Spin Transport at the International Linear Collider and its Impact on the Measurement of Polarization

Dissertation

zur Erlangung des Doktorgrades
des Department Physik
der Universität Hamburg

vorgelegt von

Moritz Beckmann

aus Hannover

Hamburg
2013

Gutachterin der Dissertation:	Dr. Jenny List Prof. Dr. Gudrid Moortgat-Pick
Gutachterin der Disputation:	Dr. Jenny List Prof. Dr. Erika Garutti
Datum der Disputation:	25.11.2013
Vorsitzender des Prüfungsausschusses:	Dr. Georg Steinbrück
Vorsitzender des Promotionsausschusses:	Prof. Dr. Peter Hauschildt
Dekan der MIN-Fakultät:	Prof. Dr. Heinrich Graener
Leiterin des Department Physik:	Prof. Dr. Daniela Pfannkuche

Abstract

At the planned International Linear Collider (ILC), the longitudinal beam polarization needs to be determined with an unprecedented precision. For that purpose, the beam delivery systems (BDS) are equipped with two laser Compton polarimeters each, which are foreseen to achieve a systematic uncertainty of $\leq 0.25\,\%$. The polarimeters are located 1.6 km upstream and 150 m downstream of the e^+e^- interaction point (IP). The average luminosity-weighted longitudinal polarization $\mathcal{P}_z^{\text{lumi}}$, which is the decisive quantity for the experiments, has to be determined from these measurements with the best possible precision. Therefore, a detailed understanding of the spin transport in the BDS is mandatory to estimate how precise the longitudinal polarization at the IP is known from the polarimeter measurements. The envisaged precision for the propagation of the measurement value is $\leq 0.1\,\%$.

This thesis scrutinizes the spin transport in view of the achievable precision. A detailed beamline simulation for the BDS has been developed, including the simulation of the beam-beam collisions at the IP. The following factors which might limit the achievable precision is investigated: a variation of the beam parameters, the beam alignment precision at the polarimeters and the IP, the bunch rotation at the IP, the detector magnets, the beam-beam collisions, the emission of synchrotron radiation and misalignments of the beamline elements.

In absence of collisions, a precision of $0.085\,\%$ on the propagation of the measured longitudinal polarization has been found achievable. This result however depends mainly on the presumed precisions for the parallel alignment of the beam at the polarimeters and for the alignment of polarization vector. In presence of collisions, the measurement at the downstream polarimeter depends strongly on the intensity of the collision and the size of the polarimeter laser spot. Therefore, a more detailed study of the laser-bunch interaction is required for a quantitative statement.

Zusammenfassung

Am geplanten International Linear Collider (ILC) soll die longitudinale Polarisation der kollidierenden Leptonstrahlen mit einer bisher unerreichten Präzision bestimmt werden. Dafür sind zwei Laser-Compton-Polarimeter pro Strahlzuführungssystem (beam delivery system, BDS) vorgesehen, die die longitudinale Polarisation mit einem systematischen Fehler $\leq 0{,}25\,\%$ messen sollen. Die beiden Polarimeter befinden sich 1,6 km vor bzw. 150 m hinter dem Kollisionspunkt (interaction point, IP). Die entscheidende Größe für die Experimente, die mittlere luminositätsgewichtete longitudinale Polarisation $\mathcal{P}_z^{\text{lumi}}$, soll aus diesen Messungen so genau wie möglich bestimmt werden. Um abschätzen zu können, wie genau sich die longitudinale Polarisation am IP aus den Messungen der Polarimeter bestimmen lässt, ist ein detailliertes Verständnis des Spintransports im BDS erforderlich. Die angestrebte Genauigkeit für die Propagation des Messwertes beträgt $\leq 0.1\,\%$.

Die vorliegende Arbeit betrachtet den Spintransport im Hinblick auf die erzielbare Genauigkeit. Zu diesem Zweck ist eine detaillierte Strahlsimulation entwickelt worden, die auch die Simulation der Strahlkollisionen am IP beinhaltet. Eine mögliche Begrenzung der erzielbaren Genauigkeit durch folgende Faktoren wird untersucht: eine Variation der Strahlparameter, die Genauigkeit der Strahlausrichtung an den Polarimetern und am IP, die Drehung der Teilchenpakete am IP, die Detektormagnete, die Kollisionen der Strahlen, die Emission von Synchrotronstrahlung und Fehlstellungen der Strahlrohrelemente.

Finden keine Kollisionen statt, lässt sich eine Genauigkeit von $0{,}085\,\%$ für die Propagation des Messwertes erreichen. Dieses Ergebnis beruht jedoch hauptsächlich auf den Annahmen über die erreichbare Genauigkeit für die parallele Ausrichtung des Strahls an den Polarimetern und für die Ausrichtung des Polarisationsvektors. Finden Kollisionen statt, hängt die hinter dem IP gemessene longitudinale Polarisation stark von der Intensität der Kollisionen und der Fokussierung des Laserstrahls des Polarimeters ab. Daher ist in diesem Fall für eine quantitative Aussage noch eine detailliertere Untersuchung der Wechselwirkung des Lasers mit dem Teilchenpaket erforderlich.

Contents

Chapter 1

Introduction

In the year 2012, a Higgs boson has been discovered [1] at the Large Hadron Collider (LHC), which might either complete the standard model of particle physics or point towards one of many possible extensions, e. g. supersymmetry.

The LHC is a proton-proton collider. In contrast to a lepton collider, it can achieve higher collision energies and is more suitable to produce strongly interacting particles. However, a hadron collider suffers from the inherent handicap of limited knowledge of the initial conditions in the collisions and the strong QCD background in the collision. A lepton collider allows for measurements with higher precision and therefore also for indirect measurements of phenomena at much higher energies than the actual collision energy, as the Large Electron-Positron Collider (LEP) has already shown [2], and is more suitable to study electroweak interactions. Therefore, a new linear collider as complement to the LHC is desirable with view on e. g. the model-independent measurement of the Higgs couplings and branching ratios or the search for the electroweak sector of supersymmetry.

For such a new lepton collider, polarized beams are beneficial [3] as explained in the following. The cross-section of electroweak processes depends on the polarization of the incoming particles. Thus, beam polarization introduces new observables: at a collider with polarized beams, the polarized cross sections (cf. section 5.3), which are key observables at an e^+e^- collider, can be determined separately. Without beam polarization, only the unpolarized cross section, i. e. the average value of the polarized cross sections, can be measured. The dependence of the cross sections on the polarization can be employed to enhance desired processes and suppress undesired ones and raise thereby the effective luminosity. The benefits of polarized beams have already been demonstrated at the Stanford Linear Collider (SLC) in the determination of the effective weak mixing angle $\sin^2\theta_W^{\text{eff}}$ [4, 5]. The SLC

achieved an electron beam polarization of about 80 %; the positron beam was unpolarized. Furthermore, polarized beam allow to study the chiral structures of interaction and determine the chirality of new particles. This requires in many cases both beam to be polarized.

There are currently two such polarized electron-positron colliders being planned: the International Linear Collider (ILC, see chapter 2 and [6]) and the Compact Linear Collider (CLIC) [9]. This thesis focuses on the ILC, which is foreseen to provide collisions with a center-of-mass energy of $200 - 500\,\mathrm{GeV}$ (upgradable to 1 TeV) and polarizations of $\geq 80\,\%$ for the electron beam and $\geq 30\,\%$ for the positron beam.

The precision to which the polarized cross sections can be determined depends mainly on how exactly the beam polarizations are known at the interaction point e^+e^- (IP). Therefore, a determination of the beam polarizations as precise as possible is crucial, which comprises not only the measurements at the polarimeters, but also the spin transport from the polarimeters to the IP. While spin transport studies for circular accelerators have already been carried out earlier [10, 11], such studies at linear accelerators are a novelty. The situation at circular accelerators is however fundamentally different due to long-term effects (e. g. polarization build-up by Sokolov-Ternov effects) and additional constraints (e. g. closed orbits) which do not appear at linear colliders. At the SLC, dedicated simulations for the spin transport have not been carried out. The spin transport [5] has been derived from the particle transport and T-BMT precession (cf. sections 4.2.1 and 7.3) instead. The uncertainties from the spin transport including the collision effects have been found negligible with respect to the uncertainty of 0.5 % on the measurement of the longitudinal polarization at the SLD Compton polarimeter. This measurement has been the most precise one at a high-energy collider so far. Nevertheless, for the measurement at the ILC, a precision of 0.25 % is envisaged for the polarimeter measurement (cf. chapter 5). Furthermore, the effects of the T-BMT precession and the collision effects will be stronger at the ILC due to the higher collision energies (SLC: 91 GeV) and the stronger focussing of the beams at the IP. Therefore, dedicated spin transport simulations are required for the ILC.

Several spin tracking studies have already been carried out for the ILC, but with different foci. A study by J. Smith investigates the polarization losses along the way from the beam source to the IP with a precision of 1 % [12], which is however not precise enough for the purpose of polarimetry and neglects the polarimeter behind the IP. Studies by A. Hartin [13] regarding the spin transport between the polarimeters preceeded this thesis, but concentrated on single aspects, like the collision effects (cf. chapter 9) or misalignments and ground motion (cf. chapter 10).

A comprehensive spin transport simulation for the ILC BDS including these effects has been set up in this thesis. In the first part of this thesis, the basic concepts are introduced; in the second part, the results are presented. First preliminary results from an earlier version of the simulation have already been published in [14].

Chapter 2

The International Linear Collider (ILC)

The International Linear Collider (ILC) [6] is a planned electron-positron collider with a center-of-mass collision energy of $200 - 500\,\text{GeV}$ (upgradable to $1\,\text{TeV}$). The design foresees an electron beam polarization at the e^+e^- interaction point (IP) of $\geq 80\,\%$ and a positron beam polarization at the IP of $\geq 30\,\%$ (extendable to $60\,\%$).

2.1 Overview

For an e^+e^- collider ring at these beam energies, either the energy loss due to synchrotron radiation or the size of the ring would be unacceptably large. Therefore, the ILC is not designed as a collider ring like LEP and the LHC, but as a linear collider.

A first comprehensive description of the planned accelerator was published as the Reference Design Report (RDR) [15]. Several changes were put down in the SB2009 proposal [17] and implemented then in the Technical Design Report (TDR) [6].

Figure 2.1 shows the basic layout of the ILC. A polarized electron beam is produced by a photocathode gun and accelerated to an energy of $5\,\text{GeV}$. In the damping rings, the bunch emittances (cf. section 3.2.3) are minimized. Thereafter, the beam is guided to the turn-around (left end of figure 2.1). Behind the turn-around, spin rotators are located, which adjust the polarization vector to any desired orientation. In the following, the beam is accelerated in the main linac (linear accelerator) to the desired beam energy ($100 - 250\,\text{GeV}$). Behind the main linac, the positron beam source is located, which comprises an helical undulator section and a target. In the undula-

tors, the electron beam radiates off circularly polarized photons. Afterwards, the electron beam is separated from the photons and guided by the beam delivery system (BDS) to the IP and eventually to the electron beam dump. The photons produced in the undulators hit the target where they produce electron-positron pairs. The polarized positrons are selected, are accelerated to 5 GeV and run through the same procedure as the electron beam afterwards. Most relevant for this thesis is the BDS, which is presented in more detail in section 2.2.

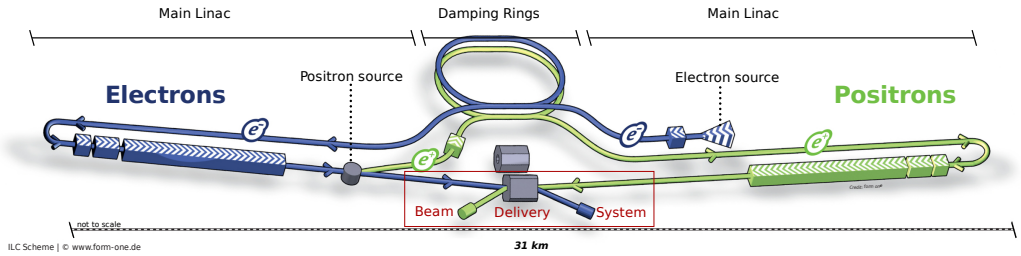

Figure 2.1: Schematic view of the International Linear Collider (ILC) according to the Technical Design Report (TDR). Taken from [18] and modified.

According to the TDR baseline design, the beams consist of 5 bunch trains per seconds. Each bunch trains contains 1 312 electron bunches.

2.2 The Beam Delivery System (BDS)

Behind the main accelerator, where each beam is accelerated to its final energy for the collision, follows the *beam delivery system* (BDS). It guides the beam to the interaction point (IP), and transports the spent beam further to the beam dump.

Figure 2.2 shows a schematic view of the electron BDS up to the IP. The beamline contains (among others) the following sub-systems:

- The undulator for the generation of photons, which are used to generate the positron beam, and the (photon) target bypass (dogleg). This subsystem does not exist in the positron beamline. It is technically not part of the beam delivery system, but it is included in the BDS lattice files (cf. section 7.1.1).
- The chicane[1] to detect the photons from the laser-wire emittance measurement. In the RDR layout, this chicane hosted also the upstream

[1] A chicane denotes a section of the beamline in which the beam is offset with respect to its original course. At the end of the chicane, it is brought back to its original course. Examples can be found in figures 5.3 and 5.4.

Compton-polarimeter. Since those two measurement would interfere with each other, the polarimeter has been moved to a separate chicane.

- The new chicane for the upstream Compton-polarimeter. The polarimeters will be introduced in detail in chapter 5.
- A double curve for the energy collimation including the upstream energy spectrometer.
- The final focus magnets to prepare the beam for the collision.
- The interaction point (IP), where the electron bunches collide with the positron bunches. The full crossing angle between the e^--beamline and the e^+-beamline amounts to $\zeta = 14\,\text{mrad}$ (cf. section 3.1.2).

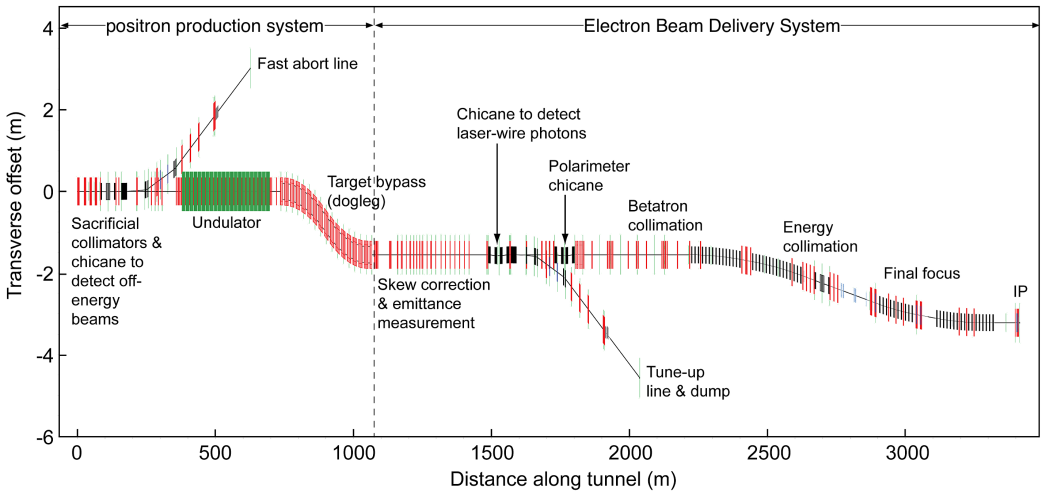

Figure 2.2: Layout of the electron beam delivery system (BDS). The actual BDS starts at the vertical dotted line. The extraction line following behind the IP is not shown. The positron BDS is a mirror image. Taken from figure 2.12 in [7].

Behind the IP (not shown in figure 2.2), the extraction line follows, comprising these sub-systems:

- The extraction line quadrupoles (5-46 m behind the IP), that serve to recapture the disrupted beam after the collision and collimate it at the second focal point 147 m behind the IP.
- The downstream energy spectrometer chicane (46-73 m behind the IP).

- The downstream Compton-polarimeter chicane (120-175 m behind the IP) with the second focal point.
- The beam dump, where the spent beam is absorbed (301 m behind the IP).

In order to obtain a small vertical beam size at the IP, a main criterium in the design of the BDS is to minimize the growth of the vertical emittance (cf. section 3.2.3). Therefore, all curves and chicanes in front of the IP are set up in the horizontal plane as shown in figure 2.2 in order to avoid such a growth by emission of synchrotron radiation. The chicanes behind the IP are set up in the vertical plane [7, 16].

The beamline is described by the *lattice*, which is a list of all beamline elements (magnets, cavities, collimators etc.) and their properties that are relevant for the particle tracking (position, length, alignment, aperture, electromagnetic fields etc.). The most relevant elements for this thesis are dipole magnets, which serve to deflect the beam (see also section 6.1), and quadrupole magnets, which serve to focus the beam (see also section 6.2). The term "lattice" refers to the repeating sequences of quadrupole magnets which are required to keep a particle beam focussed over long distances.

Throughout this thesis, the lattice version `SB2009_Nov10` is used [19]. In comparison with the RDR version, the most relevant change for this study is the introduction of the separate chicane for the upstream polarimeter, which however is less important for the spin transport than for the actual measurement (see above). The `SB2009_Nov10` lattice version has not been optimized for the new beam parameters according to SB2009. Therefore, the nominal RDR beam parameter set is employed for this study (chapter 7). The new parameter set of the TDR is expected to affect the polarization mainly via the beam-beam collisions and will therefore be discussed in chapter 9.

Several elements are not yet included in the lattice files. The undulators at the beginning of the e^--beamline and the crab cavities (to compensate for the beam-beam crossing angle, see section 8.1) are replaced by placeholders (drift tubes), the detector magnets are not included at all. The main effects of the undulators would be a loss in energy and an increased energy spread. Therefore, the e^--beam is initialized with the corresponding energy distribution, which it actually would only have after passing the undulators. For this study, the crab cavities and the detector magnets have been added as described in chapter 8.

Chapter 3

Coordinate Systems and Notation

This chapter explains the notation used throughout this thesis and contains the definitions of the employed coordinate systems (section 3.1) and the parameters used to describe the properties of a particle bunch (section 3.2). The definition of the particle coordinates explained in section 3.1.1 might be not entirely intuitive and therefore requires special attention.

Throughout this thesis, SI units are used. Natural units might be used occasionally.

The term "electron" is not only used to denote e^-, but also as collective terms for e^- and e^+. Since all particle interactions involved in this thesis originate from quantum electrodynamics (QED), all effects are symmetric for electrons and positrons, apart from differences in the lattice and the different degrees of beam polarization.

A list of the symbols used in this thesis is attached at the very end of this thesis.

3.1 Coordinate Systems

In this section, the different coordinate systems used throughout this thesis are introduced. The particle transport is described using the **beamline coordinate system** and the particle coordinates (section 3.1.1). For the collision process and the detector magnets, the **detector coordinate system** (section 3.1.2) is used, which differs only by the orientation of a few axes from the coordinate system which is used internally in Guinea-Pig++ (section 3.1.3) to simulate the collisions (cf. chapter 9 and [20]). The peculiarities of the transformations between the coordinate systems are described

in section 3.1.4.

3.1.1 Beamline Coordinate System

For the particle tracking, the coordinate system of Bmad is adopted [21, 22]. This includes the *local reference coordinate system* as well as the *particle coordinates* to parametrize the simulated particles. These two concepts are introduced now.

Local Reference Coordinate System

To denote the position of a simulated particle in the laboratory frame, the local reference coordinate system as shown in figure 3.1 is used, which is based on the reference orbit: separately for the electron beamline and the positron beamline, the *reference orbit* is defined as the path of an imaginary perfect particle with exactly the nominal energy - the reference particle - that passes all beamline elements centrally. Misalignments are not taken into account for the definition and do not alter the reference orbit as line of reference. Dipole magnets are the only beamline elements which curve the reference orbit; in all other elements that occur in the ILC BDS lattice, the reference orbit runs straight. The coordinate s denotes the distance the reference particle has traveled along the reference orbit. At the beginning of a lattice, $s = 0$ by convention.

The z-axis of local reference coordinate system is tangent to the reference orbit and points in the direction of increasing s. At the beginning of the beamline, the y-axis is oriented along the vertical direction and points upwards (up to the first non-horizontal bending magnet). The x-axis is defined by the right-handedness of the coordinate system. The origin of the coordinate system is located on the reference orbit, such that $z = 0$ by construction and the position is specified by (x, y, s).

Particle Coordinates

Based on the local reference coordinate system, a particle is parametrized by the coordinates[1]

$$\boldsymbol{r}(s) = (x, \hat{p}_x, y, \hat{p}_y, \hat{z}, \delta) \tag{3.1}$$

which will be introduced in detail now. The position s along the reference orbit is used as the independent variable in this parametrization. Instead of

[1] In [22], these coordinates $\boldsymbol{r}(s) = (x, \hat{p}_x, y, \hat{p}_y, \hat{z}, \delta)$ are denoted by (x, p_x, y, p_y, z, p_z) and referred to as "phase-space coordinates". The unnormalized momenta $p_{x,y,z}$ are denoted by $P_{x,y,z}$.

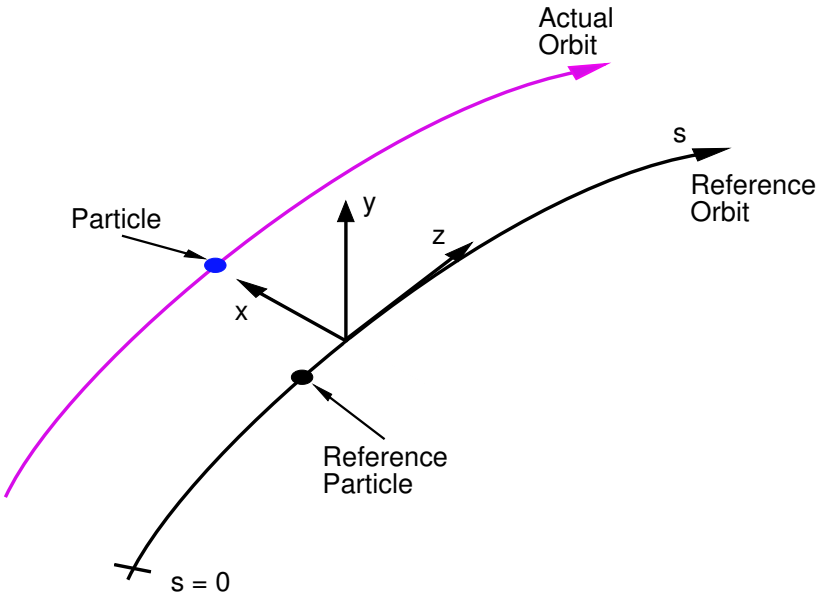

Figure 3.1: The local reference coordinate system in Bmad. The positions of a particle and the reference particle are shown here at a given time t. Taken from figure 9.1 in [22] and modified.

a longitudinal coordinate,

$$\hat{z}(s) = -\beta(s)\, c \left(t(s) - t_0(s) \right) \tag{3.2}$$

is used, where $\beta(s)$ is the relativistic Lorentz factor of the simulated particle and $t(s)$ and $t_0(s)$ denote the arrival times at s of the simulated particle and the reference particle, respectively. $\hat{z} > 0$ means that the simulated particle is ahead of the reference particle.

If the reference orbit is not curved and the simulated particle does not move relative to the reference particle, $\hat{z}$ corresponds to the longitudinal distance between the simulated particle and the reference particle. Both conditions are fulfilled. Any non-negligible relative motion would tear the bunch apart. At the relevant points in the ILC lattice (the beginning of the lattice, the e^+e^- interaction point (IP) and the laser-bunch IPs of the polarimeters; see section 2.2), the reference orbit is not curved. This is also true at the IP, since the detector magnets do not alter the reference orbit (cf. sections 6.1.1) and 8.2.

Therefore, $\hat{z}$ will be used as longitudinal coordinate throughout this thesis and be called z, since the $z = 0$ as defined above is of no practical use. $x(s)$ and $y(s)$ are the transverse coordinates. Figure 3.2 illustrates for the

horizontal plane how the coordinates should be interpreted. For the sketched particle is $x(s) = x_0$, regardless of the value of $\hat{z}(s)$. Especially for $\hat{z}(s) \approx z = z_0$, note that $x(s) \neq x_1$! Therefore, the triple (x, y, z) is not a meaningful position in space. Instead, the triple (x, y, s) is a meaningful position in space that describes e. g. where a particle enters a magnet. But $(x, y, s + z)$ is in general not the position of the particle at the time the reference particle enters the magnet. In cases where the x-coordinate at the arrival time of the reference particle is required, it is denoted by $x(s + z) = x_1$.

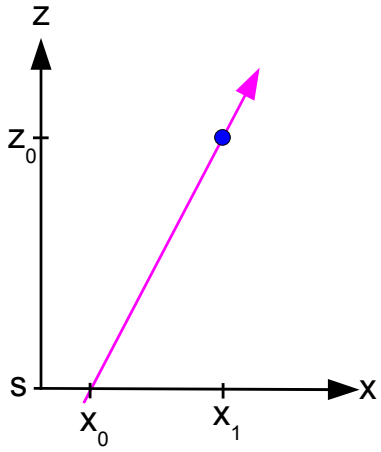

Figure 3.2: Illustration of the transverse coordinates. $x(s) = x_0$, regardless of the value of $\hat{z}(s)$.

Instead of the classical momentum vector $\vec{p} = (p_x, p_y, p_z)$, normalized quantities are used to describe the particle momentum, which are denoted as $(\hat{p}_x, \hat{p}_y, \delta)$. They are related by:

$$\begin{pmatrix} \hat{p}_x \\ \hat{p}_y \\ \delta \end{pmatrix} = \frac{1}{p_0} \begin{pmatrix} p_x \\ p_y \\ |\vec{p}| - p_0 \end{pmatrix} \quad \Leftrightarrow \quad \begin{pmatrix} p_x \\ p_y \\ p_z \end{pmatrix} = p_0 \begin{pmatrix} \hat{p}_x \\ \hat{p}_y \\ \sqrt{(1+\delta)^2 - \hat{p}_x^2 - \hat{p}_y^2} \end{pmatrix}$$

where $p_0 = \sqrt{(E_0)^2 - m_e^2}$ is the reference momentum of the beam, E_0 the nominal beam energy and m_e the electron mass. Since this study involves only relativistic electrons,

$$\delta = \frac{|\vec{p}| - p_0}{p_0} \approx \frac{E - E_0}{E_0}$$

where E is the individual particle energy.

The standard particle tracking method of Bmad used in this study assumes $\hat{p}_x, \hat{p}_y \ll 1$, for which the slopes of a particle trajectory outside bending magnets are given by (contributions from transverse magnetic fields are omitted here, since they are negligible at the relevant points):

$$x' = \frac{dx}{ds} \approx \frac{\hat{p}_x}{1+\delta} = \frac{p_x}{|\vec{p}|}$$
$$y' = \frac{dy}{ds} \approx \frac{\hat{p}_y}{1+\delta} = \frac{p_y}{|\vec{p}|}. \tag{3.3}$$

For the definition of the polarization vector $\vec{\mathcal{P}}$ in this coordinate system see section 3.2.5.

3.1.2 Detector Coordinate System

At the interaction point (IP), the coordinate system of the detector concept ILD (formerly LDC) as sketched in figure 3.3 is used [23]. The e^--beamline and the e^+-beamline cross at an angle $\zeta = 14\,\text{mrad}$. The origin of the detector coordinate system is the IP (i. e. the intersection point of the reference orbits of the e^-- and the e^+-beamline). The z-axis runs parallel to the detector axis and is oriented such that $p_z > 0$ for the e^--beam (thus the angle with respect to the e^--beamline coordinate system at $s = s_{\text{IP}}$ is $\zeta/2 = 7\,\text{mrad}$, but $\pi - \zeta/2$ with respect to the e^+-beamline coordinate system at $s = s_{\text{IP}}$). The y-axis is again oriented along the vertical direction and points upwards; the x-axis is defined by the the coordinate system being right-handed.

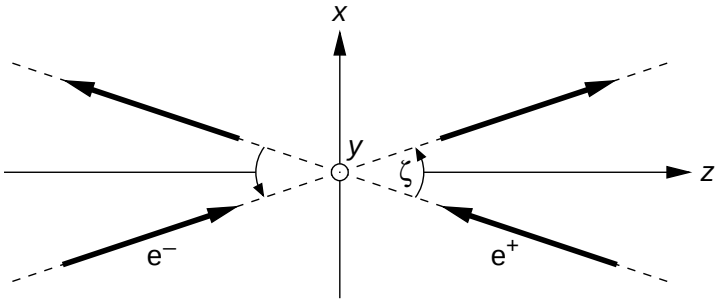

Figure 3.3: Detector coordinate system used at the IP. Taken from figure 1 in [23] and modified. The axes labeled x, y, z in this sketch are denoted in this thesis as $x^{\text{D}}, y^{\text{D}}, z^{\text{D}}$, respectively.

The axes of the detector coordinate system will be labeled $x^{\text{D}}, y^{\text{D}}, z^{\text{D}}$ subsequently to avoid confusion with the axes of the beamline coordinate

systems (y^{D} only for the sake of uniformity; the y-axes of the detector coordinate system and both beamline coordinate systems are identical).

For the definition of the polarization vector $\vec{\mathcal{P}}^{\mathrm{D}}$ in this coordinate system see section 3.2.5.

3.1.3 Guinea-Pig++ Coordinate Systems

Guinea-Pig++ uses two separate coordinate systems, one for each beam. They are only used internally in the simulation and therefore listed here only for reference. The axes of these coordinate systems are here label by $x^{\mathrm{G\text{-}}}$ etc. for e^--beam and by $x^{\mathrm{G+}}$ etc. for e^+-beam, respectively. The origin and is the same as for the detector coordinate system described in the previous section, but the orientation of several axes is flipped as as follows:

$$\begin{aligned} x^{\mathrm{G\text{-}}} &= x^{\mathrm{G+}} &&= -x^{\mathrm{D}} \\ y^{\mathrm{G\text{-}}} &= y^{\mathrm{G+}} &&= y^{\mathrm{D}} \\ -z^{\mathrm{G\text{-}}} &= z^{\mathrm{G+}} &&= z^{\mathrm{D}} \end{aligned}$$

Thus the coordinate system of the e^--beam is right-handed, whereas the one of the e^+-beam is left-handed [24, 25].

As described in section 3.1.1, x and y denote the position where the particle trajectory intersects the plane perpendicular to the reference orbit at $s = s_{\mathrm{IP}}$. z denotes the longitudinal position in the bunch.

The definition of the polarization vector in this coordinate system is described in section 3.2.5.

3.1.4 Transformations between the Coordinate Systems

Since all involved coordinate systems do not move relative to each other, the transformation between the beamline coordinate system and the detector coordinate system is only a rotation about the y-axis by the corresponding angle. Due to their special definition (section 3.1.1), x and z transform as follows: if z is regarded as the longitudinal position and x' can be assumed to be constant over the length of the bunch, the horizontal distance of the particle from the reference orbit at $s + z(s)$ is

$$x(s + z) = x(s) + x'(s) \cdot z(s).$$

$\big(x(s + z), z(s)\big)$ transforms as a spatial vector and

$$\arctan\left(x'^{\mathrm{D}}\right) = \arctan\left(x'\right) + \lambda \tag{3.4}$$

where ζ is the beam crossing angle at the IP and $\lambda = \zeta/2 = 7\,\text{mrad}$ for the e^--beam and $\lambda = \pi - \zeta/2$ for the e^+-beam.

Therefore,

$$\begin{pmatrix} x^{\mathrm{D}} \\ z^{\mathrm{D}} \end{pmatrix} = \begin{pmatrix} 1 & -x'^{\mathrm{D}} \\ 0 & 1 \end{pmatrix} \cdot \begin{pmatrix} \cos\lambda & \sin\lambda \\ -\sin\lambda & \cos\lambda \end{pmatrix} \cdot \begin{pmatrix} 1 & x' \\ 0 & 1 \end{pmatrix} \cdot \begin{pmatrix} x \\ z \end{pmatrix} \tag{3.5}$$

$$= \begin{pmatrix} \cos\lambda - \sin\lambda \cdot x'^{\mathrm{D}} & 0 \\ -\sin\lambda & \cos\lambda + \sin\lambda \cdot x' \end{pmatrix} \cdot \begin{pmatrix} x \\ z \end{pmatrix}.$$

The 12-element of the transformation matrix being zero reflects again the special definition of $x(s)$ used here, which is not connected to z (see section 3.1.1). The transformation of the polarization vector is described in section 3.2.5.

3.2 Bunch Parametrization

A particle bunch is an ensemble of $N_e \sim 10^{10}$ particles. Due to limited computing resources, the simulation contains only N_e^{macro} so-called macroparticles[2], where one macroparticle represents N_e/N_e^{macro} real particles.

3.2.1 Position and Size

The macroparticles are parametrized by the coordinates $\boldsymbol{r}(s)$ as described in section 3.1.1. The position of a bunch and its extension are described by the arithmetic means of the particle coordinates $\langle x\rangle$, $\langle y\rangle$, $\langle z\rangle$ and the corresponding standard deviations

$$\begin{pmatrix} \sigma_x \\ \sigma_y \\ \sigma_z \end{pmatrix} = \begin{pmatrix} \mathrm{stddev}\, x \\ \mathrm{stddev}\, y \\ \mathrm{stddev}\, z \end{pmatrix} \text{ , where } \mathrm{stddev}\, x = \sqrt{\langle x^2\rangle - \langle x\rangle^2}$$

At the IP, the horizontal beam size with respect to the detector coordinate system is an important parameter. Due to the crossing angle and the rotation of the bunches (see section 8.1), the center of the bunch-bunch collision moves along the x-axis in the course of the collision, as sketched in figure 8.1. To compute the beam size without a smearing due the transverse motion, a co-moving x-coordinate

$$x^{\mathrm{D}} := x^{\mathrm{D}} \mp z^{\mathrm{D}} \cdot \sin(\zeta/2) \tag{3.6}$$

[2] "Macroparticle" is employed as general term in this thesis and does not refer to the macroparticle structure in Bmad. Instead, the simulated beam is implemented as *beam_struct*.

for an $e^{\pm}$-bunch is used, where ζ is the beam crossing angle at the IP and $\lambda = \zeta/2 = 7\,\text{mrad}$ for the e^--beam and $\lambda = \pi - \zeta/2$ for the e^+-beam. This coordinate is used to compute the bunch position $\left\langle x^{\text{D}} \right\rangle$ and the beam size σ_x^{D}. Since $\sigma_z \gg \sigma_x$, the corresponding change in the bunch length σ_z is

$$\left| \frac{\sigma_z^{\text{D}} - \sigma_z}{\sigma_z} \right| \approx 1 - \cos\left(7\,\text{mrad}\right) = 1 - 2.4 \cdot 10^{-5} \tag{3.7}$$

and therefore neglected here.

3.2.2 Motion and Divergences

Analogous to the parametrization of the bunch position, the direction of bunch motion[3] $\left(\langle x' \rangle, \langle y' \rangle \right)$ and the angular divergences[4]

$$\begin{pmatrix} \theta_x \\ \theta_y \end{pmatrix} = \begin{pmatrix} \text{stddev}\, x' \\ \text{stddev}\, y' \end{pmatrix}$$

are obtained. The longitudinal motion component is parametrized by the mean relative energy loss $\langle \delta \rangle$ and the beam energy spread $\sigma_E/E = \text{stddev}\,\delta$.

Complementary to the horizontal and vertical angular divergences and directions of motion, the total angular divergence

$$\theta_r = \sqrt{{\theta_x}^2 + {\theta_y}^2},$$

the polar angle of the direction of bunch motion

$$\vartheta_{\text{bunch}} = \sqrt{\langle x' \rangle^2 + \langle y' \rangle^2}$$

and the corresponding azimuthal angle

$$\phi_{\text{bunch}} = \text{atan2}\left(\langle y' \rangle, \langle x' \rangle \right)$$

are used, where $\text{atan2}\,(y, x)$ is the 2π-periodic extension of the arc tangent function $\arctan(y/x)$.

---

[3] $\langle x' \rangle = \left\langle \frac{dx}{ds} \right\rangle = \frac{d\,\langle x \rangle}{ds}$ (see eq. 3.3) describes the horizontal motion of the bunch center. Unlike the x-component of the bunch momentum, which might have been the more intuitive choice, it does not weigh the contributions with the norm of the particle momentum.

[4] The symbols θ and ϑ are two variations to write the lowercase Greek letter Theta. Throughout this thesis, θ is used for angular divergences and ϑ for (polar) angles. The angular divergences θ_x, θ_y are also called $\sigma_{x'}$, $\sigma_{y'}$ in some publications.

3.2.3 Emittances

The emittances ε_x and ε_y are a measure for the beam quality, i. e. its "focussability". ε_x is given by

$$\varepsilon_x = \sqrt{\sigma_x^2\,\theta_x^2 - \Big\langle \big(x - \langle x\rangle\big)\big(x' - \langle x'\rangle\big)\Big\rangle^2} \tag{3.8}$$

and ε_y analogously.

Sometimes, the normalized emittance

$$\gamma\varepsilon_x = \frac{E_0}{m_\mathrm{e}}\,\varepsilon_x \tag{3.9}$$

is given instead. See also section 6.3.

3.2.4 Disruption Parameters

The disruption parameter provide a measure for the strength of the disruption effects in a beam-beam collision. They are calculated from the undisturbed bunch parameters as follows:

$$\begin{aligned} D_x =& \frac{2r_e N_e \sigma_z}{\gamma\sigma_x\,(\sigma_x + \sigma_y)} \\ D_y =& \frac{2r_e N_e \sigma_z}{\gamma\sigma_y\,(\sigma_x + \sigma_y)} \end{aligned} \tag{3.10}$$

3.2.5 Polarization

The bunch polarization is described by the polarization vector

$$\vec{\mathcal{P}} = \begin{pmatrix} \mathcal{P}_x \\ \mathcal{P}_y \\ \mathcal{P}_z \end{pmatrix}.$$

The exact definition of the polarization is given in section 4.1; the macroparticle polarization is introduced in section 7.1.2. The polarization $|\vec{\mathcal{P}}|$ is referred to as "entire" polarization here to distinguish it more clearly from the transverse / longitudinal polarization. The components of $\vec{\mathcal{P}}$ express the polarization along the corresponding axes of the beamline coordinate system (section 3.1.1). Thus $\mathcal{P}_z$ is the component parallel to the reference orbit.

If $\hat{p}_x = 0 = \hat{p}_y$, $\mathcal{P}_z$ corresponds to the helicity, which is the component parallel to the momentum vector. Since $\hat{p}_x$ and $\hat{p}_y$ are typically sufficiently

small, the terms "longitudinal polarization" and "helicity" are often used synonymous.

The orientation of the reference orbit is identical at the relevant points (see section 3.1.1) of each beamline; thus the orientations of the axes of the beamline coordinate systems at these points are identical as well.

In the detector coordinate system (section 3.1.2), the components of the polarization vector $\vec{\mathcal{P}}^{\mathrm{D}}$ also refer to the axes of the detector coordinate system, but with one exception: for the e^+ beam, the opposite signs are assigned to $\mathcal{P}_x^{\mathrm{D}}$ and $\mathcal{P}_z^{\mathrm{D}}$ (corresponding to a 180° rotation about the y^{D}-axis) to avoid a seeming flip of the polarization due to the choice of the coordinate system.

Therefore, the components of the polarization vector transform via

$$\begin{pmatrix} \mathcal{P}_x^{\mathrm{D}} \\ \mathcal{P}_z^{\mathrm{D}} \end{pmatrix} = \begin{pmatrix} \cos\lambda & \sin\lambda \\ -\sin\lambda & \cos\lambda \end{pmatrix} \cdot \begin{pmatrix} \mathcal{P}_x \\ \mathcal{P}_z \end{pmatrix} \tag{3.11}$$

where ζ is the beam crossing angle at the IP and $\lambda = \zeta/2 = 7\,\mathrm{mrad}$ for the e^--beam and $\lambda = (\pi - \zeta/2) - \pi = -7\,\mathrm{mrad}$ for the e^+-beam. Since the y-axes at the IP are identical in all systems, so is the vertical polarization: $\mathcal{P}_y \equiv \mathcal{P}_y^{\mathrm{D}}$.

In Guinea-Pig++, the transverse components of the polarization vector $\mathcal{P}_x$ and $\mathcal{P}_y$ refer to the axes of the coordinate system described in section 3.1.3, whereas the longitudinal component $\mathcal{P}_z$ contains an additional sign, again to avoid a seeming flip of the polarization due to the choice of the coordinate system [26].

The polar angle of $\vec{\mathcal{P}}$ is denoted by

$$\vartheta_{\mathrm{pol}} = \arccos\left(\frac{\mathcal{P}_z}{\left|\vec{\mathcal{P}}\right|}\right)$$

and the corresponding azimuthal angle

$$\phi_{\mathrm{pol}} = \mathrm{atan2}\left(\mathcal{P}_y, \mathcal{P}_x\right).$$

The quotient of the polar angles of $\vec{\mathcal{P}}$ and $\vec{p}$ is denoted by

$$b = \vartheta_{\mathrm{pol}}/\vartheta_{\mathrm{bunch}}.$$

The corrected value for the longitudinal polarization (see section 7.4) is computed via

$$\mathcal{P}_z^{\mathrm{corr}} = \frac{\mathcal{P}_z}{\cos\left(a\gamma\left(1 + \langle\delta\rangle\right)\vartheta_{\mathrm{bunch}}\right)}.$$

Chapter 4

Polarization

In this chapter, the concept of polarization for massive spin-1/2 particles and the influence of electromagnetic fields on polarization are introduced.

4.1 Definition

Polarization describes the average spin orientation of an ensemble of particles. To parametrize spins, the following definition from [10] is adopted here: the expectation value of the vector operator representing the spin of a particle in its instantaneous rest frame satisfies the equation of motion of a classical spin vector. The direction of this expectation value is denoted by the spin vector $\vec{S}$ with $|\vec{S}| = 1$, where $\vec{S}$ is $(2/\hbar)$ times the expectation value.

The polarization vector of an ensemble of N particles is

$$\vec{\mathcal{P}} = \frac{1}{N} \sum_{j=1}^{N} \vec{S}_j = \left\langle \vec{S} \right\rangle_N . \tag{4.1}$$

For the representation of the polarization vector in the coordinate systems used in this thesis see chapter 3.

The (entire[1]) polarization $|\vec{\mathcal{P}}|$ is a measure for the uniformity of the spin orientation, which is commonly compared to the concept of entropy. In general, the polarization cannot be increased in an accelerator, apart from Sokolov-Ternov effects in storage rings, which shall not be discussed here.

[1]To distinguish the polarization $|\vec{\mathcal{P}}|$ from the components $\mathcal{P}_x$, $\mathcal{P}_y$ and $\mathcal{P}_z$ of the polarization vector, the word "entire" is used occasionally for clarification in this thesis to denote $|\vec{\mathcal{P}}|$.

4.1.1 Transformation under a Lorentz Boost

To calculate the polarization in an arbitrary inertial system of reference, one needs to know its behavior under Lorentz boosts. The transformation of spin vectors $\vec{T}, \vec{U}$ (not normalized to $|\vec{T}| = |\vec{U}| = 1$) is given in [27]:

Let $\vec{T}$ be the spin vector in the particle's instantaneous rest frame, i. e.

$$\vec{T} = \frac{\hbar}{2}\,\vec{S}, \tag{4.2}$$

and $\vec{U}$ the spin vector in a frame in which the particle moves with the velocity $\vec{v}$. They are related by

$$\begin{aligned} \vec{T} &= \vec{U} - \frac{\gamma}{\gamma+1}\frac{\left(\vec{v}\cdot\vec{U}\right)\vec{v}}{c^2} = \vec{U} - \frac{\beta^2\,\gamma}{\gamma+1}\cdot\vec{U}_{\parallel} \\ \vec{U} &= \vec{T} + \frac{\gamma^2}{\gamma+1}\frac{\left(\vec{v}\cdot\vec{T}\right)\vec{v}}{c^2} = \vec{T} + \frac{\beta^2\,\gamma^2}{\gamma+1}\cdot\vec{T}_{\parallel} = \vec{T} + (\gamma-1)\cdot\vec{T}_{\parallel}, \end{aligned} \tag{4.3}$$

where c is the vacuum speed of light and β and γ are the relativistic Lorentz factors. $\vec{U}_{\parallel}$ and $\vec{T}_{\parallel}$ are the projections of $\vec{U}$ and $\vec{T}$ on $\vec{v}$.

To calculate the polarization, the spin vectors have to be normalized by their length, which is $|\vec{T}| = \hbar/2$ in the particle's rest frame, and

$$|\vec{U}| = \sqrt{|\vec{T}|^2 + \left(\gamma\frac{\vec{v}\cdot\vec{T}}{c}\right)^2} = \sqrt{|\vec{T}|^2 + (\gamma-1)\cdot|\vec{T}_{\parallel}|^2}. \tag{4.4}$$

Thus the polarization is invariant under a Lorentz boost purely parallel or perpendicular to the polarization vector, but not for other directions.

4.1.2 Luminosity-Weighted Polarization

The luminosity $\mathcal{L}$ is the event rate $\dot{N}$ of hard particle interactions divided by the total cross section σ_{tot} of these interactions:

$$\mathcal{L} = \frac{\dot{N}}{\sigma_{\text{tot}}} \tag{4.5}$$

The total cross section depends on the polarizations of the incoming electrons and positrons. Therefore, the polarization of each beam needs to be known in order to determine a cross section from the number of events in a data sample with a given time-integrated luminosity. Relevant is however not the

polarization of the entire bunches, but the average spin orientation of only those particles which actually undergo a hard interaction. This quantity is called luminosity-weighted polarization. For a single collision of an electron bunch and a positron bunch, it is denoted here by the symbol $\vec{\mathcal{P}}^{\text{lumi},1}$.

The luminosity-weighted polarization for a series of many collisions is denoted by the symbol $\vec{\mathcal{P}}^{\text{lumi}}$ and given by

$$\vec{\mathcal{P}}^{\text{lumi}} = \frac{\sum_i \mathcal{L}_i \cdot \vec{\mathcal{P}}_i^{\text{lumi},1}}{\sum_i \mathcal{L}_i}, \tag{4.6}$$

where $\mathcal{L}_i$ and $\vec{\mathcal{P}}_i^{\text{lumi},1}$ denote the luminosities and the luminosity-weighted polarizations of the single bunch crossings enumerated by the index i. More generally, the luminosity-weighted polarization is usually expressed as

$$\vec{\mathcal{P}}^{\text{lumi}} = \frac{\int \mathcal{L}(t)\vec{\mathcal{P}}^{\text{lumi},1}(t)\,dt}{\int \mathcal{L}(t)\,dt}. \tag{4.7}$$

The luminosity-weighted polarization is the value which is required for the analysis of the particle physics data collected by the experiments and which the polarization measurement seeks to determine in the end.

4.2 Interaction with Electromagnetic Fields

Spins interact with electromagnetic fields. The essential mechanisms of a polarized electron beam interacting with an electromagnetic field which are relevant for this study are discussed in the rest of this chapter.

The direct influence of electromagnetic fields on spins is described by T-BMT precession (section 4.2.1) and by the emission of electromagnetic radiation which can cause a spin-flip (section 4.2.3). Indirectly, the energy loss due to the emission of a radiation affects the further spin propagation by the energy loss.

4.2.1 T-BMT Precession

Let us consider a spin-carrying particle in its rest frame. In presence of a magnetic field, the spin precesses around the magnetic field, which is known as Thomas precession. The Thomas-Bargmann-Michel-Telegdi equation - short T-BMT equation - expresses the same phenomenon in the laboratory frame. Moving from the particle's rest frame to the laboratory frame, parts of the magnetic field in the rest frame are transformed into an electric field

perpendicular to the boost direction. Therefore, a perpendicular electric field in the laboratory frame contributes to the precession as well. Let q, m, $\vec{p}(t)$ and $\vec{r}(t)$ denote the charge, mass, momentum and position, respectively, of a particle at a time t in the laboratory frame. The T-BMT equation describes the change of the particle spin $\vec{S}$ with time under the influence of electromagnetic fields $\vec{B}\left(\vec{r},t\right), \vec{E}\left(\vec{r},t\right)$:

$$\frac{d}{dt}\vec{S} = \left(\vec{\Omega}_B + \vec{\Omega}_E\right) \times \vec{S}, \tag{4.8}$$

where $\vec{\Omega}_B\left(\vec{B},\vec{r},\vec{p},t\right)$ and $\vec{\Omega}_E\left(\vec{E},\vec{r},\vec{p},t\right)$ are the contributions from the magnetic and electric fields stated in eqs. 4.9 and 4.11, respectively.

The contribution from the magnetic field is

$$\vec{\Omega}_B\left(\vec{B},\vec{r},\vec{p},t\right) = -\frac{q}{m\gamma}\left(\left(1+a\gamma\right)\vec{B} - \frac{a\,\vec{p}\cdot\vec{B}}{\left(\gamma+1\right)m^2c^2}\,\vec{p}\right), \tag{4.9}$$

where γ is the relativistic Lorentz factor, c the vacuum speed of light and a the anomaly of the gyro-magnetic moment g. For electrons, the latter is [28]:

$$a \equiv \frac{g-2}{2} \approx 0.001159652 \tag{4.10}$$

The contribution from the electric field is

$$\vec{\Omega}_E\left(\vec{E},\vec{r},\vec{p},t\right) = \frac{q}{m\gamma}\cdot\frac{1}{mc^2}\left(a+\frac{1}{1+\gamma}\right)\vec{p}\times\vec{E}. \tag{4.11}$$

These contributions are listed here only for the sake of completeness, since there are no beamline elements with significant electric fields in the beam delivery system.

The expression for $\vec{\Omega}_B$ in eq. 4.9 can be decomposed in two parts for the field components $\vec{B}_\parallel$ parallel to $\vec{p}$ and $\vec{B}_\perp$ perpendicular to it:

$$\vec{\Omega}_B\left(\vec{B},\vec{r},\vec{p},t\right) = -\frac{q}{m\gamma}\left(\left(1+a\gamma\right)\vec{B}_\perp \;+\; \left(1+a\right)\vec{B}_\parallel\right) \tag{4.12}$$

Perpendicular magnetic fields affect the momentum $\vec{p}$ and the spin $\vec{S}$ very similarly $\left(\text{if } \vec{B}_\parallel = \vec{E} = 0\right)$:

$$\frac{d}{dt}\vec{p} = -\frac{q}{m\gamma}\left(\qquad\quad \vec{B}_\perp\right)\times\vec{p} \tag{4.13}$$

$$\frac{d}{dt}\vec{S} = -\frac{q}{m\gamma}\left(\left(1+a\gamma\right)\vec{B}_\perp\right)\times\vec{S} \tag{4.14}$$

Thus the spin vector precesses in a perpendicular magnetic field about $\vec{B}$ by the angle

$$\xi_{\text{spin}} = (1 + a\gamma)\ \xi_{\text{orbit}} \tag{4.15}$$

as sketched in figure 4.1, where ξ_{orbit} is the deflection angle of the particle. How to calculate ξ_{orbit} is explained in section 6.1.2. [10, 12]

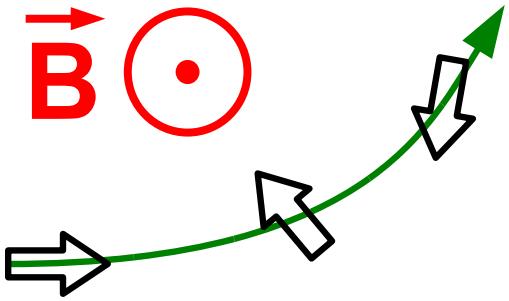

Figure 4.1: Spin rotation in a magnetic field. A charged particle is deflected in a magnetic field, the spin vector (⇒) precesses by a multiple of the deflection angle.

4.2.2 Spin Fan-Out

This section describes an effect caused by T-BMT precessions of different strengths which is referred to as "spin fan-out" in the following. Spin fan-out occurs in inhomogeneous magnetic fields or in the presence of a beam energy spread. Figure 4.2 illustrates spin fan-out using the example of a two-particle bunch traversing quadrupole magnets: Both particles are deflected into different directions in the first defocussing quadrupole and the spin vectors precess correspondingly according to eq. 4.15. Thus the longitudinal polarization decreases, but the transverse polarization remains zero since the transverse components of the two spin vectors cancel each other. Consequently, the entire polarization decreases: $|\vec{\mathcal{P}}'| < |\vec{\mathcal{P}}|$. This can be reversed by a focussing quadrupole which rotates the spin vectors back to the original orientation as shown in the right half of figure 4.2.

For a longitudinally polarized beam traversing a series of quadrupole magnets, the transport of the polarization can be described by a function f of the angular divergence θ_r, if the maximum polarization $|\vec{\mathcal{P}}|_{\text{max}}$ is obtained for $\theta_r \approx 0$ (as in figure 4.2):

$$f(\theta_r) = |\vec{\mathcal{P}}|_{\text{max}} \cdot \cos\big((1 + a\gamma) \cdot \theta_r\big), \tag{4.16}$$

where θ_r is used as measure for the fan-out of the momentum vectors, i. e. the defocussing of the beam. A possible beam energy spread is not taken into account by this function.

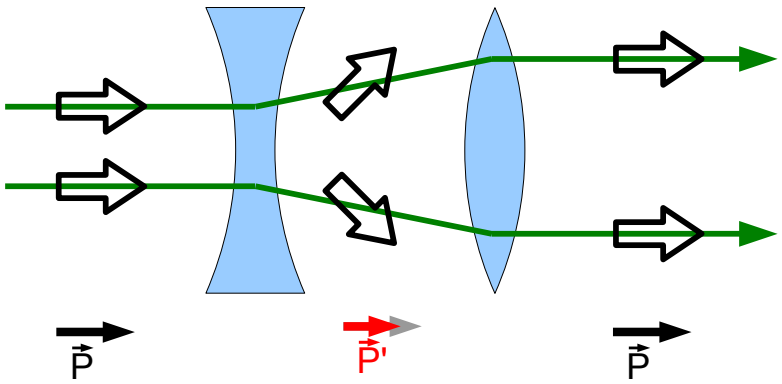

Figure 4.2: Illustration of the fan-out of spin vectors ($\Rightarrow$) in quadrupole magnets.

In presence of a beam energy spread, a similar behavior occurs (also in homogeneous magnetic fields), since the "amplification factor" $(a\gamma + 1)$ is energy-dependent. This fan-out is reversible as well.

So it might seem that polarization can be generated by spin fan-out, but that is actually not the case. Spin fan-out allows only to restore an existing ordering in the spin orientation which is "hidden" in a correlation between the spin orientation and the particle energy or a particle coordinate. It is not possible to restore polarization which got lost in stochastic processes like radiative depolarization, which will be introduced in the following section. Therefore, the term "spin fan-out" has been introduced here instead of "depolarization" to avoid confusion with the irrecoverable radiative depolarization.

4.2.3 Radiative Depolarization

When charged particles are deflected by electromagnetic fields, they emit electromagnetic radiation, which results in a loss of energy and a possible spin-flip. Depending on the circumstances, this radiation is called

- bremsstrahlung (slow-down radiation), if the particles are decelerated when they pass through matter. Bremsstrahlung is no issue in this study and therefore not further discussed here.

- beamstrahlung (beam radiation), if the particles are deflected in the electromagnetic field of the oncoming bunch during the collision at the beam-beam interaction point (IP). Beamstrahlung will be discussed in section 4.2.4.

- synchrotron radiation, if the particles are deflected in the fields of accelerator magnets. This kind of radiation will be discussed in the following.

The total radiation power P_γ of an electron (i. e. the average energy radiated off per time) with momentum $p = |\vec{p}|$ in a magnetic field $B = |\vec{B}|$ perpendicular to the momentum is (eq. 8.10 in [29])

$$P_\gamma(p, B) = \frac{2}{3} r_e m_e c^3 \frac{\beta^4 \gamma^4}{\rho^2} = \frac{2}{3} \frac{r_e q^2 c}{m_e} \beta^2 \gamma^2 B^2, \tag{4.17}$$

where q, m_e and $r_e \approx 2.818 \cdot 10^{-15}\,\mathrm{m}$ are the charge, the mass and the classical radius of the electron, respectively. c is the vacuum speed of light, $\rho = p/(qB)$ the bending radius in the magnetic field and β and γ are the relativistic Lorentz factors. Thus, the energy loss over a distance $\Delta s = s_1 - s_0$ is

$$\begin{aligned}\Delta E(p(s), B(s), \Delta s) = \int_{s_0}^{s_1} \frac{P_\gamma}{\beta c}\, ds &= \frac{2}{3} \frac{r_e q^2}{m_e} \int_{s_0}^{s_1} \beta\gamma^2 B^2\, ds \\ &= 3.304\,167 \cdot 10^{-13} \frac{\mathrm{GeV}}{\mathrm{T^2 m}} \int_{s_0}^{s_1} \beta\gamma^2 B^2\, ds. \end{aligned} \tag{4.18}$$

The number of photons radiated off along this distance is (eq. 8.93 in [29])

$$\begin{aligned} N(p(s), B(s), \Delta s) &= \int_{s_0}^{s_1} \frac{1}{\beta c} \frac{5}{2\sqrt{3}} \frac{\alpha c}{\rho} \gamma\, ds \\ &= \frac{5}{2\sqrt{3}} \frac{\alpha q}{m_e c} \int_{s_0}^{s_1} \frac{B}{\beta^2}\, ds \\ &= 6.179\,39 \frac{1}{\mathrm{Tm}} \int_{s_0}^{s_1} \frac{B}{\beta^2}\, ds, \end{aligned} \tag{4.19}$$

where α is the electromagnetic fine-structure constant. Depending on the initial spin state (up or down), there are two different probabilities[2] for a spin-flip at the emission of a photon. As it will be shown in chapter 9, the amount of depolarization due to synchrotron radiation is negligible. Therefore, only the larger of the two probabilities is calculated here. The spin-flip probability along the distance $\Delta s = s_1 - s_0$ is (eq. 2.23 in [30])

$$\begin{aligned} w_{\text{flip}}(p(s), B(s), \Delta s) &= \int_{s_0}^{s_1} \frac{1}{\beta c} \left(1 \pm \frac{8}{5\sqrt{3}}\right) \frac{5}{16}\sqrt{3}\, \frac{c\lambda\!\!\!^{-}_e r_e \gamma^5}{\rho^3}\, ds \\ &\leq \int_{s_0}^{s_1} \left(1 + \frac{8}{5\sqrt{3}}\right) \frac{5}{16}\sqrt{3}\, \lambda\!\!\!^{-}_e r_e \left(\frac{q}{m_e c}\right)^3 \frac{\gamma^2 B^3}{\beta^4}\, ds \\ &= 2.288\,0 \cdot 10^{-19} \frac{1}{\mathrm{T^3 m}} \int_{s_0}^{s_1} \frac{\gamma^2 B^3}{\beta^4}\, ds, \end{aligned} \tag{4.20}$$

where $\lambda\!\!\!^{-}_e \approx 3.862 \cdot 10^{-13}\,\mathrm{m}$ is the reduced electron Compton wavelength. The other symbols have already been introduced with eq. 4.17.

4.2.4 Beam-Beam Collision Effects

At the IP, the electron and positron bunches collide with each other. Apart from hard particle-particle interactions, which can be neglected here since only few occur per bunch crossing, each particle is deflected by the electromagnetic field of the other bunch as sketched in figure 4.3. The two colliding bunches tend to focus each other, which is denoted as *pinch effect*.

The polarization is again affected by T-BMT precession and radiative depolarization as explained in the following.

T-BMT Precession

For the beam parameters of the ILC, the following description from [31] can be used, which has been adapted to the variable names in this thesis (see chapter 3): for beams with Gaussian-shaped particle densities, the RMS[3]

[2] In storage rings, this difference gives rise to a polarization build-up along the magnetic field axis on timescales far beyond the flight time through the ILC beam delivery system.

[3] RMS = root mean square. This means actually the standard deviation of the distribution of deflection angles with mean value 0.

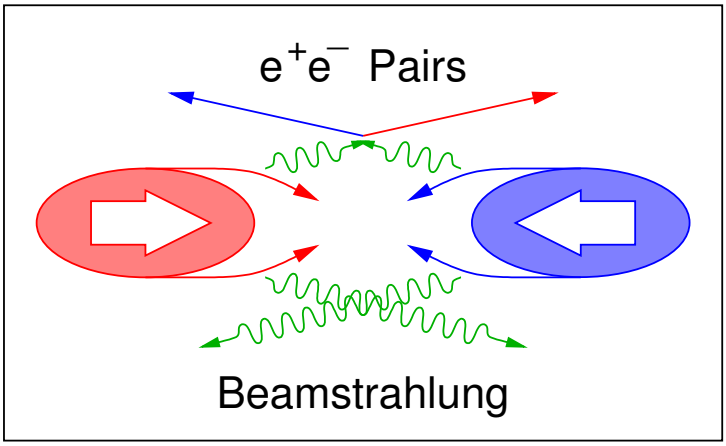

Figure 4.3: Illustration of the mutual focussing of the colliding bunches (pinch effect). The deflection of the bunch particles leads to T-BMT precession and emission of beamstrahlung. The beamstrahlung photons can recombine to e^+e^- pairs. [32]

deflection angles can be computed according to eq. 30 in [31] from the disruption parameters (see section 3.2.4):

$$\theta_j^{\mathrm{disr}} \approx \frac{1}{2}\frac{\sigma_j^{\mathrm{D}}}{\sigma_z^{\mathrm{D}}}\frac{D_j^{\mathrm{D}}}{\sqrt[6]{1+\left(D_j^{\mathrm{D}}/2\right)^5}} \quad (j=x,y) \tag{4.21}$$

Ignoring a possible correlation between the incident angle and the disruption angle, the angular divergence θ_j^{aft} after the collision is given by

$$\theta_j^{\mathrm{aft}} = \sqrt{\left(\theta_j^{\mathrm{disr}}\right)^2 + \left(\theta_j^{\mathrm{bef}}\right)^2} \quad (j=x,y,r)\,, \tag{4.22}$$

where θ_j^{bef} is the angular divergence before the collision. According to eq. 4.16, the corresponding spin fan-out is (eq. 31 in [31])

$$\begin{aligned} |\vec{\mathcal{P}}|^{\mathrm{bef}} - |\vec{\mathcal{P}}|^{\mathrm{aft}} &= |\vec{\mathcal{P}}|^{\mathrm{bef}} \cdot \left(1 - \cos\left((1+a\gamma)\cdot\theta_r^{\mathrm{aft}}\right)\right) \\ &\approx \frac{1}{2}|\vec{\mathcal{P}}|^{\mathrm{bef}} \cdot (1+a\gamma)^2 \cdot (\theta_r^{\mathrm{aft}})^2, \end{aligned} \tag{4.23}$$

where $|\vec{\mathcal{P}}|^{\mathrm{bef}}$ is the polarization before the collision and $|\vec{\mathcal{P}}|^{\mathrm{aft}}$ after the collision. For flat beams ($\sigma_x \gg \sigma_y$) and $D_x^{\mathrm{D}} \ll 1$ (both conditions are fulfilled at the ILC [16]), the contribution from the vertical dimension can be ignored.

Let Q denote the following relation between the polarizations before and after the collision and the luminosity-weighted polarization $|\vec{\mathcal{P}}|^{\text{lumi,1}}$ as introduced in section 4.1.2:

$$Q := \frac{|\vec{\mathcal{P}}|^{\text{bef}} - |\vec{\mathcal{P}}|^{\text{lumi,1}}}{|\vec{\mathcal{P}}|^{\text{bef}} - |\vec{\mathcal{P}}|^{\text{aft}}} \tag{4.24}$$

For $D_x^{\text{D}} \ll 1$, Q takes the value (eq. 16 in [31])

$$Q = \frac{2}{3}\frac{\ln(9/8)}{\ln(4/3)} = 0.273. \tag{4.25}$$

Merging eqs. 4.23 - 4.25, one obtains:

$$\begin{aligned} |\vec{\mathcal{P}}|^{\text{bef}} - |\vec{\mathcal{P}}|^{\text{lumi,1}} &= Q\left(|\vec{\mathcal{P}}|^{\text{bef}} - |\vec{\mathcal{P}}|^{\text{aft}}\right) \\ &\approx \frac{1}{4}\left(\frac{1}{2}|\vec{\mathcal{P}}|^{\text{bef}} \cdot (1+a\gamma)^2 \cdot (\theta_r^{\text{aft}})^2\right) \\ &= \frac{1}{2}|\vec{\mathcal{P}}|^{\text{bef}} \cdot (1+a\gamma)^2 \cdot \left(\frac{\theta_r^{\text{aft}}}{2}\right)^2 \end{aligned} \tag{4.26}$$

As explained in [33], one can interpret that as about half of the T-BMT precession occurring before the hard interaction. A comparison to eq. 4.23 implies that one can reproduce the luminosity-weighted polarization at a point behind the IP where the angular divergence has to be reduced by a factor 1/2 with respect to the divergence at the IP after the collision. This idea does however not take beamstrahlung effects into account.

Beamstrahlung

Contrary to the spin-flips caused by synchrotron radiation emission in the accelerator (cf. section 4.2.3), the spin-flips due to beamstrahlung emission cannot be neglected.

As presented in section 2.6.2 in [34], the *beamstrahlung parameter* Υ is a measure of the strength of the electromagnetic fields in the collision. Though the field strengths vary during the collision, a global value for the beamstrahlung parameter can be calculated as following:

$$\Upsilon_{\text{global}} \approx \frac{5}{6}\frac{\gamma\, r_e^2\, N_e}{\alpha\, \sigma_z^{\text{D}}\,(\sigma_x^{\text{D}} + \sigma_y)} \tag{4.27}$$

An approximate maximum value Υ_{max} occurring is

$$\Upsilon_{\text{max}} \approx \frac{12}{5}\Upsilon_{\text{global}} \tag{4.28}$$

A detailed description of the beamstrahlung-related effects on the polarization that are taken into account in the simulation in this thesis can be found in section 5.9 of [35].

Chapter 5

BDS Polarimetry at the ILC

To determine the polarization at the e^+e^- IP, the ILC design [7] foresees two laser Compton polarimeters per beam in the beam delivery system (BDS), as sketched in figure 5.1. Compton polarimeters are chosen especially because they allow an almost non-invasive measurement. The "upstream polarimeter" serves to measure the longitudinal polarization of the undisturbed beam as short as possible before the collision. The "downstream polarimeter" serves to measure the longitudinal polarization after the beam-beam collision in order to evaluate the effects of the collision on the polarization. The laser-bunch interaction points are located 1649 m in front of the IP and 148 m behind the IP, respectively. From these two measurements and the luminosity measurement, the average luminosity-weighted longitudinal polarization $\mathcal{P}_z^{\text{lumi}}$ is determined.

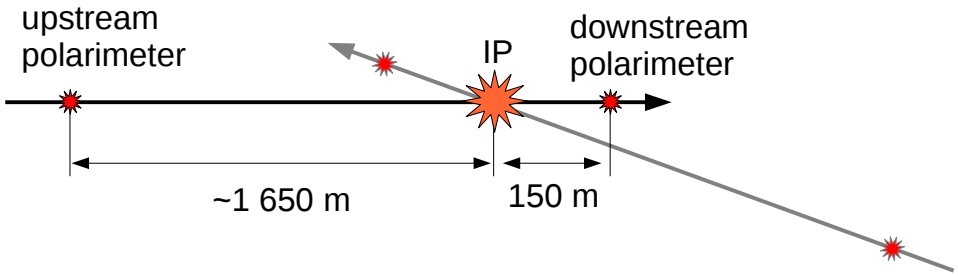

Figure 5.1: Positions of the laser-bunch interaction points of the polarimeters in the BDS (schematic view).

In this chapter, the methods to determine the polarization and their precision will be introduced.

5.1 Compton Polarimetry

The cross section of the Compton scattering process depends on the polarizations of the electron and the photon participating. This dependence is employed in a Compton polarimeter to measure the polarization of the electron beam. For that purpose, a circularly polarized laser is shot almost frontally (under a crossing angle $\vartheta_0 = 10\,\mathrm{mrad}$) into the electron beam.

5.1.1 Compton Scattering

The spin-dependent differential cross section of the Compton scattering process is given by

$$\frac{d\sigma}{dy_C} = \frac{2\pi r_e^2}{x_C}\left(a_C + \mathcal{P}_z \cdot \mathcal{P}_3^\gamma \cdot b_C\right), \tag{5.1}$$

using the following abbreviations:

$$\begin{aligned} y_C &:= 1 - \frac{E'}{E} \\ x_C &:= \frac{4EE_\gamma}{m_e^2}\cos^2\frac{\vartheta_0}{2} \\ a_C &:= \frac{1}{1-y_C} + 1 - y_C - 4r_C(1-r_C) \\ b_C &:= r_C x_C (1-2r_C)(2-y_C) \\ r_C &:= \frac{y_C}{x_C\,(1-y_C)} \end{aligned} \tag{5.2}$$

E, E_γ denote the electron/photon energy before the Compton scattering,
E', E'_γ denote the electron/photon energy after the Compton scattering,
m_e and r_e are the mass and the classical radius of the electron,
ϑ_0 is the crossing angle between electron and photon,
$\mathcal{P}_z$ is the longitudinal polarization of the electron and
$\mathcal{P}_3^\gamma$ denotes the circular polarization of the laser photon. For the definition of photon polarization see e. g. [36].

There are two characteristic points in the energy spectrum of the scattered electrons. First, the differential cross section (eq. 5.1) is independent of the polarization for the electron energy

$$E'_{\mathrm{crossover}} = \frac{E}{1 + x_C/2}, \tag{5.3}$$

since the polarization-dependent term in eq. 5.1 disappears at this energy. Second, the energy of the scattered electron is bounded from below for kinematic reasons. This boundary called *Compton edge* is given by:

$$E'_{\mathrm{min}} = \frac{E}{1 + x_C} \tag{5.4}$$

Figure 5.2 shows the differential cross section of the Compton scattering process versus the energy of the scattered electron assuming maximum polarization (a) and the position of the Compton edge versus the beam energy (b) for ILC-like conditions. For a beam energy $E = 250\,\mathrm{GeV}$, the Compton edge is located at $E'_{\mathrm{min}} = 25.5\,\mathrm{GeV}$ and the crossover point at $E'_{\mathrm{crossover}} = 46.3\,\mathrm{GeV}$ [37, 38].

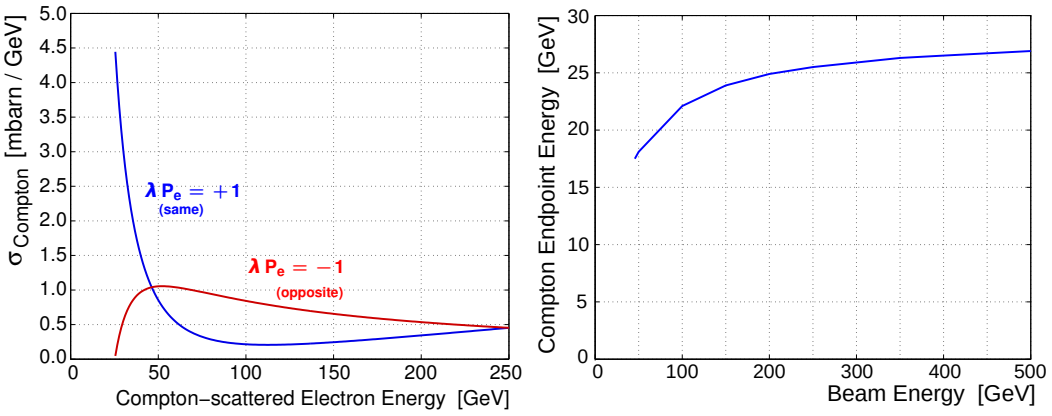

(a) (b)

Figure 5.2: Differential cross section $d\sigma/dE'$ of the Compton scattering process vs. the energy E' of the scattered electron for $\mathcal{P}_z\mathcal{P}_3^\gamma = \pm 1$ (denoted by λP_e in the figure) and electron beam energy $E = 250\,\mathrm{GeV}$ (a); Compton edge (Compton endpoint energy) E'_{min} vs. the electron beam energy E (b). In both cases, the laser photon energy is $E_\gamma = 2.3\,\mathrm{eV}$. Taken from figure 2 of [37] and modified.

5.1.2 Measurement Principles

For the ILC, it is planned to operate the polarimeters in the *multi-photon mode*, where ~ 1000 electrons per bunch crossing are scattered[1] . Compared to the bunch population N_e, this is a fraction of $\sim 10^{-7}$. Thus, the scattering

[1]The Compton scattering cross section and the number of scattered electrons are connected by the laser-bunch luminosity, which is described in detail in section 4.6 of [37].

changes the polarization at most by this amount, which is negligible with respect to the envisaged precision of 0.1 %. Therefore, this measurement is regarded as non-invasive.

For a measurement in the multi-photon mode, it is not feasible to measure the kinematic variables of the individual electrons. Instead, the numbers of scattered electrons for the two opposite laser polarizations are measured, which are denoted by $N^{\pm}$ for the same/opposite polarizations, i. e. $\mathcal{P}_z\mathcal{P}_3^\gamma = \pm 1$. These numbers give the *asymmetry* [38]

$$A = \frac{N^- - N^+}{N^- + N^+}. \tag{5.5}$$

The maximum possible asymmetry ($\mathcal{P}_z\mathcal{P}_3^\gamma = \pm 1$) is called the *analyzing power* Π. At the laser-bunch IP, it can be calculated from the differential cross sections:

$$\Pi = \frac{\int (D^- - D^+)\, dy_C}{\int (D^- + D^+)\, dy_C} \tag{5.6}$$

with

$$D^- := \frac{d\sigma}{dy_C}\Big|_{\mathcal{P}_z\mathcal{P}_3^\gamma = -1} \qquad D^+ := \frac{d\sigma}{dy_C}\Big|_{\mathcal{P}_z\mathcal{P}_3^\gamma = +1} \tag{5.7}$$

and y_C as introduced in eq. 5.2.

If the asymmetry has been measured and the analyzing power and the laser polarization are known and non-zero, the longitudinal polarization is given by

$$\mathcal{P}_z = \frac{A}{\mathcal{P}_3^\gamma \cdot \Pi}. \tag{5.8}$$

5.1.3 Polarimeters

The two BDS polarimeters per beam introduced above work both according to the same principles. The differences in the design of the two polarimeters are owed to the different beam properties before and after the collision.

Upstream Polarimeter

Figure 5.3 shows a schematic view of the upstream polarimeter. The laser-bunch interaction point (hereafter laser-bunch IP; not to be confused with the IP, which is the e^+e^- interaction point) is located in the middle of the magnetic chicane. The magnetic field of the chicane has been chosen to be constant. Thus, the horizontal position of the laser-bunch IP depends on the beam energy.

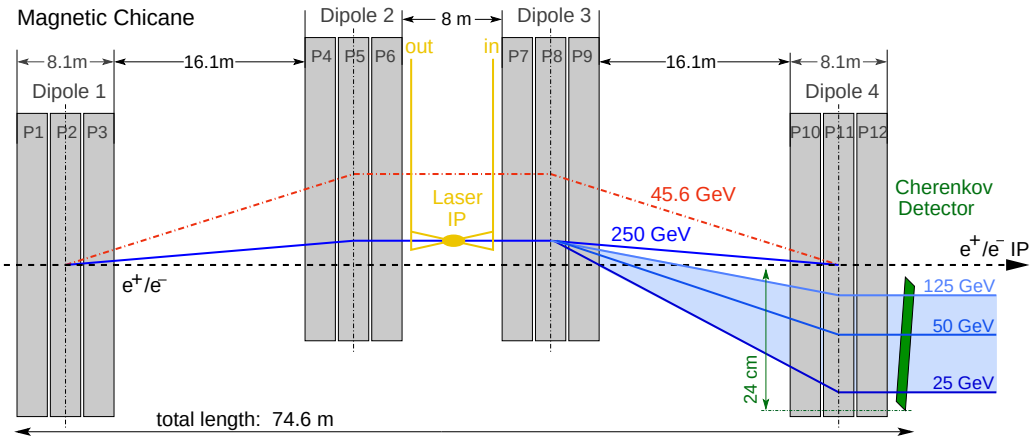

Figure 5.3: Schematic view of the upstream polarimeter. The chicane is set up in the horizontal plane. The path of the electron beam is displayed for two different beam energies (45.6 GeV and 250 GeV); for the latter, the fan of Compton-scattered particles branching off in dipole 3 is also drawn. [37]

The scattering angles of the electrons are $\lesssim 10\,\mu$rad (figure 4 in [38]). To separate them from the undisturbed beam, the magnetic chicane is employed, which also translates the energy distribution of the scattered electrons into a spatial distribution since particles with lower energy are bent more strongly. Behind the chicane, a Cherenkov detector is used to detect the scattered electrons in order to determine the asymmetry A. The foreseen detector consists of 20 gas-filled channels, in which the scattered electrons produce Cherenkov light, and of photomultiplier tubes to measure the amount of Cherenkov light. In principle, the longitudinal polarization can be determined separately from the asymmetry measured in each single channel, if the corresponding analyzing power is calculated for this channel accounting for the detector properties and especially for the energy range of the scattering electrons arriving in the respective channel.

Downstream Polarimeter

Figure 5.4 shows a schematic view of the extraction line up to the downstream polarimeter. The working principle of the downstream polarimeter is the same as for the upstream polarimeter. However, the beamstrahlung produced in the collision at the IP and the synchrotron radiation from the energy spectrometer chicane arrive at the downstream polarimeter as a fan with 15 cm radius. The Cherenkov detector of the downstream polarimeter needs to be located outside this fan to avoid a unacceptably large background

signal from the beamstrahlung photons. Therefore, the two magnets in the downstream polarimeter chicane behind the laser-bunch IP (BVEX3P and BVEX4P) overcompensate the beam orbit offset generated by the first two magnets (BVEX1P and BVEX2P), such that the scattered electrons are bent further away from the beamline.

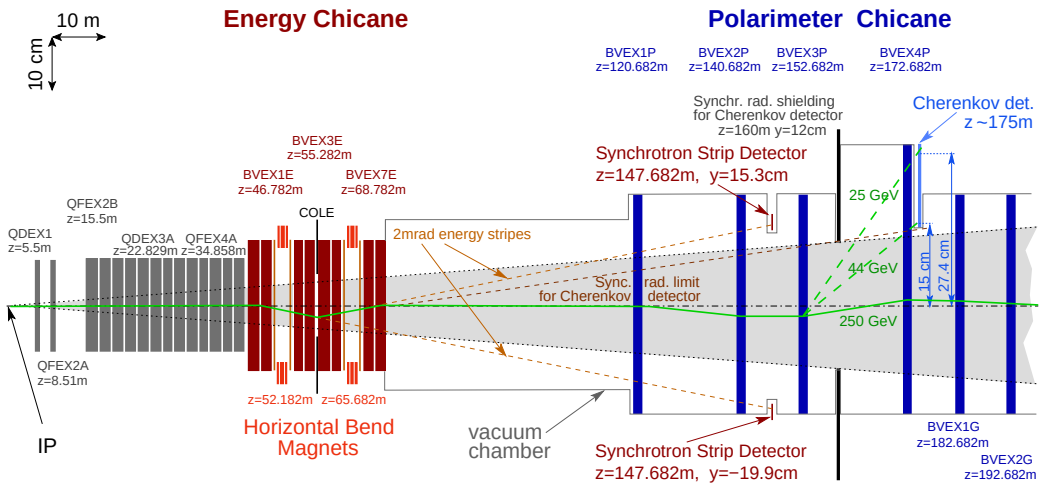

Figure 5.4: Schematic view of the extraction line up to the downstream polarimeter. The chicanes are set up in the vertical plane. The path of the electron beam is displayed for 250 GeV beam energy. The beamstrahlung fan from the IP and the synchrotron radiation fan from the energy chicane are also drawn. Taken from figure 4 of [39] and modified by D. Käfer.

In order to reproduce the luminosity-weighted polarization at the downstream polarimeter as explained in section 4.2.4, the lattice needs to be designed such that the angular divergence θ_x at the downstream polarimeter is half as large as at the IP and θ_y remains negligible with respect to θ_x. This has been implemented as follows:

The propagation of the particle coordinates

$$\boldsymbol{r}(s) = (x, \hat{p}_x, y, \hat{p}_y, z, \delta)^{\mathrm{T}} \tag{5.9}$$

is described in the linear approximation by the *transfer matrix* $\mathbf{R}$. For the propagation from the e^+e^- IP to (the laser-bunch IP of) the downstream polarimeter

$$\boldsymbol{r}(s_{\mathrm{DP}}) = \mathbf{R}(\mathrm{IP} \to \mathrm{DP}) \cdot \boldsymbol{r}(s_{\mathrm{IP}}), \tag{5.10}$$

$\mathbf{R}(\text{IP} \rightarrow \text{DP})$ has been computed from the lattice files (see section 7.1.1) to

$$\mathbf{R}(\text{IP} \rightarrow \text{DP}) = \begin{pmatrix} -2 & -0.001 & 0 & 0 & 0 & 0 \\ -0.049 & -0.5 & 0 & 0 & 0 & 0 \\ 0 & 0 & -8.524 & 0 & 0 & 0.02 \\ 0 & 0 & -0.067 & -0.117 & 0 & 0 \\ 0 & 0 & -0.001 & -0.002 & 1 & 10^{-4} \\ 0 & 0 & 0 & 0 & 0 & 1 \end{pmatrix} \tag{5.11}$$

and is identical for both the e^--and the e^+-beamline. The second row contains the contributions to θ_x at the downstream polarimeter. Since the beam is strongly focussed at the IP ($x \approx 0$), the element $\mathbf{R}_{21}$ can be neglected. The element $\mathbf{R}_{22}$ with $|\mathbf{R}_{22}| = 0.5$ reduces θ_x as desired.

Requirements to the Laser Systems

For an accurate determination of the luminosity-weighted longitudinal polarization, it is favorable to perform laser-bunch collisions for every single electron bunch. To obtain the envisaged statistical precision (see below), ~ 1000 electrons per bunch crossing need to be Compton-scattered at the upstream polarimeter. Depending on the intensity of the beamstrahlung background, this number might be larger for the downstream polarimeter.

For a measurement at the undisrupted beam (at the downstream polarimeter in absence of collisions and at the upstream polarimeter), a laser spot size similar to the beam size is favorable in order to minimize the required laser intensity. Earlier studies assume a transverse laser spot size of $50\,\mu$m (section 4.6 in [38]). For the disrupted beam with a much larger transverse extension, the impact of the laser spot size on the measurement accuracy is discussed in chapter 9.

A larger spot size requires a larger laser intensity in order to generate the required number of Compton scatterings per bunch crossing. Since such intense lasers might not feature the required pulse frequency to measure every single bunch, only three measurements per bunch train are foreseen at the downstream polarimeter. However, measuring every single bunch is still desirable, like it is foreseen at the upstream polarimeter.

Measurement Uncertainty

It is envisaged to achieve a systematic uncertainty of $\leq 0.25\,\%$ for each polarimeter. This uncertainty comprises the uncertainty of the polarization of the laser, the linearity of the detector and the knowledge of the analyzing power [37]. The highest precision as yet has been achieved at the SLD experiment with a systematic uncertainty of $0.5\,\%$ [5].

The statistical error is expected to be $< 1\,\%$ already for one minute of measurement time due to the large number of Compton-scattered electrons and the high bunch frequency.

For the alignment of the beams at the laser-bunch IPs with the the beam at the e^+e^- IP, a tolerance of $\sim 50\,\mu$rad has been demanded. This demand will be assessed in section 7.4.2.

5.2 Spin Transport

As explicated in section 5.1.3, the Compton polarimeters are expected to provide measurements with a systematic error of $\leq 0.25\,\%$ and a negligible statistical error ($\leq 0.1\,\%$) on timescales of hours. To extract the luminosity-weighted longitudinal polarization $\mathcal{P}_z^{\text{lumi}}$ at the IP from these measurements, one needs to know the polarization evolves along the path from the upstream polarimeter over the IP to the downstream polarimeter, which is the central question to be studied in this thesis.

In order not to increase the imprecision remarkably, the goal for the precision to which the spin transport needs to be understood has been set to $\leq 0.1\,\%$.

From the longitudinal polarization propagated to the IP and the luminosity, which can be measured to a precision of $\leq 0.1\,\%$ (section 8.7.2.2 in [7]), the $\mathcal{P}_z^{\text{lumi}}$ can be calculated according to eq. 4.6.

5.3 Determining the Polarization from Collision Data

As described in [40], an average value $\mathcal{P}_z^{\text{lumi}}$ of the luminosity-weighted longitudinal polarization of the colliding beams over many collisions can also be determined from polarization-dependent particle physics interactions at the IP, e. g. the process $e^-e^+ \to W^+W^-$. This provides a second measurement, which is independent of the polarimeters and the spin transport. In the following, the method of explained in more detail.

The moduli of the longitudinal luminosity-weighted polarizations can be calculated using a modified Blondel scheme, which requires the cross sections of $e^-e^+ \to W^+W^-$ to be measured for the four possible combinations of signs for the longitudinal luminosity-weighted polarizations, e. g.

$$(\mathcal{P}_z^{\text{lumi}}(e^-), \mathcal{P}_z^{\text{lumi}}(e^+)) = \{(+0.8, +0.3), (+0.8, -0.3), (-0.8, +0.3), (-0.8, -0.3)\}.$$

$$|\mathcal{P}_z^{\text{lumi}}(e^\pm)| = \sqrt{\frac{(\sigma_{-+} + \sigma_{+-} - \sigma_{--} - \sigma_{++})(\pm\sigma_{-+} \mp \sigma_{+-} + \sigma_{--} - \sigma_{++})}{(\sigma_{-+} + \sigma_{+-} + \sigma_{--} + \sigma_{++})(\pm\sigma_{-+} \mp \sigma_{+-} - \sigma_{--} + \sigma_{++})}}, \tag{5.12}$$

where σ_{ij} denotes the total cross section of $e^-e^+ \to W^+W^-$ with i and j being the signs of $\mathcal{P}_z^{\text{lumi}}$ of the positron and electron beams, respectively.

In addition, one can employ the distribution of $\cos\theta_W$, where θ_W is the angle between the electron beam axis and the direction of motion of the W^- boson. Figure 5.5 shows the statistical error of the longitudinal luminosity-weighted polarization of both beams determined using the modified Blondel scheme versus the size of the data set used ("positron/electron Blondel"). Equal shares for all combinations of signs are assumed. If a fit on $\cos\theta_W$ is

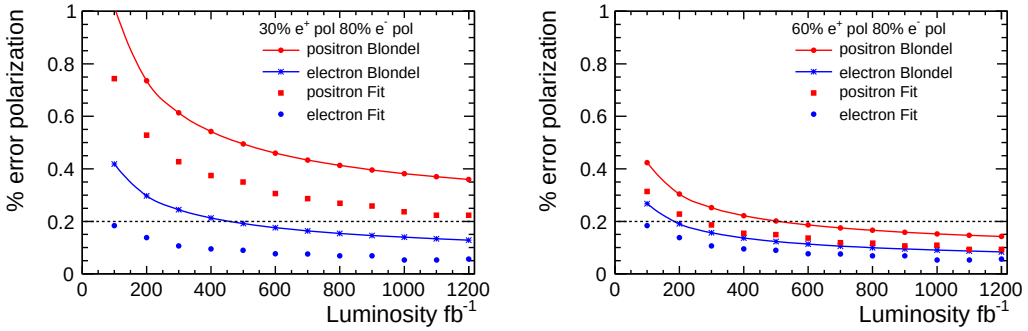

Figure 5.5: Statistical error of the longitudinal luminosity-weighted polarization versus the size of the data set expressed in terms of the integrated luminosity for 30 % (left) and 60 % (right) positron beam polarization. Taken from figure 5.14 in [40].

used in addition ("positron/electron Fit"), the additional information reduces the statistical error for a given data set.

It has been assumed that $|\mathcal{P}_z^{\text{lumi}}|$ is identical for both sign configurations, which can in reality only be assured up to the measurement uncertainty of the polarimeters. That introduces a systematic error [41], which mainly limits the achievable precision. Table 5.1 lists the total errors including this systematic error for a data set with an integrated luminosity of $500\,\text{fb}^{-1}$, which is foreseen to be collected during the first four years of operation assuming a measurement uncertainty of 0.25 % for the polarimeters. Again, equal shares for all combinations of signs are assumed.

However, both polarizations having the same sign suppresses the production of standard model particles, which might be undesired. If the share of the same-sign configurations is reduced, the statistical error rises.

$\lvert\mathcal{P}_z^{\text{lumi}}(e^-)\rvert$	$\lvert\mathcal{P}_z^{\text{lumi}}(e^+)\rvert$	$\frac{\Delta\mathcal{P}_z^{\text{lumi}}}{\mathcal{P}_z^{\text{lumi}}}(e^-)$	$\frac{\Delta\mathcal{P}_z^{\text{lumi}}}{\mathcal{P}_z^{\text{lumi}}}(e^+)$
0.8	0.3	0.16	0.35
0.8	0.6	0.16	0.17

Table 5.1: Errors of the luminosity-weighted longitudinal polarization determined from $500\,\text{fb}^{-1}$ data assuming a measurement uncertainty of $0.25\,\%$ for the polarimeters. Extracted from table 5.13 in [40].

In conclusion, employing W^+W^- scattering provides a direct access to $\mathcal{P}_z^{\text{lumi}}$ which yields a smaller systematic error, but a measurement over several years is necessary to push the total error (incl. the statistical error, see table 5.1) below $0.25\,\%$. Therefore, this method is not suitable to determine the longitudinal polarization for individual machine runs. However, the long-time measurement can be used to calibrate the Compton polarimeters or to verify the simulated spin transport from the polarimeters to the IP.

Chapter 6

Accelerator Simulation & Spin Transport

In this chapter, the basic principles of the beamline simulation used in this thesis (see section 7.1) are explained, especially the spin transport. An extensive description of the particle transport simulation can be found in [22].

6.1 Dipole Magnets

Magnets with a homogeneous dipole field are used to curve the beam trajectory.

6.1.1 Dipoles vs. Kicker Magnets

Bmad and several other accelerator simulations distinguish between dipole and kicker magnets, both of which are technically magnets with a dipole field, but are treated differently in the simulation: a dipole magnet bends the reference orbit (see section 3.1.1), whereas a kicker magnet does not. A dipole magnet is used where the beamline design foresees a curve, e. g. in rings or chicanes, whereas kicker magnets are used to adjust the actual beam trajectory. This function often implies that the magnetic field has to be altered on very short timescales, hence the name. Vice versa, a dipole magnet in the simulation being implemented as kicker does not automatically imply that the field strength can be altered on short timescales, but only that it does not affect the reference orbit.

6.1.2 Bending angle

The trajectory of a particle with charge q and momentum $p = |\vec{p}|$ in a transverse magnetic field with strength $B = |\vec{B}|$ is a circle with the radius

$$\rho = \frac{p}{B\,q}. \tag{6.1}$$

A useful quantity to express the effect of a dipole magnet on a given particle/beam is the *magnetic rigidity* $B\rho$. Assuming a constant magnetic field, the deflection angle of a particle/beam dipole magnet with length L is given by

$$\xi_{\text{orbit}} = \frac{L}{\rho} = \frac{BL}{B\rho} = \frac{BLq}{p}. \tag{6.2}$$

In the units used in this thesis and with $|q| = e$, it is given by

$$B\rho\,[\text{Tm}] = \frac{p\,[\text{eV}]}{c\,[\text{m/s}]}; \tag{6.3}$$

for an electron (beam) with the momentum $p = 250\,\text{GeV/c}$, it amounts to

$$B\rho = 250\,\frac{\text{GeV}}{c} = 833.9\,\text{Tm}. \tag{6.4}$$

For example, a magnet with an integrated field strength of 0.834 Tm would deflect such a beam by an angle of 1 mrad.

In the beamline coordinate system (see section 3.1.1), the bending angle ξ_{ref} of the reference orbit has to be subtracted from the individual bending angle ξ_{orbit} of a particle, if the involved magnet is a bending dipole magnet.

6.2 Quadrupole Magnets

Quadrupole magnets are used to focus the beam. Figure 6.1 displays a schematic view of a quadrupole magnet. The field of a quadrupole magnet is perpendicular to the beam axis and the magnetic field strength is proportional to the distance from the beam axis. Thus, a beam passing a quadrupole magnet oriented as shown in figure 6.1 is focussed in the horizontal plane and defocussed in the vertical plane. Several quadrupoles arranged in one line can yield a focussing effect in both planes.

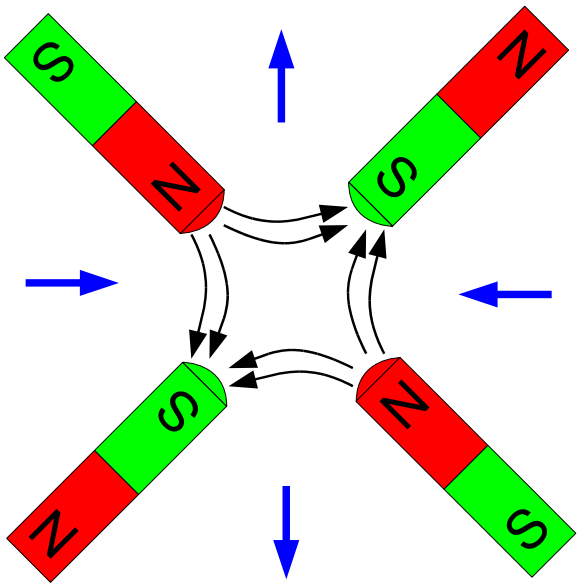

Figure 6.1: Quadrupole magnet (schematic view). The beam axis is perpendicular to the image plane; the reference orbit intersects the image plane in the center of the magnet. The bar magnets illustrate the configuration of the magnetic poles, the curved arrows indicate the orientation of the magnetic field and the straight arrows show the (de)focussing effect of the magnet on an electron beam going into the image.

6.3 Twiss Parameters

In linear particle tracking, it is convenient to express the parameters of a Gaussian-shaped beam for the transverse extensions by the so-called Twiss parameters (also referred to as Courant-Snyder functions) and the emittance (see e. g. chapter 2 of [34]). Since a different particle tracking method is used in this thesis, the Twiss parameters are used here only to generate the beams at the beginning of the BDS (cf. table 7.1) and for comparison with other studies.

In the horizontal direction, the Twiss parameters α_x, β_x and the emittance ε_x are related to the beam size σ_x, the angular divergence θ_x and the quantity

$\langle xx' \rangle$ as follows, if $\langle x \rangle = \langle x' \rangle = 0$:

$$\begin{aligned} \sigma_x^2 = \langle x^2 \rangle &= \varepsilon_x \, \beta_x \\ \langle xx' \rangle &= -\varepsilon_x \, \alpha_x \\ \theta_x^2 = \langle x'^2 \rangle &= \varepsilon_x \, \frac{(1+\alpha_x^2)}{\beta_x}. \end{aligned} \tag{6.5}$$

This works analogously for the vertical direction. The Twiss parameters β_x, β_y are not to be confused with the relativistic Lorentz-factor β.

6.4 Misalignments

Misalignments are deviations of the actual positions of beamline elements from the design positions. They can be static or time-dependent (ground motion).

They are parametrized here as shifts along the three spatial directions (x, y and z) and the rotations about the corresponding axes (for the coordinate system, see section 3.1.1). Following the Bmad manual [22] (chapter 4 "element attributes"), the three spatial misalignments are referred to as x-offset, y-offset and s-offset, and the rotations are referred to as x-pitch (rotation about the y-axis), y-pitch (rotation about the x-axis) and tilt (rotation about the z-axis). Internally, Bmad does not misalign the beamline elements, but shifts and rotates the beam particles correspondingly for every beamline element.

The first countermeasure against misalignments is a re-alignment of the magnets, which is assumed here to be already performed. Thus, the simulated misalignments are the remaining misalignments after the re-alignment.

Misaligned magnets affect the trajectory of the beam, which could lead without correction in the worst case to a beam loss. To avoid this, the beamline is equipped with a feedback orbit correction.

Further information on misalignments in view of the ILC and the planned countermeasures can be found in volume 3 of [6].

6.5 Feedback Orbit Correction

The functional principle of a feedback orbit correction (described e. g. in section 4.5.3 of [34]) is the following: there are several beam position monitors (BPMs) and correction dipole magnets implemented as kickers (see section 6.1.1) distributed along the beamline. The BPMs measure the positions of a bunch with respect to the design orbit (e. g. the center of a magnet the

BPM is mounted to). The correction dipoles are used to correct the trajectory; the required kicks for each magnet are computed from the measured beam positions and the design lattice. Depending on the response time of the system, the correction is applied to the next bunch or a later one.

If the misalignments are sufficiently small compared to the influence of the correction dipoles and vary slowly enough with time, this procedure ensures that the beam trajectory stays close to the design orbit and avoids a beam loss. Feedback correction is used during the operation of the accelerator to mitigate the effects of residual misalignments which could not be removed by magnet adjustment or to mitigate misalignments arising with time from ground motion, but it does not correct the misalignments of the magnets.

In this study, the required correction kicks are computed as follows: For each correction dipole, the *responses* at each BPM downstream, i. e. the changes in the transverse beam positions $\Delta\langle x\rangle$, $\Delta\langle y\rangle$ at a BPM for given kick angles $\Delta\langle x'\rangle$, $\Delta\langle y'\rangle$, are computed to the first order[1]. This can be expressed as a system of linear equations

$$\boldsymbol{b} = \mathbf{C} \cdot \boldsymbol{a} \tag{6.6}$$

where $\boldsymbol{b}$ and $\boldsymbol{a}$ are vectors containing the individual position changes $\Delta\langle x\rangle$, $\Delta\langle y\rangle$ and kick angles $\Delta\langle x'\rangle$, $\Delta\langle y'\rangle$, respectively, and $\mathbf{C}$ is the response matrix. Finding the desired kick angles for the orbit correction translates here to finding the vector $\boldsymbol{a}$ that minimizes $|\boldsymbol{b}|$ for a given $\mathbf{C}$. Typically, a beamline contains more BPMs than correction dipoles. Thus, $\mathbf{C}$ is not square and the system of equations is overdetermined. The method of choice to compute the desired kick angles under these conditions is *singular value decomposition* (SVD), which is described in section 2.9 of [42].

6.6 Spin Transport

The spin transport in Bmad is performed based on the T-BMT equation (see section 4.2.1 and [12, 22]). Since spin-orbit coupling is negligible for accelerators, the spin transport does not influence the particle transport. In favor of a fast computation, a SU(2)-representation is employed, which means that the polarization vectors of the macroparticles (see section 3.2.5) and the rotations are represented by spinors $\boldsymbol{\Psi}$ and by unit quaternions $\boldsymbol{d}$,

[1] The first-order responses correspond to the elements $\mathbf{R}_{12}$ and $\mathbf{R}_{34}$ of the *transfer matrix* $\mathbf{R}$ from the correction dipole position to the BPM position. See section 5.1.3 for an example for a transfer matrix.

respectively. In the following, the quaternions are written as real 4-vectors

$$\boldsymbol{d} = \begin{pmatrix} d_1 \\ d_2 \\ d_3 \\ d_4 \end{pmatrix} = \begin{pmatrix} \vec{d} \\ d_4 \end{pmatrix}, \tag{6.7}$$

where d_4 represents the real part of the quaternion and d_1, d_2 and d_3 the imaginary parts.

The spinor representation $\boldsymbol{\Psi}$ and the representation as three-dimensional vector $\vec{S}$ are related as follows:

$$\vec{S} = \boldsymbol{\Psi}^\dagger \vec{\boldsymbol{\tau}} \boldsymbol{\Psi} \tag{6.8}$$

where

$$\vec{\boldsymbol{\tau}} = \begin{pmatrix} \boldsymbol{\tau}_1 \\ \boldsymbol{\tau}_2 \\ \boldsymbol{\tau}_3 \end{pmatrix} \tag{6.9}$$

is the vector consisting of the Pauli matrices

$$\boldsymbol{\tau}_1 = \begin{pmatrix} 0 & 1 \\ 1 & 0 \end{pmatrix} \qquad \boldsymbol{\tau}_2 = \begin{pmatrix} 0 & -\imath \\ \imath & 0 \end{pmatrix} \qquad \boldsymbol{\tau}_3 = \begin{pmatrix} 1 & 0 \\ 0 & -1 \end{pmatrix}. \tag{6.10}$$

For the inverse transformation, it is more convenient to express $\vec{S}$ in spherical coordinates S, ϑ, ϕ:

$$\vec{S} = \begin{pmatrix} S_x \\ S_y \\ S_z \end{pmatrix} = S \begin{pmatrix} \sin\vartheta\cos\phi \\ \sin\vartheta\sin\phi \\ \cos\vartheta \end{pmatrix} \tag{6.11}$$

$\boldsymbol{\Psi}$ is then given by

$$\boldsymbol{\Psi} = \sqrt{S} \cdot e^{\imath\xi} \begin{pmatrix} \cos(\vartheta/2) \\ \sin(\vartheta/2) \cdot e^{\imath\phi} \end{pmatrix}, \tag{6.12}$$

where ξ is a complex phase without physical meaning.

A rotation about an axis $\vec{r}$ with $|\vec{r}| = 1$ by an angle α is represented by the unit quaternion

$$\boldsymbol{d} = \begin{pmatrix} -\vec{r} \cdot \sin(\alpha/2) \\ \\ \cos(\alpha/2) \end{pmatrix}. \tag{6.13}$$

The rotated spin $\boldsymbol{\Psi'}$ is computed by

$$\boldsymbol{\Psi'} = \left(d_4 \mathbb{1}_2 - \imath \left(\sum_{j=1}^{3} d_j \boldsymbol{\tau_j} \right) \right) \cdot \boldsymbol{\Psi} \tag{6.14}$$

where $\mathbb{1}_2$ is the 2-dimensional unity matrix and $\boldsymbol{\tau_{1,2,3}}$ are the Pauli matrices as above.

6.6.1 Existing Implementation in Bmad

At the beginning of this study, the the spin transport was implemented in Bmad as described in the following [12]:

- For dipole and quadrupole magnets, the quaternions calculated up to first order in the particle phase-space coordinates (see eq. 3.1) are taken from [43].
- For solenoids, Bmad simulates only the spin precession about the magnetic field neglecting any particle motion perpendicular to the magnetic field.
- For all other elements, the spins are left unchanged - apart from cavities, which do not appear in the ILC beam delivery system and are hence not relevant for this study. The crab cavities (section 8.1) are implemented in a different fashion.

6.6.2 Modifications

During the course of this study, the following modifications / additions have been made:

- Misalignments (see section 6.4), which could hitherto only applied to the particle transport, can now also be applied to spins. In the case of rotated beamline elements, the polarization vectors of the macroparticles are rotated correspondingly[2]. In the case of shifted beamline elements, no action is required, since shifts leave the spin invariant. The alteration of the particle coordinate accounts already for a possible change in the magnetic field the spin is exposed to, e. g. in a shifted quadrupole magnet.
- For kicker magnets (and dipoles implemented as such, see section 6.1.1) and beamline elements with additional kick components, a spin precession according to eq. 4.15 is applied, following the implementation for the particle transport in the Bmad_Standard tracking method [22]. Unlike for the spin transport through bending dipole magnets, this implementation does not take the particle coordinates (apart from the particle energy) into account.

[2]Since the polarization is expressed in the instantaneous rest frame of the particle (see section 4.1), there are no Lorentz boosts involved. Contrary to rotations due to T-BMT precession, the rotation angles are the same as for the particle coordinates.

- The spin transport through magnets of order 2 and higher (sextupoles, octupoles etc.) was not implemented since the corresponding quaternions are zero up to the first order in the particle coordinates. That means that these magnets affect mostly far-off-axis particles, which are more likely to appear in the case of misalignments. In order not to neglect the influence of these magnets completely, they are treated following the implementation of multipole elements in the Bmad_Standard tracking method: the multipole kick angles are computed (as described in section 10.2 "Magnetic Fields" in [22]) and the corresponding spin precession according to eq. 4.15 is applied.

The modifications listed above have been included in the official distribution of Bmad. Further modifications, which have not been included in the official version of Bmad, are the crab cavities (described in section 8.1) and the fringe field kicks of a tilted solenoid (described in section 8.2).

Chapter 7

Basic Simulation

In this chapter, the transport simulation for the particles and the spin is introduced and tested for the basic configuration as described by the RDR [15]. The propagation of the spin through the most common beamline elements is explained and the simulation is tested for consistency with the design values and for accuracy. Furthermore, a calculative correction for a possible incident angle is introduced.

7.1 Simulation and Initialization Parameters

The beam transport simulation is based on Bmad [21], which is a subroutine library for the transport simulation of relativistic charged particles in high-energy accelerators. The used version is distribution `bmad_dist_2012_0419_d` with the spin tracking code module `spin_mod.f90` taken from distribution `bmad_dist_2012_0511_d`, in which the spin transport through solenoids has been modified as explained in section 8.2.

If not stated otherwise, the Bmad_Standard tracking method is used for both the particle tracking and the spin tracking.

The simulation data have been processed with ROOT [44].

7.1.1 Lattice

For this study, the lattice `SB2009_Nov10` (see chapter 2), which was the latest available one at the time this simulation was carried out, is used with the following modification: in both the e^-- and the e^+-beamline, the last two final focus quadrupole magnets (QF1 and QD0) and all quadrupole magnets in the extraction line are split into 20 slices each instead of two slices. This does not mean a physical alteration of the beamline, but only makes the

simulation track the particles through those magnets in smaller steps than usual[1]. This additional slicing is motivated by computational reasons that are explicated in section 7.3.3. The modified version of the lattice is used throughout this thesis, unless the unmodified lattice is explicitly referred to. The transverse beam sizes and angular divergences are calculated from the emittances and the Twiss parameters of the lattice.

The simulation starts at the beginning of the respective lattice and is aborted at the downstream polarimeter because the further path down to the beam dump is irrelevant for polarization measurement.

7.1.2 Beam Initialization

The beams are generated by the Bmad routine `init_beam_distribution` (this routine is described extensively in appendix C.2 of [12]) with the parameters listed in table 7.1. As required by the used lattice, these correspond to the nominal parameter set from the RDR (table 2.6-1 in [16]). Since this requirement does not apply to the beam energy spread σ_E/E, the value from the TDR (table 8.2 in [7]) is used here instead. The beam sizes and angular divergences are generated from the emittances and the Twiss parameters of the lattice (cf. section 6.3). A Gaussian bunch shape is assumed. This is not quite accurate at the end of the main linac [45], but it will become apparent later that the size of the bunch, but not the exact shape is decisive for the spin transport.

The numbers of simulated macroparticles N_e^{macro} are chosen as compromise between the conscious usage of computing resources and the number of macroparticles required for an accurate simulation. If collision effects are simulated, 40 000 macroparticles are required, whereas 10 000 suffice for the transport simulation. Occasionally, the tracking method PTC [22] will be used instead of the Bmad_Standard tracking for comparison. Using PTC, only 1 000 macroparticles could be simulated due to the higher RAM consumption of PTC. Every sample consists of N_{rep} independent simulation runs with one bunch per simulation run. Therefore, no interaction between the bunches in a bunch train is taken into account and "beam" and "bunch" are mostly synonymous in this thesis. For every run, a new random seed is used.

The polarization vector of each macroparticle[2] is set manually to $\vec{\mathcal{P}} = (0, 0, +0.8)^T$ for the e^--beam and to $\vec{\mathcal{P}} = (0, 0, +0.3)^T$ for the e^+-beam.

[1] The author would like to thank Mathias Vogt (DESY) for this idea.

[2] The spin of a single particle would be described by a classical spin vector with norm 1. Since a macroparticle represents many particles, one can assign a polarization vector to it.

Parameter	symbol		e^--beam	e^+-beam
Nominal beam energy	E_0 [GeV]		250	
Number of repetitions	N_{rep}		1000	
Generated bunches			1	
Number of macroparticles	N_e^{macro}		1 000/10 000/40 000	
Number of particles	N_e		$2 \cdot 10^{10}$	
Horizontal normalized emittance	$\gamma_0 \varepsilon_x$	[μm]	9.4	
Vertical normalized emittance	$\gamma_0 \varepsilon_y$	[μm]	0.04	
Bunch length	σ_z	[μm]	300	
Beam energy spread (TDR)	σ_E/E	[10^{-3}]	1.24	0.7
Horizontal polarization	$\mathcal{P}_x$	[%]	0	
Vertical polarization	$\mathcal{P}_y$	[%]	0	
Longitudinal polarization	$\mathcal{P}_z$	[%]	+80	+30
Twiss parameters	β_x	[m]	72	
	β_y	[m]	40	
	α_x		-1.6	
	α_y		1.3	

Table 7.1: Beam parameters used to initialize the beams at the beginning of the beam delivery system (BDS). [7, 16]

Statistical fluctuations of the bunch polarization are not taken into account, since this study intends to investigate the measurement uncertainty for a bunch with a given polarization. For the initialization, it was assumed in lack of other information that there are no correlations of the polarization vectors with other parameters, e. g. the position in the bunch or the particle energy. In that case, the individual spin configuration for a bunch with a given polarization is irrelevant.

7.1.3 Statistical Uncertainties on the Bunch Parameters

The simulation output is presented in this thesis usually as the mean value over the N_{rep} runs in a sample $\pm$ the sample standard deviation. The sample standard deviation is not to be confused with the error on the mean value, which is a factor $1/\sqrt{N_{\text{rep}}}$ smaller.

Several bunch parameters are already mean values or sample standard deviations of subsamples, like $\langle x \rangle$ and σ_x where the subsample is the hor-

izontal particle positions x in one bunch, which is used as example in the following. The number of macroparticles per bunch N_e^{macro} determines the statistical uncertainty on the bunch parameters. For Gaussian-distributed quantities, the uncertainty on the the mean value is given by

$$\Delta \langle x \rangle = \frac{\sigma_x}{\sqrt{N_e^{\text{macro}}}}. \tag{7.1}$$

The uncertainty on the sample standard deviation is

$$c_{\text{low}}(p_{\text{err}}, N_e^{\text{macro}})\sigma_x \leq \sigma_x \leq c_{\text{high}}(p_{\text{err}}, N_e^{\text{macro}})\sigma_x, \tag{7.2}$$

where p_{err} is the chosen probability of error, which is here $p_{\text{err}}^{1\,\sigma} \approx 1-0.683$ corresponding to a statistical significance of 1 standard deviation. The relative statistical uncertainties $c_{\text{low}}(p_{\text{err}}, N_e^{\text{macro}})$, $c_{\text{high}}(p_{\text{err}}, N_e^{\text{macro}})$ are

$$\begin{aligned} c_{\text{low}}(p_{\text{err}}, N_e^{\text{macro}}) &:= \sqrt{\frac{N_e^{\text{macro}} - 1}{\chi^2_{p_{\text{err}}/2;N_e^{\text{macro}}-1}}} - 1 \\ c_{\text{high}}(p_{\text{err}}, N_e^{\text{macro}}) &:= \sqrt{\frac{N_e^{\text{macro}} - 1}{\chi^2_{1-p_{\text{err}}/2;N_e^{\text{macro}}-1}}} - 1, \end{aligned} \tag{7.3}$$

$$\tag{7.4}$$

where $\chi^2_{p;n}$ denotes the quantile for the probability p of the χ^2-distribution with n degrees of freedom. Table 7.2 lists the relative statistical uncertainties for the values of N_e^{macro} that appear in this thesis [46]. Since $c_{\text{low}} \approx -c_{\text{high}}$ in all these cases, the upper and the lower error are not distinguished in the following.

N_e^{macro}	c_{low}	c_{high}
1 000	−0.021 64	0.023 14
10 000	−0.006 997	0.007 147
40 000	−0.003 517	0.003 554
100 000	−0.002 229	0.002 244

Table 7.2: Relative statistical uncertainties $c_{\text{low}}(p_{\text{err}}, N_e^{\text{macro}})$, $c_{\text{high}}(p_{\text{err}}, N_e^{\text{macro}})$ on the sample standard deviation for $p_{\text{err}}^{1\,\sigma}$ and different values of N_e^{macro}.

Therefore, the standard deviations on bunch parameters that present already a mean value or a standard deviation of a subsample should obey to the equations above, if the samples follow a Gaussian distribution. This can be used as cross-check for the correctness of the simulation or as indicator, whether a sample is Gaussian-distributed.

7.2 Particle Transport

The parameters of the simulated bunches at the IP and the laser-bunch IPs of the polarimeters are now confronted with the corresponding design values from the ILC RDR [16] and with the requirements for measuring the polarization. The polarization itself is discussed in the following section (7.3).

7.2.1 IP: Comparison with the Design Parameters

The bunch parameters at the IP and the corresponding design values are listed in table 7.3. Each sample consists of 1000 runs with $N_e^{\mathrm{macro}} = 10\,000$ macroparticles per bunch. Stated are the mean values of the bunch parameters $\pm$ their standard deviations. In the upper part of table 7.3, the beam parameters and their relative deviations ("dev.") from the corresponding design values are listed. For the parameters in the lower part, the design values are zero by default; therefore, the values are expressed as fractions ("fr.") of the corresponding spreads, e. g. $\langle x \rangle / \sigma_x$, $\langle x' \rangle / \theta_x$, $\langle \delta \rangle / (\sigma_E / E)$. In operation, the beam parameters can be adjusted by tuning the correction magnets and the focussing quadrupoles, which allows for differences of $\sim 10\,\%$ between the design values and the simulation output. The beam-beam crossing angle (see section 3.1.2) is not taken into account here; the corresponding bunch rotation is introduced in section 8.1. Therefore, the design value of 639 nm for the horizontal beam size applies in this chapter to σ_x and not to σ_x^{D}.

To show that such a variation does not affect the polarization significantly, a sample with 21 % larger emittances ε_x, ε_y has been generated, whose bunch parameters are listed in table 7.3 as well. The effect on the polarization is discussed in section 7.3.4. For the samples with the nominal emittance, most of the parameters agree to a level of $\lesssim 1\,\%$ with the design values, apart from the angular divergences θ_x and θ_y, which deviate by up to $\lesssim 4\,\%$ from the design values, which is still acceptable. The horizontal bunch position $\langle x \rangle$ is ≈ 3 standard deviations off the design orbit, which might be caused by non-linear terms in the particle transport of this simulation. However, in relation to the horizontal beam size σ_x, the deviation is only $\approx 3\,\%$, which is sufficiently small. For the sample with enlarged emittances, one expects increases in the beam sizes σ_x, σ_y and angular divergences θ_x, θ_y by 10 % (eq. 6.5). The simulated bunch parameters meet this expectation to the same level as the sample with the design emittance.

parameter		design value	e^--beam value	e^--beam dev. [%]	e^+-beam value	e^+-beam dev. [%]	e^--beam, $\varepsilon = 1.21\,\varepsilon_{\text{nom}}$ value	e^--beam, $\varepsilon = 1.21\,\varepsilon_{\text{nom}}$ dev. [%]
σ_x	[nm]	639.0	640 ± 4		637 ± 4		704 ± 5	10.24
σ_y	[nm]	5.7	5.72 ± 0.04		5.73 ± 0.04		6.30 ± 0.04	10.44
σ_z	[mm]	0.3	0.300 ± 0.002		0.300 ± 0.002		0.300 ± 0.002	
θ_x	[μrad]	32.0	32.3 ± 0.2	1.09	30.9 ± 0.2	-3.36	35.2 ± 0.2	9.97
θ_y	[μrad]	14.0	14.4 ± 0.1	2.56	14.3 ± 0.1	2.15	15.8 ± 0.1	12.88
σ_E/E (e^-)	[10^{-3}]	1.24	1.240 ± 0.009				1.240 ± 0.009	
σ_E/E (e^+)	[10^{-3}]	0.7			0.700 ± 0.005			
ε_x	[pm]	20.5	20.7 ± 0.2		19.7 ± 0.2	-3.90	24.8 ± 0.2	20.89
ε_y	[fm]	79.8	82.1 ± 0.8	2.94	82.0 ± 0.8	2.71	99.5 ± 1.0	24.65
parameter			value	fr. [%]	value	fr. [%]	value	fr. [%]
$\langle x \rangle$	[nm]		-22 ± 6	3.49	19 ± 6	3.03	-27 ± 7	3.83
$\langle y \rangle$	[nm]		-0.00 ± 0.06		-0.00 ± 0.06		0.00 ± 0.06	
$\langle z \rangle$	[nm]		$82 \pm 3\,053$		$107 \pm 2\,951$		$-12 \pm 3\,055$	
$\langle x' \rangle$	[μrad]		-0.3 ± 0.3	1.07	0.3 ± 0.3		-0.4 ± 0.4	1.11
$\langle y' \rangle$	[μrad]		-0.0 ± 0.1		0.0 ± 0.1		0.0 ± 0.2	
$\langle \delta \rangle$	[10^{-3}]		0.00 ± 0.01		0.000 ± 0.007		0.00 ± 0.01	

Table 7.3: Comparison of the parameters of the simulated bunches with design values at the IP [7, 16]. The parameters are introduced in section 3.2. "dev." is the relative deviation of the simulated parameter from the design value. The bunch positions and angles are also given as fraction ("fr.") of the corresponding bunch sizes and divergences, resp, e. g. $\langle x \rangle$ in terms of σ_x or $\langle \delta \rangle$ in terms of σ_E/E. Deviations/fractions below 1 % are omitted for better readability. The beam-beam crossing angle is not taken into account here. Each sample consists of 1000 runs with $N_e^{\text{macro}} = 10\,000$ macroparticles per bunch. Stated are the mean values of the bunch parameters $\pm$ the sample standard deviations. The two right columns show the parameters for a sample that has been initialized with emittances ε_x, ε_y that are 21 % larger than the design values.

7.2.2 Bunch Parameters at the Polarimeters

Table 7.4 lists selected bunch parameters at the laser-bunch IPs of the upstream polarimeters and the downstream polarimeters. For the upstream polarimeter, there are no design values specified as for the IP, but the polarization measurement requires the bunch to be sufficiently small for the interaction with the laser beam of the polarimeter (cf. chapter 5). The laser-bunch IP at the downstream polarimeter is the second focal point in the lattice in order confine even the disrupted bunches after a bunch-bunch-collision as much as possible such that a polarization measurement can be performed.

position	parameter		e^--beam	e^+-beam
UP	σ_x	[μm]	31.6 ± 0.2	24.1 ± 0.2
	σ_y	[μm]	3.19 ± 0.02	3.14 ± 0.02
	σ_z	[mm]	0.300 ± 0.002	0.300 ± 0.002
	θ_x	[μrad]	0.985 ± 0.007	0.980 ± 0.007
	θ_y	[μrad]	$0.025\,7 \pm 0.000\,2$	$0.026\,0 \pm 0.000\,2$
	σ_E/E	[10^{-3}]	1.240 ± 0.009	0.700 ± 0.005
	$\langle x \rangle$	[μm]	-0.1 ± 0.3	-0.0 ± 0.2
	$\langle y \rangle$	[μm]	-0.00 ± 0.03	0.00 ± 0.03
	$\langle z \rangle$	[nm]	$87 \pm 3\,053$	$109 \pm 2\,951$
	$\langle x' \rangle$	[μrad]	-0.006 ± 0.010	0.00 ± 0.01
	$\langle y' \rangle$	[μrad]	$-0.000\,0 \pm 0.000\,3$	$0.000\,0 \pm 0.000\,3$
	$\langle \delta \rangle$	[10^{-3}]	0.00 ± 0.01	0.000 ± 0.007
DP	σ_x	[μm]	9.7 ± 0.2	5.17 ± 0.08
	σ_y	[μm]	25.2 ± 0.2	14.2 ± 0.1
	σ_z	[mm]	0.300 ± 0.002	0.300 ± 0.002
	θ_x	[μrad]	16.2 ± 0.1	15.5 ± 0.1
	θ_y	[μrad]	1.69 ± 0.01	1.68 ± 0.01
	σ_E/E	[10^{-3}]	1.240 ± 0.009	0.700 ± 0.005
	$\langle x \rangle$	[μm]	3.3 ± 0.1	-1.07 ± 0.05
	$\langle y \rangle$	[μm]	-0.0 ± 0.2	-0.0 ± 0.1
	$\langle z \rangle$	[nm]	$19 \pm 3\,053$	$50 \pm 2\,951$
	$\langle x' \rangle$	[μrad]	0.2 ± 0.2	-0.2 ± 0.2
	$\langle y' \rangle$	[μrad]	0.00 ± 0.02	-0.00 ± 0.02
	$\langle \delta \rangle$	[10^{-3}]	0.00 ± 0.01	0.000 ± 0.007

Table 7.4: Selected bunch parameters at the upstream polarimeter (UP) and the downstream polarimeter (DP).

As required by the lattice design (see section 5.1.3), θ_x at the downstream polarimeter is half as large as at the IP, and $\theta_y \ll \theta_x$.

The transverse bunch sizes at the polarimeters range from few micrometers to few ten micrometers. A laser pulse with a spot size of $\sim 50\,\mu$m as foreseen in section 4.6 of [38] would cover the entire bunch and uses the laser power efficiently since the laser spot is not much broader than the electron bunch. However, in this case the sizes and the shape of the electron bunch have to be taken into account when the luminosity of the collision of the laser pulse with the electron bunch is calculated, which was not necessary in [38] for the TESLA beam parameters. The bunch length σ_z corresponds to a time of $\sigma_z/c = 1\,$ps, which is smeared by the spread of $\langle z \rangle$. This spread originates here mainly from the bunch initialization (see section 7.1.2 and eq. 7.1), since the simulation hardly alters z for particles moving with practically light speed. Possible influences from the beam source or the main linac are not taken into account in this thesis. Therefore, $\langle z \rangle$ and σ_z should be seen here rather as underlying assumptions than as simulation results. In contrast, the other bunch parameters provide significant information, since they are altered substantially by the simulation.

The laser-bunch IP of the upstream polarimeter is not a focal point, in contrast to the laser-bunch IP of the downstream polarimeter (cf. section 2.2). Therefore, the angular divergences at the upstream polarimeter are small compared to those at the IP and the downstream polarimeter. The mean bunch positions and angles are negligible with respect to the sizes and angular divergences, apart from $\langle x \rangle$ at the downstream polarimeter, which however does not change the picture for a $50\,\mu$m wide laser spot.

7.3 Spin Transport

In this section, the spin transport along the BDS is explained and the effects of dipole and quadrupole magnets are explicated, the employed spin tracking methods and the lattice modifications are tested for accuracy and the tolerances towards changes in the bunch parameters are investigated.

The longitudinal and entire polarization along the BDS is shown in figure 7.1 and a magnified view of the region around IP and downstream polarimeter in figure 7.2. This figure displays also the function $f(\theta_r)$ of the angular divergence, which will be discussed below in section 7.3.2. The error bands indicate the standard deviations of the polarizations at the respective points. Since the beams are initialized with an exact value for the polarization, the standard deviations reflect only differences in the particle transport due to the random fluctuations of the particle positions and momenta.

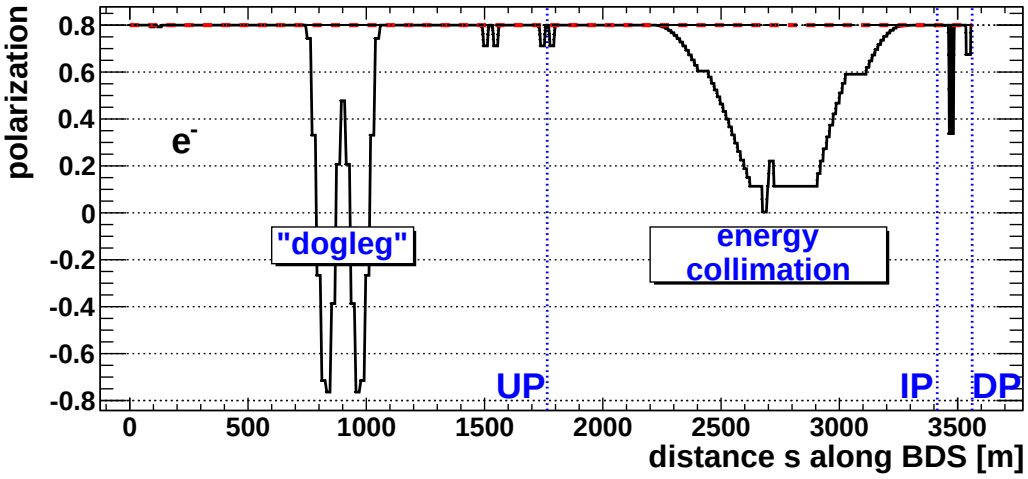

(a)

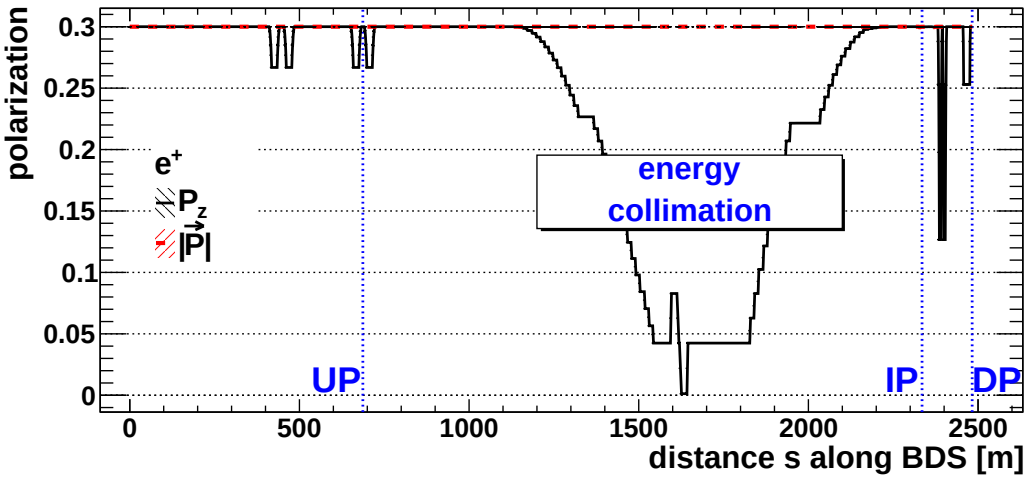

(b)

Figure 7.1: Longitudinal polarization $\mathcal{P}_z$ (black, solid) and entire polarization $|\vec{\mathcal{P}}|$ (red, dashed) of the electron beam along the BDS (a), accordingly for the positron beam (b). The positions of the upstream polarimeter (UP), the interaction point (IP) and the downstream polarimeter (DP) are flagged.

The spin transport in the fields of the beamline magnets is described by T-BMT precession (section 4.2.1). As eq. 4.8 shows, the absolute change in polarization is proportional to the degree of polarization, i. e. the relative changes do not depend on it. Thus, possible differences would originate from differences in the beamline or the different beam energy spreads. As figures 7.1 and 7.2 show, these differences are negligible with respect to the envisaged precision of 0.1 % for this study (see section 5.2). Therefore, only the

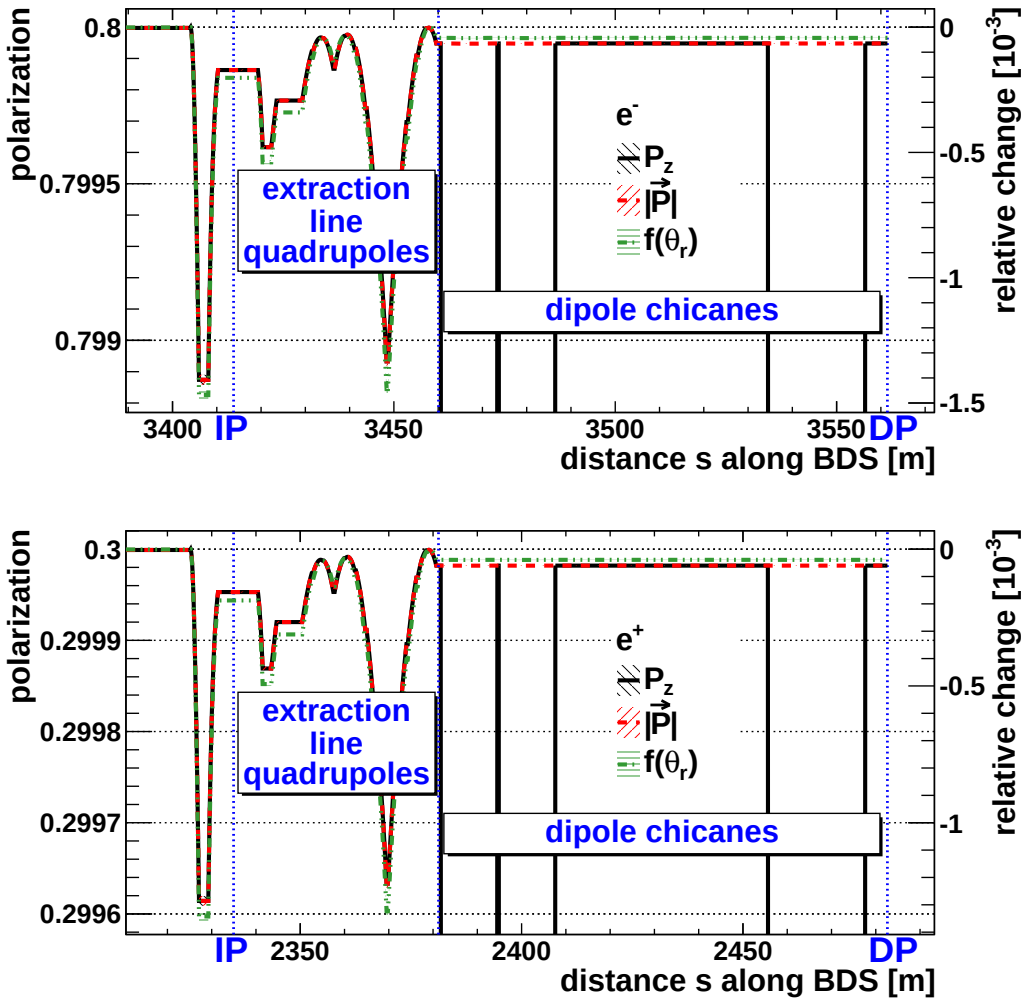

Figure 7.2: Longitudinal polarization $\mathcal{P}_z$ (black, solid), entire polarization $|\vec{\mathcal{P}}|$ (red, dashed) and the function $f(\theta_r)$ of the angular divergence defined in eq. 7.8 (green, dash-dotted) of the electron beam between IP and downstream polarimeter (a), accordingly for the positron beam (b). In contrast to figure 7.1, this figure shows the extraction line in detail.

electron beam will be discussed in the following, since it is more uncertainty-prone due to the larger energy spread and the additional beamline section for the positron beam generation.

The most obvious feature in figures 7.1 and 7.2 are several dips in the longitudinal polarization, whereas the entire polarization remains unchanged at those positions. This behavior is caused by a rotation of the polariza-

tion vector in a dipole magnet. Figure 7.2 shows also uniform changes in the longitudinal and entire polarization around the IP, which are caused by quadrupole magnets. The effects of these two magnet types, which are the most common ones in the lattice, are explained in more detail below.

7.3.1 Effects of Dipole Magnets

Since the field of a dipole magnet is homogeneous, one can assume that all spins experience the same fields along the same distance if σ_x, σ_y, θ_x and θ_y are sufficiently small, even though the ILC BDS comprises sector-shaped dipole magnets. To account for the rotation ξ_{ref} of the reference orbit, eq. 4.15 needs to be modified. $\xi_{\text{orbit}} = \xi_{\text{ref}}/(1+\delta)$ denotes here the deflection angle for a single particle with the energy $E = (1+\delta) \cdot E_0$. The resulting spin precession angle is

$$\begin{aligned}
\xi_{\text{spin}} &= (1 + a\gamma) \cdot \xi_{\text{orbit}} - \xi_{\text{ref}} \\
&= (1 + a\ (1+\delta)\ \gamma_0) \cdot \frac{\xi_{\text{ref}}}{(1+\delta)} - \xi_{\text{ref}} \\
&= \left(a\gamma_0 - \frac{\delta}{1+\delta} \right) \cdot \xi_{\text{ref}}, \qquad (7.5)
\end{aligned}$$

where a is the anomalous gyro-magnetic moment of the electron and γ the relativistic Lorentz factor. For 250 GeV-electrons, the "amplification factor" is

$$a\gamma_0 = a\frac{E_0}{m_e} \approx 567, \qquad (7.6)$$

whereas $\delta \sim \sigma_E/E \ll 1$, so the term $\delta/(1+\delta)$ can be neglected for now. Then all spin vectors and thus also the polarization vector precess by the same angle

$$\xi_{\text{spin}} = a\gamma_0\, \xi_{\text{ref}} = a\gamma_0\, \frac{BL}{B\rho}, \qquad (7.7)$$

where B the field strength of the magnet, L its length and $B\rho$ the magnetic rigidity of the beam (see section 6.1.2)

In figure 7.1a, the largest precession of the polarization occurs in the dogleg (cf. section 2.2) between $s \approx 700\,\text{m}$ and $s \approx 1\,100\,\text{m}$. At $s = 900\,\text{m}$, the reference orbit is bent by 0.54° with respect to the original direction of the beamline. According to eq. 7.7, the polarization vector should precess by $\vartheta_{\text{pol}} = a\gamma_0 \cdot 0.54° = 306°$, which results in a longitudinal polarization of $|\vec{\mathcal{P}}| \cdot \cos\vartheta_{\text{pol}} \approx 0.48$ as seen in figure 7.1a. For $\vartheta_{\text{pol}} = 180°$, the $\mathcal{P}_z$ takes the value $\mathcal{P}_z = -|\vec{\mathcal{P}}| \approx -0.8$, which is not displayed accurately in figure 7.1a since the graphs consist of discrete data points (one at the end of each beamline

element) connected with a straight line. Likewise, the polarization vector precesses in the other double curves and chicanes.

The precession can be reversed by one or more other dipoles bending the beam back to its original direction, such that the beam would leave a double curve or a chicane with the same spin configuration as it entered it.

7.3.2 Effects of Quadrupole Magnets

As described in section 4.2.2, quadrupole magnets cause the spin vectors to fan out, which leads to a reversible loss of (entire!) polarization (see section 4.2.2). Figure 7.2 shows such a behavior in the last final focus quadrupoles (10-3 m in front of the IP) as well as in the quadrupoles in the extraction line (5-46 m behind the IP). To demonstrate that the changes in polarization stem from the spin fan-out, the function $f(\theta_r)$, which has already been introduced in section 4.2.2, is also drawn in figure 7.2:

$$f(\theta_r) = |\vec{\mathcal{P}}|_{\max} \cdot \cos\left(\left(a\gamma_0\big(1 + \langle\delta\rangle\big) + 1\right) \cdot \theta_r\right) \tag{7.8}$$

γ has been replaced by $\gamma_0(1+\langle\delta\rangle)$. $|\vec{\mathcal{P}}|_{\max} = 0.8$ is here the initial polarization for the e^--beam and $|\vec{\mathcal{P}}|_{\max} = 0.3$ for the e^+-beam. At the beginning of the lattice, the angular divergence is $\theta_r \approx 1\,\mu$rad. This angular divergence has not been taken into account for the initialization of the polarization vectors of the macroparticles. However, this deviation is sufficiently small in relation to the θ_r at the IP and in the extraction line to fulfill the requirements stated in section 4.2.2. Furthermore, the beam energy spread is negligible in absence of collisions, such that $f(\theta_r)$ should provide a good approximation of the (entire) polarization. As figure 7.2 shows, $f(\theta_r)$ describes the propagation through the quadrupole magnets to a precision $\lesssim 0.01\,\%$, which explains the behavior of the polarization in the extraction line.

7.3.3 Spin Tracking Accuracy

After the qualitative behavior of the polarization has been explained now, the precision of the spin transport simulation and the effect of the modification of the original lattice are evaluated in the following. Figure 7.3 shows the longitudinal polarization of the e^--beam along the extraction line for three different combinations of lattice files and tracking methods:

- The Bmad_Standard tracking method on the original lattice files, labeled "BStd org". $N_e^{\text{macro}} = 10\,000$ particles.

- The Symp_Lie_PTC tracking method (see [22]) on the original lattice files, labeled "PTC org". This method is more exact than Bmad_Standard, but disfavored here due to its large consumption of computing resources. $N_e^{\text{macro}} = 1\,000$ particles due to the large resource consumption.

- The Bmad_Standard tracking method on the modified lattice files (sliced quadrupole magnets), labeled "BStd mod". This method and these lattice files have been used above and will be used for all other studies in this thesis. $N_e^{\text{macro}} = 10\,000$ particles.

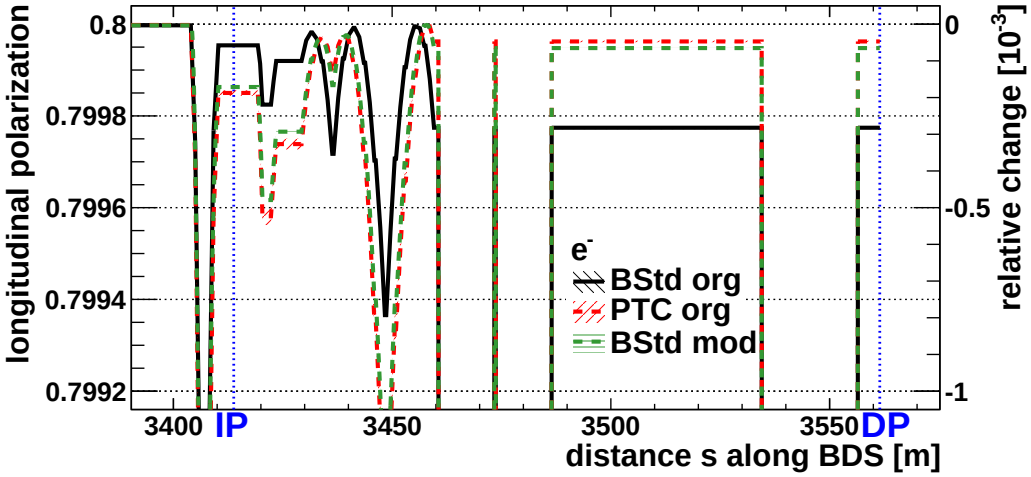

Figure 7.3: Evaluation of different tracking methods and lattice files. Shown is the longitudinal polarization of the e^--beam along the extraction line for three different combinations of lattice files and tracking methods. BStd = Bmad_Standard tracking; PTC = Symp_Lie_PTC tracking; org = original lattice files; mod = modified lattice files.

In contrast to the polarization, the particle transport does not differ significantly for the three samples; therefore, only the polarization is discussed here separately.

In general, the simulation result should not depend on the number of slices a physical beamline element is divided in. If the used tracking method employs approximations, a finer slicing reduces the possible errors from these approximations and is consequently to prefer, if different degrees of slicing yield different results. This is exactly the case in figure 7.3 for the Bmad_Standard spin tracking ("BStd org" vs. "BStd mod") in the quadrupole magnets of the final focus system and the extraction line. Since the beam is rather broad at

these positions, the particles are exposed to stronger magnetic fields than in other quadrupole magnets with similar field gradients, but where the beam sizes are smaller. Apparently, the spin precession in these quadrupole magnet is so strong that the used approximations (calculation of the quaternions up to the first order in the particle coordinates, see section 6.6) are not applicable any more without the additional slicing. This explanation is supported by the sample "PTC org", which uses a completely different tracking method, but obtains very similar results as the sample "BStd mod".

Furthermore, as discussed in section 7.2.2, the extraction line is designed such that the angular divergence θ_r and thus the degree of spin fan-out at the downstream polarimeter are smaller than at the IP. This is the case for θ_r, but not for the sample produced with Bmad_Standard tracking on the original lattice files. The values of the longitudinal polarization $\mathcal{P}_z$, the (entire) polarization $|\vec{\mathcal{P}}|$ and $f(\theta_r)$ at the IP and the polarimeters are listed in table 7.5 including the respective standard deviations for the three samples listed above. At the upstream polarimeter, the scatter is extremely low, since

	sample	$\mathcal{P}_z$	$\lvert\vec{\mathcal{P}}\rvert$	$f(\theta_r)$
UP	BStd org	0.799 999 5 (0)	0.799 999 5 (0)	0.799 999 9 (0)
	PTC org	0.799 999 5 (0)	0.799 999 5 (0)	0.799 999 9 (0)
	BStd mod	0.799 999 5 (0)	0.799 999 5 (0)	0.799 999 9 (0)
IP	BStd org	[0.799 949 5 (5)]	[0.799 949 5 (5)]	0.799 838 (2)
	PTC org	0.799 845 (6)	0.799 846 (6)	0.799 838 (6)
	BStd mod	0.799 863 (2)	0.799 863 (2)	0.799 838 (2)
DP	BStd org	[0.799 774 (3)]	[0.799 774 (3)]	0.799 965 8 (5)
	PTC org	0.799 962 (2)	0.799 962 (2)	0.799 966 (2)
	BStd mod	0.799 947 9 (8)	0.799 947 9 (7)	0.799 965 8 (5)

Table 7.5: Comparison of the different tracking methods and magnet slicings as introduced above. Listed are the longitudinal polarization $\mathcal{P}_z$, the (entire) polarization $|\vec{\mathcal{P}}|$ and the function $f(\theta_r)$ as defined in eq. 7.8 at the IP and the polarimeters (UP/DP = up-/downstream polarimeter) for the electron beam. The uncertainties given by the digit in round brackets are the sample standard deviations. The results put in square brackets have been identified as unreliable (see text).

the simulation starts with an exact value. A maximum precision of 7 digits has been chosen for the tables; the listed standard deviations also refer to this level of precision. The standard deviations of the sample "PTC org" are by a factor ≈ 3 larger than those of the sample "BStd mod", which is explained by the different numbers of macroparticles requiring a factor $\sqrt{10}$

(see section 7.1.3). $f(\theta_r)$ takes (almost) the same value for all samples. For all three samples, the $f(\theta_r)$ is not compatible with the $|\vec{\mathcal{P}}|$ at the IP and the downstream polarimeter with respect to the errors on the mean values[3], but the deviations are safely below the envisaged precision of 0.1 % for the changes in polarization occuring here. But the deviations are clearly larger for "BStd org" than for the two other samples, which supports again the additional slicing.

In conclusion, Bmad_Standard tracking on the original lattice files ("BStd org") yields wrong results and will not regarded any further.

Two-Dimensional T-BMT Precession

In the context of accuracy, eq. 4.15 has to be scrutinized regarding the application to different rotation axes. In general, rotations about different axes do not commute. If the momentum vector undergoes a series of rotations about different axes (x and y) such that it points eventually into the original direction again, this does not have to be the case for the polarization vector undergoing the rotations about the same axes, but by the $(a\gamma + 1)$-fold angles[4]. However, all chicanes in the BDS up to the IP are set up in the horizontal plane and all chicanes between IP and downstream polarimeter in the vertical plane; therefore, the rotations in the respective other plane are limited to possible kicks from correction magnets and the betatron oscillations[5]. The excellent agreement of $f(\theta_r)$ with $|\vec{\mathcal{P}}|$ shows that the problem of the non-commuting rotations is negligible for the betatron oscillations. The agreement of $f(\theta_r)$ with $|\vec{\mathcal{P}}|$ is be re-evaluated for the harsher conditions in chapters 9 and 10.

7.3.4 Dependence on Bunch Parameters

A larger transverse extension of a bunch leads to a larger spin fan-out in inhomogeneous magnetic fields. Therefore, the spin transport for a sample initialized with the design parameters will now be compared with a sample with increased emittances ε_x, ε_y and thus 10 % larger beam sizes and angular divergences. The corresponding beam parameters at the IP have been shown

[3]Note that the digits in round brackets denote the sample standard deviation, not the errors on the mean value, as explained in section 7.1.3.

[4]This is the working principle of the spin rotators in front of the main linac, which are used to rotate the polarization vector in a desired direction.

[5]Betatron oscillations denote the movement of a particle passing alternatingly focussing and defocussing quadrupoles, which let the particle trajectory oscillate around the reference trajectory.

in table 7.3, the polarization values are listed in table 7.6. The change in polarization due to the increased spin fan-out is only $\approx 3{\cdot}10^{-5}$, which is again safely below the envisaged precision of 0.1 % for this study. Consequently, the accuracy of the beam parameters on the percentage level is sufficient for the simulation of the spin transport.

$\varepsilon/\varepsilon_{\text{nom}}$	$\mathcal{P}_z$ @ UP	$\mathcal{P}_z$ @ IP	$\mathcal{P}_z$ @ DP
1	0.799 999 5 (0)	0.799 863 (2)	0.799 947 9 (8)
1.21	0.799 999 4 (0)	0.799 837 (2)	0.799 938 1 (9)

Table 7.6: Comparison of the different beam sizes and angular divergences. Listed are the longitudinal polarization $\mathcal{P}_z$ and the (entire) polarization $|\vec{\mathcal{P}}|$ at the IP and the polarimeters (UP/DP = up-/downstream polarimeter) for the electron beam, once initialized with the design emittances and once with the emittances ε_x and ε_y enhanced by 21 %.

7.4 Impact and Correction of the Incident Angle

As it has been explained in section 7.3.1, a deflection of the beam goes along with a precession of the polarization vector, which strongly affects a measurement of the longitudinal component $\mathcal{P}_z$. Therefore, the lattice is designed such that there is no net bending angle between the polarimeters and the IP (unlike figure 2.1 suggests).

Given that both the polarization vector and the momentum vector of a bunch run parallel to the reference orbit at one certain point, such that $\vartheta_{\text{pol}} = \vartheta_{\text{bunch}} = 0$ and $\mathcal{P}_z = |\vec{\mathcal{P}}|$, the orientation of the polarization vector can be derived from the orientation of the momentum vector from T-BMT precession (see section 4.2.1). If also

- only transverse magnetic fields occur along the following path, such that eq. 4.15 applies,
- the bunch energy $\big(1 + \langle\delta\rangle\big)\, E_0$ remains constant and
- the beam energy spread is negligible ($\sigma_E/E \approx 0$),

then the following equations applies to every point downstream the beamline

without net bending angle:

$$\vartheta_{\text{pol}} = b\,\vartheta_{\text{bunch}} \approx \Big(1 + a\gamma_0\left(1 + \langle\delta\rangle\right)\Big)\,\vartheta_{\text{bunch}} \tag{7.9}$$

$$\phi_{\text{pol}} = \phi_{\text{bunch}}, \tag{7.10}$$

where b denotes the quotient of ϑ_{pol} and ϑ_{bunch}. This quotient is only meaningful, if the azimuthal angles agree. The longitudinal polarization is then given by

$$\mathcal{P}_z = |\vec{\mathcal{P}}| \cdot \cos\left(\vartheta_{\text{pol}}\right) = |\vec{\mathcal{P}}| \cdot \cos\left(b\,\vartheta_{\text{bunch}}\right). \tag{7.11}$$

An incident angle ϑ_{bunch} leads to a relative change (omitting δ)

$$\Delta\mathcal{P}_z/\mathcal{P}_z = 1 - \cos\left(\vartheta_{\text{pol}}\right) = 1 - \cos\big(\left(1 + a\gamma_0\right)\vartheta_{\text{bunch}}\big). \tag{7.12}$$

Table 7.7 lists these changes for different values of the incident angle ϑ_{bunch} that occur in this thesis, calculated for an electron beam with the energy $E_0 = 250\,\text{GeV}$.

$\vartheta_{\text{bunch}}\,[\mu\text{rad}]$	$\vartheta_{\text{pol}}\,[\text{mrad}]$	$\Delta\mathcal{P}_z/\mathcal{P}_z\,[10^{-3}]$
5	2.8	0.004
15	8.5	0.036
30	17	0.15
44	25	0.31
49	28	0.39
50	28	0.40
59	34	0.56
67	38	0.72
100	57	1.6
185	105	5.5
200	114	6.5

Table 7.7: Relative change of $\mathcal{P}_z$ according to eq. 7.12 due to an incident angle ϑ_{bunch} for electrons with $E_0 = 250\,\text{GeV}$ energy.

If the bunch incident angle ϑ_{bunch} is known, it can be employed to compute a corrected longitudinal polarization

$$\begin{aligned}\mathcal{P}_z^{\text{corr}} :=& \frac{\mathcal{P}_z}{\cos\left(\left(1 + a\gamma_0\left(1 + \langle\delta\rangle\right)\right)\vartheta_{\text{bunch}}\right)} \\ \approx& \frac{\mathcal{P}_z}{\cos\left(b\,\vartheta_{\text{bunch}}\right)} \overset{(7.9)}{=} |\vec{\mathcal{P}}|\end{aligned} \tag{7.13}$$

7.4.1 Error Propagation

The error on $\mathcal{P}_z^{\text{corr}}$ as defined in eq. 7.13 is given in the first-order approximation by

$$\begin{aligned}\frac{\Delta\mathcal{P}_z^{\text{corr}}}{\mathcal{P}_z^{\text{corr}}} &= \frac{1}{\mathcal{P}_z^{\text{corr}}}\sqrt{\left(\frac{d\mathcal{P}_z^{\text{corr}}}{d\mathcal{P}_z}\right)^2 \Delta\mathcal{P}_z^2 + \left(\frac{d\mathcal{P}_z^{\text{corr}}}{d\vartheta_{\text{bunch}}}\right)^2 \Delta\vartheta_{\text{bunch}}^2 + \left(\frac{d\mathcal{P}_z^{\text{corr}}}{db}\right)^2 \Delta b^2} \\ &=: \sqrt{C_{|\vec{\mathcal{P}}|}^2 + C_\vartheta^2 + C_b^2} \end{aligned} \tag{7.14}$$

where

$$\begin{aligned} C_{|\vec{\mathcal{P}}|} &= \frac{\Delta\mathcal{P}_z}{\mathcal{P}_z} \\ C_\vartheta &= -b\,\frac{\sin\left(b\,\vartheta_{\text{bunch}}\right)}{\cos^3\left(b\,\vartheta_{\text{bunch}}\right)}\cdot\Delta\vartheta_{\text{bunch}} \approx -b^2\,\vartheta_{\text{bunch}}\cdot\Delta\vartheta_{\text{bunch}} \\ C_b &= -\vartheta_{\text{bunch}}\,\frac{\sin\left(b\,\vartheta_{\text{bunch}}\right)}{\cos^3\left(b\,\vartheta_{\text{bunch}}\right)}\cdot\Delta b \approx -b\,\vartheta_{\text{bunch}}^2\cdot\Delta b \end{aligned} \tag{7.15}$$

Due to the cosine function in eq. 7.13, this first-order is only of limited use for the exact computation of the tolerances, but illustrates the influences of the contributing variables:

- $C_{|\vec{\mathcal{P}}|}$ represents the measurement uncertainty of the polarization, which amounts to 0.25 %, neglecting the statistical error (see section 5.1.3).
- C_ϑ represents the uncertainty to which the incident angle is known. It is proportional to ϑ_{bunch}. Thus the larger the incident angle is, the more accurately it must be known.
- C_b represents the uncertainty of b, where

$$\Delta b = \frac{db}{dE}\,\Delta E = a\gamma\,\frac{\Delta E}{E} \approx b\,\frac{\Delta E}{E}. \tag{7.16}$$

  ΔE contains the uncertainty of the energy measurement as well as the energy spread within the bunch. If $\vartheta_{\text{bunch}} \sim \Delta\vartheta_{\text{bunch}}$ and $\Delta E/E \ll 1$, then $C_b \ll C_\vartheta$.

7.4.2 Alignment Tolerances

To ensure that the longitudinal polarization $\mathcal{P}_z$ at the IP agrees with the longitudinal polarization measured at the polarimeters, the beam needs to have the same orientation at these three places in order to avoid differences

in $\mathcal{P}_z$ due to T-BMT precession. Otherwise, a correction for the incident angle as described above would be necessary, which introduces an additional error increasing with the size of the correction as shown above. An example for such a correction and its non-feasibility will be presented in section 8.2.3.

The tolerance foreseen for the parallel alignment of the beam at the polarimeters to the beam at the IP amounts to $\Delta\vartheta_{\text{bunch}} = 50\,\mu\text{rad}$ (see section 2.4 in [37]). This tolerance results in a the relative uncertainty of $4.0{\cdot}10^{-4}$ on $\mathcal{P}_z$ (table 7.7), which contributes to the envisaged precision of 0.1 % for the spin transport. The particular challenge in this alignment is not so much to determine the beam incident angle relative to the beamline at one point, but to determine the differences in the incident angles at three points which lie up to $\approx 2\,\text{km}$ apart from each other. It remains to be investigated whether the beamlines can be aligned sufficiently precise between the upstream polarimeter and the downstream polarimeter to achieve the required precision of $\Delta\vartheta_{\text{bunch}} = 50\,\mu\text{rad}$. At the IP, the curved beam trajectories in the fields of the detector magnets (see section 8.2) provide an additional burden. Estimates for the achievable precision on $\Delta\vartheta_{\text{bunch}}$ range from $\sim 10\,\mu\text{rad}$ [47] up to $\sim 100\,\mu\text{rad}$ [48]. For a cross-calibration of the polarimeters in absence of collisions, the exact incident angle at the IP is irrelevant. Therefore, this additional burden does not apply in that case.

For the alignment procedure in reality, the beam incident angles $\langle x' \rangle$ and $\langle y' \rangle$ at the laser-bunch IP of the upstream polarimeter constitute the starting point, since these angles are also constrained by beam quality requirements [47]. Thus, the beam orbits at the IP and at the downstream polarimeter need to be adjusted parallel to the orbit at the upstream polarimeter. The polarization vector is adjusted parallel to the beam at the upstream polarimeter; this can be performed with an expected uncertainty $\Delta\vartheta_{\text{pol}} = 25\,\text{mrad}$ [47] yielding a contribution of $3.1 \cdot 10^{-4}$ to the relative error on $\mathcal{P}_z$.

The uncertainties on incident angle ϑ_{bunch} and the polarization angle ϑ_{pol} at the upstream polarimeter are presumed to be uncorrelated here. However, their effects on the longitudinal polarization at the IP are correlated, since ϑ_{bunch} affects ϑ_{pol} by means of T-BMT precession. Therefore, the cumulative contribution to the uncertainty on the propagation of $\mathcal{P}_z$ is calculated from the total uncertainty on ϑ_{pol}, which is given by

$$\Delta\vartheta_{\text{pol}}^{\text{tot}} = \sqrt{\Delta\vartheta_{\text{pol}}^2 + \left((1 + a\gamma_0) \cdot \Delta\vartheta_{\text{bunch}}\right)^2}. \tag{7.17}$$

For $\Delta\vartheta_{\text{bunch}} = 50\,\mu\text{rad}$, $\Delta\vartheta_{\text{pol}} = 25\,\text{mrad}$ and an electron beam with an energy of 250 GeV, the total uncertainty amounts to $\Delta\vartheta_{\text{pol}}^{\text{tot}} = 38\,\text{mrad}$ and contributes a relative error of $7.2 \cdot 10^{-4}$ to the uncertainty on the propagation of $\mathcal{P}_z$ (table 7.7).

7.4.3 Beam-Beam Crossing Angle

The procedure above does not take the crossing angle ζ into account yet. This could in principle be done by

$$\mathcal{P}_z^{\mathrm{corr,D}} = \mathcal{P}_z^{\mathrm{corr}} \cdot \cos\left(\frac{\zeta}{2}\right) = \mathcal{P}_z^{\mathrm{corr}} \cdot \cos\left(7\,\mathrm{mrad}\right). \tag{7.18}$$

Note that the factor $a\gamma + 1$ does not appear in the above equation, since this rotation stems from a transformation of the coordinate systems and not from precession in magnetic fields. For $\cos\left(7\,\mathrm{mrad}\right) \approx 1 - 2.5 \cdot 10^{-5}$, this correction can be safely neglected, as well as the distinction between $\mathcal{P}_z$ and $\mathcal{P}_z^{\mathrm{D}}$, as long as $|\mathcal{P}_x| < 0.01$ (eq. 3.11). The longitudinal polarization $\mathcal{P}_z^{\mathrm{D}}$ at the IP in the detector coordinate system will be listed in the following tables nevertheless for the sake of completeness.

7.4.4 Correction Applied on the Basic Lattice

As example, table 7.8 lists all relevant parameters for the correction at the polarimeters and the IP and the polarimeters for the basic lattice, where a correction should be unnecessary by design. The largest angle $\vartheta_{\mathrm{bunch}} = 0.4\,\mu\mathrm{rad}$ appears at the IP, but the resulting correction for such a small angle is only of the order of 10^{-8}. Since $\vartheta_{\mathrm{bunch}}$ and ϑ_{pol} are almost zero, the uncertainties on ϕ_{bunch} and ϕ_{pol} are extremely large, as well as b, which is in all cases compatible with the expected value of $a\gamma + 1 \approx 568$.

	UP	IP	DP
$\mathcal{P}_x$	$-0.000\,006\,(9)$	$-0.000\,0\,(1)$	$0.000\,19\,(9)$
$\mathcal{P}_y$	$-0.000\,000\,(2)$	$-0.000\,00\,(7)$	$0.000\,000\,(7)$
$\mathcal{P}_z$	$0.799\,999\,5\,(0)$	$0.799\,863\,(2)$	$0.799\,947\,9\,(8)$
$\mathcal{P}_z^{\mathrm{D}}$		$0.799\,844\,(2)$	
$\lvert\vec{\mathcal{P}}\rvert$	$0.799\,999\,5\,(0)$	$0.799\,863\,(2)$	$0.799\,947\,9\,(7)$
$\vartheta_{\mathrm{bunch}}\,[\mu\mathrm{rad}]$	0.009 ± 0.007	0.4 ± 0.3	0.2 ± 0.1
$\vartheta_{\mathrm{pol}}\,[\mathrm{mrad}]$	0.011 ± 0.008	0.17 ± 0.10	0.2 ± 0.1
$\phi_{\mathrm{bunch}}\,[^\circ]$	176 ± 89	179 ± 59	-1 ± 52
$\phi_{\mathrm{pol}}\,[^\circ]$	-178 ± 79	178 ± 97	-0 ± 25
b	$3\,532 \pm 17\,397$	573 ± 860	$1\,678 \pm 5\,755$
$\mathcal{P}_z^{\mathrm{corr}}$	$0.799\,999\,5\,(0)$	$0.799\,863\,(2)$	$0.799\,947\,9\,(8)$

Table 7.8: Polarization of the electron beam at the IP and the laser-bunch IPs of the polarimeters. Listed are the polarization-relevant parameters as introduced in section 3.2.5.

Chapter 8

Interaction Region

In this chapter, beamline elements which are not yet included in the basic lattice, namely the crab cavities and the detector magnets, are inserted and their effects in absence of collisions are studied, which is relevant for the calibration of the polarimeters during the tune-up of the accelerator (see chapter 11). All these changes occur behind of the upstream polarimeter, thus they affect only the polarization at the IP and the downstream polarimeter.

8.1 Bunch Rotation

The ILC design foresees a beam crossing angle $\zeta = 14\,\text{mrad}$ in the x-z plane at the IP. To avoid a loss of luminosity, the bunches are rotated by so-called "crab cavities"[1] located $\Delta s = 13.5\,\text{m}$ in front of the IP, such that the bunches collide head-on as sketched in figure 8.1. For that purpose, the particles have to be shifted horizontally[2] - depending on their longitudinal position z in the bunch - by

$$\Delta x(z) = \tan(\zeta/2) \cdot z \tag{8.1}$$

upon the arrival at the IP.

In this section, the implementation of the crab cavities is explicated and their effects on the particle transport and the polarization in absence of collisions are investigated. The effects of the bunch rotation on colliding beams will be shown in chapter 9.

[1] The name is derived from the sideward motion of crabs.

[2] Unlike in an actual rotation, the longitudinal component of the bunch is left unchanged. However, the increase in the length of the bunch is completely negligible.

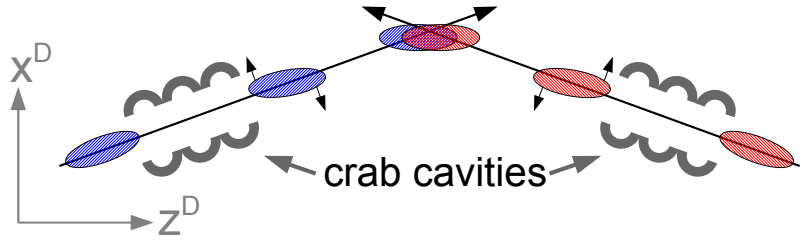

Figure 8.1: Schematic view of bunch rotation by means of crab cavities. The cavities are illustrated as 3-cell structures. The crossing angle in this drawing is exaggerated.

Implementation

The crab cavities apply a z-dependent horizontal kick $\Delta\hat{p}_x(z)$ on the bunch particles whose strength can be naïvely estimated:

$$\Delta\hat{p}_x(z) = \frac{\Delta x(z)}{\Delta s} = \frac{\tan(\zeta/2)\cdot z}{\Delta s} = 5.2\cdot 10^{-4}\cdot\frac{z}{\mathrm{m}} \tag{8.2}$$

Accounting also for the magnets between crab cavities and IP, the achieved distance at the IP is

$$\Delta x(z) = 0.021\,\mathrm{m}\cdot\Delta\hat{p}_x\cdot\sqrt{\frac{\beta_x(\mathrm{IP})}{\beta_x(\mathrm{CC})}}, \tag{8.3}$$

where β_x is the horizontal beta function of the lattice, which take the values $\beta_x(\mathrm{IP}) = 21\,\mathrm{mm}$ at the IP and $\beta_x(\mathrm{CC}) = 12.7\,\mathrm{km}$ at the center of the crab cavity section [49]. Applying the correct signs, the required kicks are

$$\Delta\hat{p}_x(z) = \pm\frac{\tan(\zeta/2)\cdot z}{0.021\,\mathrm{m}}\cdot\sqrt{\frac{\beta_x(\mathrm{IP})}{\beta_x(\mathrm{CC})}} = \pm 4.279\cdot 10^{-4}\cdot\frac{z}{\mathrm{m}} \tag{8.4}$$

for the $\mathrm{e}^{\pm}$-beams.

The kick $\Delta\hat{p}_x(z)$ is performed by the magnetic component of a time- (i. e. z-) dependent electromagnetic field. The electric component of the field is negligible for this cavity operation mode. Therefore, the crab cavities are implemented in this simulation simply like a dipole corrector magnet with a z-dependent kick strength including the corresponding spin rotation.

8.1.1 Particle Transport

In the following, the bunch parameters for a sample without bunch rotation ("BStd mod" as in section 7.3.3, $N_e = 10\,000$ macroparticles per bunch,

$N_{\mathrm{rep}} = 1000$ bunches) are confronted with the parameters of a sample with bunch rotation. The latter one contains $N_e = 100\,000$ macroparticles per bunch and $N_{\mathrm{rep}} = 10\,000$ bunches.

Corresponding to figure 8.1, figure 8.2 shows the projection of the particles of all electron bunches at the IP on the x-z plane, i. e. in a bird's eye view, without and with bunch rotation, respectively. The solid line indicates the desired rotation angles of 0 and -7 mrad, respectively. In both figures, the horizontal bunch width σ_x with respect to the beamline coordinate system is marked (see chapter 3 for the different coordinate systems).

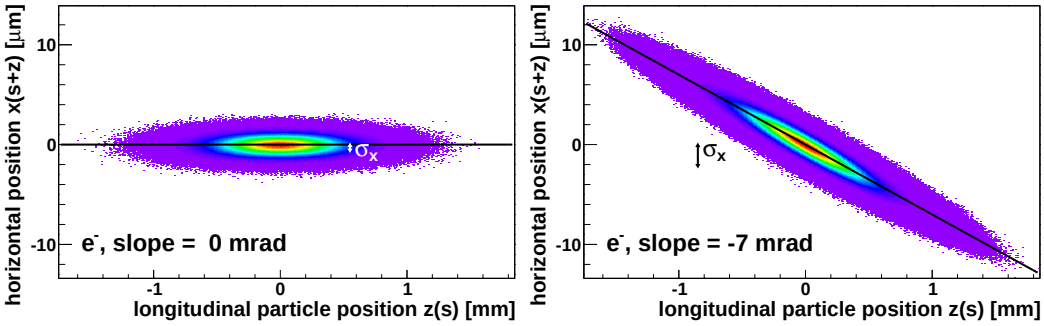

(a) (b)

Figure 8.2: Electron bunch at the IP projected on the horizontal plane (in the beamline coordinate system) without (a) and with (b) bunch rotation. Shown is the density of particles accumulated for all bunches. For the correctness of the illustration, x is replaced here by $x(s_{\mathrm{IP}} + z) = x(s_{\mathrm{IP}}) + x'(s_{\mathrm{IP}}) \cdot z(s_{\mathrm{IP}})$ (cf. section 3.1). The black line is indicates the desired rotation angle denoted in each figure. In both pictures, the size of σ_x (not σ_x^{D}) is indicated.

Table 8.1 lists the horizontal bunch parameters at the IP (for both coordinate systems) and at the downstream polarimeter for the samples without and with bunch rotation. The spreads of the latter one are a factor $\sqrt{10}$ smaller due to the 10-fold number of macroparticles. The mean position $\langle x \rangle$, $\langle x^{\mathrm{D}} \rangle$ and the incident angle $\langle x' \rangle$ are not affected by the bunch rotation, nor the angular divergence θ_x. At the IP, the bunch rotation yields the desired bunch size σ_x^{D} in the detector coordinate system. At the downstream polarimeter, the bunch rotation leads to a slight increase in σ_x, which is however negligible with respect to the required laser spot size (cf. section 7.2.2). To obtain a measure for the bunch rotation, the rotation angle $\vartheta_{\mathrm{crab}}$ of a bunch with N particles is calculated by

$$\tan \vartheta_{\mathrm{crab}} = \left(\sum_{i=1}^{N} (X_i + x_i' \cdot Z_i) \cdot \mathrm{sign}\,(Z_i) \right) / \left(\sum_{i=1}^{N} |Z_i| \right) \qquad (8.5)$$

where $X_i := x_i - \langle x \rangle$ and $Z_i := z_i - \langle z \rangle$ are the horizontal and longitudinal coordinates of the i-th particle with respect to the bunch center. The rotation angles for both beams correspond to the design values of $\mp 7\,\mathrm{mrad}$ for the $e^{\pm}$ beam.

position	parameter		bunch rotation without	with
IP	$\langle x \rangle$	[nm]	-22 ± 6	-22 ± 7
	$\langle x^{\mathrm{D}} \rangle$	[nm]	-22 ± 22	-22 ± 2
	$\langle x' \rangle$	[μrad]	-0.3 ± 0.3	-0.3 ± 0.1
	σ_x	[nm]	640 ± 4	$2\,196 \pm 5$
	σ_x^{D}	[nm]	$2\,195 \pm 15$	640 ± 1
	$\vartheta_{\mathrm{crab}}$	[mrad]	-0.00 ± 0.03	-7.001 ± 0.008
	$\vartheta_{\mathrm{crab}}$ (e^+)	[mrad]	0.00 ± 0.03	7.001 ± 0.008
	θ_x	[μrad]	32.3 ± 0.2	32.35 ± 0.07
DP	$\langle x \rangle$	[μm]	3.3 ± 0.1	3.29 ± 0.03
	$\langle x' \rangle$	[μrad]	0.2 ± 0.2	0.20 ± 0.05
	σ_x	[μm]	9.7 ± 0.2	10.58 ± 0.05
	θ_x	[μrad]	16.2 ± 0.1	16.18 ± 0.04

Table 8.1: Selected horizontal bunch parameters of the electron beam at the IP and the downstream polarimeter (DP) without and with bunch rotation. The rotation angle $\vartheta_{\mathrm{crab}}$ is also listed for the positron beam.

8.1.2 Spin Transport

A kick depending on the longitudinal position z also implies a correlation of the longitudinal polarization $\mathcal{P}_z$ with z, i. e. a spin fan-out along the z-axis. For a perfectly longitudinally polarized bunch, the longitudinal polarization $\mathcal{P}_z$ would therefore decrease. Figure 8.3 shows the longitudinal polarization along the beam delivery system both with the crab cavities turned off and on. The differences in the longitudinal polarizations of the bunches as a whole is $< 10^{-5}$ and therefore negligible[3].

Even though the longitudinal polarization of the whole bunch is not affected, a variation could affect the polarization measurement, if the laser of the polarimeter does not hit the bunch centrally. Figure 8.4 shows the longitudinal polarization of the macroparticles versus the z position in the bunch at the IP and at the downstream polarimeter. The spreads in $\mathcal{P}_z$ are

[3]The exact numbers can be found in table 7.8 for the sample without bunch rotation and in table 8.6 (column "no magnets") for the sample with bunch rotation.

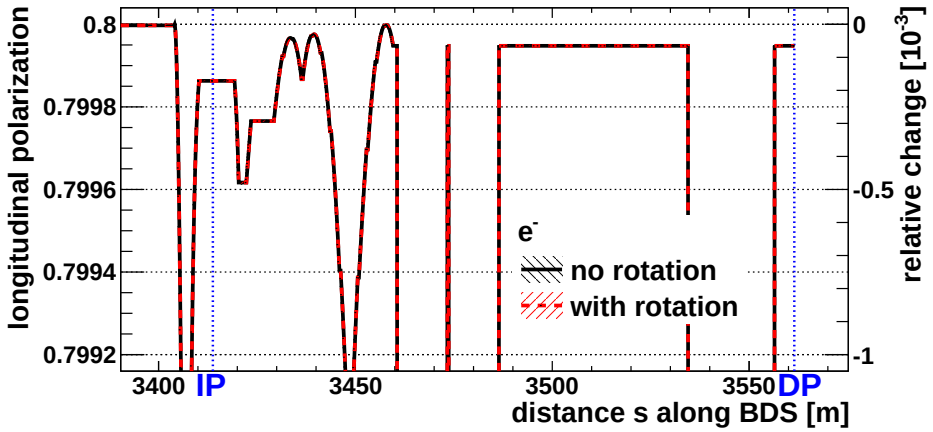

Figure 8.3: Longitudinal polarization $\mathcal{P}_z$ of the electron beam along the BDS without (black, solid) and with (red, dashed) bunch rotation. The crab cavities are located at $s = 3400\,\mathrm{m}$.

negligible with respect to the envisaged precision of 0.1 % at both positions; there is no correlation between $\mathcal{P}_z$ and z on this scale. In conclusion, the rotation of the bunch does not affect the longitudinal polarization in absence of collisions.

8.2 Detector Magnets

In this section, the magnets of the particle detectors around the e^+e^- IP are added to the simulation. The magnets comprise the detector solenoid (section 8.2.1) and the anti-DID (detector-integrated dipole, section 8.2.2).

8.2.1 Implementation of the Detector Solenoid

The solenoid provides a field parallel to the detector axis for the tracking detectors in order to measure the charge and the momentum of charged particles produced in the e^+e^- collision. As the current two detector concepts ILD and SiD [8] do not differ fundamentally (mainly by the magnet dimensions and field strengths, but only slightly in the integrated field strength $\int B(l)\,dl$ which is the more relevant quantity here), only the SiD concept is implemented in this thesis.

Due to the beam crossing angle $\zeta = 14\,\mathrm{mrad}$, the beams enter the solenoid off-axis as sketched in figure 8.5. The motion through the fringe fields at

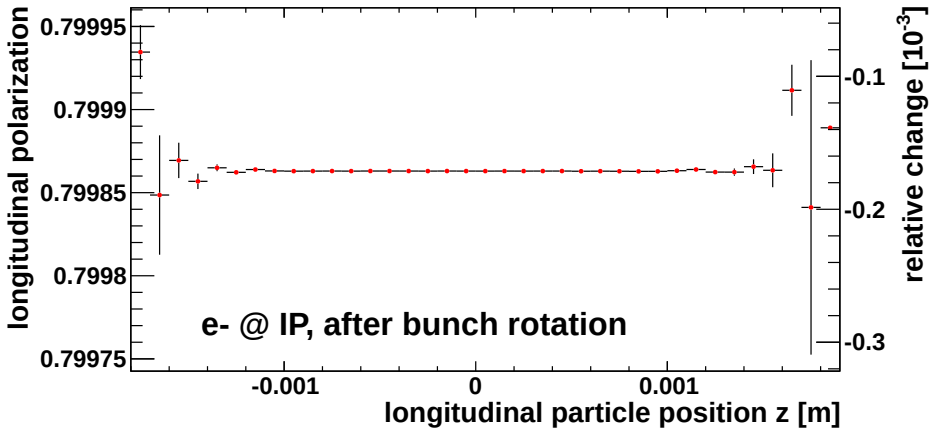

(a)

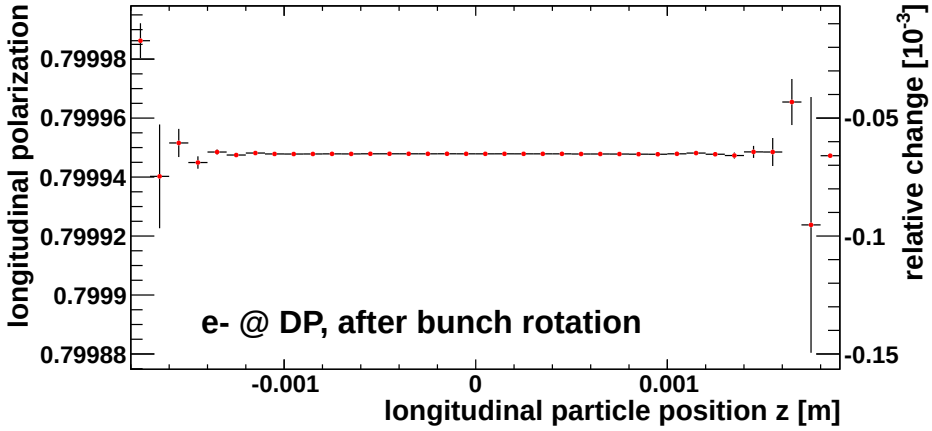

(b)

Figure 8.4: Longitudinal polarization along the bunch at the IP (a) and the downstream polarimeter (b) for the electron beam after bunch rotation. 10 000 bunches with 100 000 particles each are added up in this plot.

the ends of the solenoid is described by the so-called "hard-edge model"[4] (sketched in figure 8.5b), which imposes a fringe field kick $\vartheta_{\text{fringe}}$ at both the entrance and the exit of a solenoid and assumes a homogeneous field B_{sol} in between. The kick angle is given by

$$|\vartheta_{\text{fringe}}| = \frac{\zeta B_{\text{sol}} L_{\text{sol}}}{8\,|B\rho|}, \tag{8.6}$$

where B_{sol} denotes the nominal solenoid field strength, L_{sol} the solenoid length and $B\rho$ the magnetic rigidity of the beam (see section 6.1.2).

[4] see [50] and [51] for a more extensive description

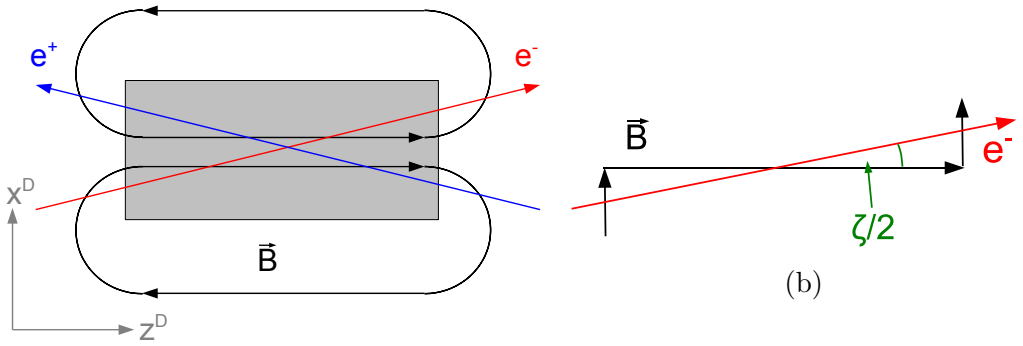

(a) (b)

Figure 8.5: Sketch of the detector solenoid field. The orientation of the detector (solenoid) and the beams is shown in (a). The solenoid field according to the "hard-edge model" is shown in (b), where also the crossing angle ζ is indicated (the full crossing angle is the angle between the two beams). The drawn coordinate axes apply to both sketches. On the basis of fig. 1 from [50].

The Bmad_Standard spin tracking method [22] accounts only for the magnetic field component $\vec{B}_{\parallel}$ parallel to the particle trajectory and has therefore been modified for this study in the following way: the spin precession due to the fringe field kicks and the perpendicular component $\vec{B}_{\perp}$ of the field within the solenoid is computed and applied at both the entrance and the exit (one half of the precession within the solenoid at each). Since large rotations about different axes do not commute, the detector solenoid is not implemented as a whole in the lattice, but as a series of 0.1 m long slices[5] with a total length of $L_{\mathrm{sol}} = 5.586\,\mathrm{m}$ and a magnetic field strength of $B_{\mathrm{sol}} = 5\,\mathrm{T}$. Thus the kicks are applied at each entrance and each exit in both particle and spin transport. But since the exit kick of one slice is exactly canceled by the entrance kick of the following slice, slicing does not make a difference if all slices come with the same magnetic field strength like in this study. However, while the particle positions x, y are returned correctly by the program, the angles x', y' do not correspond to $dx/ds, dy/ds$ between two slices, but need to be corrected for the fringe field kick. Since the fringe field kick is proportional to the transverse distance of the solenoid axis, it is practically zero at the IP; therefore the correction is neglected here.

[5] The two outermost slices are 0.093 m long.

8.2.2 Implementation of the Anti-DID

As an unwelcome side effect of the collision, $\sim 10^5$ electron-positron pairs per bunch crossing are produced by beamstrahlung photons (see figure 4.3). The majority of these electrons carries only an energy of a few GeV per particle, such that they are confined by the solenoid field and hit the forward region of the detector where they provide a powerful source of background by their sheer number [32]. The anti-DID (detector-integrated dipole) serves to guide these electrons into the beampipe in order to reduce the background in the detector. The superimposed dipole field deforms the solenoid field lines in the forward regions such that they run parallel to the outgoing beams (sketched in figure 8.6) and guide the pair electrons into the outgoing beam pipe[6].

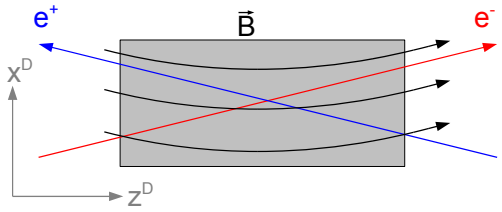

Figure 8.6: Sketch of the magnetic field of solenoid and anti-DID in the detectors, analogously to figure 8.5a.

The strength of the anti-DID field [52] for the SiD concept is described by the following 6-th order polynomial with the coefficients a_i listed in table 8.2:

$$B_{\text{anti-DID}}(z) = -0.19\,\text{T} \cdot \text{sign}(z) \cdot \sum_{i=0}^{6} a_i \left(\frac{|z|}{\text{m}}\right)^i \tag{8.7}$$

The anti-DID field is implemented as a series of 5 cm long kicker magnets (see section 6.1.1) with strengths calculated according to eq. 8.7 for an interval with a length of 11 m centered at the IP.

As explained in section 8.2.1, the angles within a sliced solenoid need to be corrected for the fringe field kick. But since the fringe field kicks of the solenoid are predominantly vertical as well, the corresponding rotations commute and thus the correction can be omitted here.

[6]The originally foreseen purpose of a detector-integrated dipole was the compensation of the solenoid effects on the incoming beams by making the magnetic field lines parallel to the incoming beams. Since the the new purpose of the dipole required the opposite dipole field orientation, its name got the prefix “anti”.

coefficient	value
a_0	0.001 534 3
a_1	0.184 76
a_2	0.050 422
a_3	−0.092 768
a_4	0.030 064
a_5	−0.003 941 3
a_6	0.000 188 6

Table 8.2: Coefficients to eq. 8.7 [52].

8.2.3 Results

To investigate the effects of the detector magnets, three different samples are used. All samples feature bunch rotation by the crab cavities; emission of synchrotron radiation is not simulated.

sample name	description
no magnets	The sample with bunch rotation as in the section 8.1. All beam parameters as in table 7.1, $N_e^{\text{macro}} = 100\,000$, $N_{\text{rep}} = 10\,000$, both detector magnets off.
solenoid	In contrast to the sample "no magnets", the detector solenoid is switched on and $N_e^{\text{macro}} = 10\,000$, $N_{\text{rep}} = 1000$. The anti-DID is still switched off.
all magnets	In contrast to the sample "solenoid", the anti-DID is switched on.

Table 8.3: Simulated samples for the investigation of the effects of the detector magnets.

Particle Transport

The effects of a solenoid on the particle transport are described in [50] and [51]. According to the Lorentz equation, the particle motion in a magnetic field is only affected by the perpendicular field $\vec{B}_\perp$, which is described here by the hard-edge model introduced in section 8.2.1. In the presence of a crossing angle in the horizontal plane, this model leads to a vertical fringe-field kick at both ends of the solenoid, as sketched in figure 8.7. Inside the solenoid, the particles experience a magnetic field with a perpendicular component pointing into the opposite direction, such that the vertical displacement disappears at the IP and the beam arrives under the negative fringe field kick

angle. At the end of the solenoid, the beam departs at $\langle y \rangle = -\vartheta_{\text{fringe}} L_{\text{sol}}$, where L_{sol} denotes the solenoid length, under the angle $\langle y' \rangle = -2\,\vartheta_{\text{fringe}}$ [50].

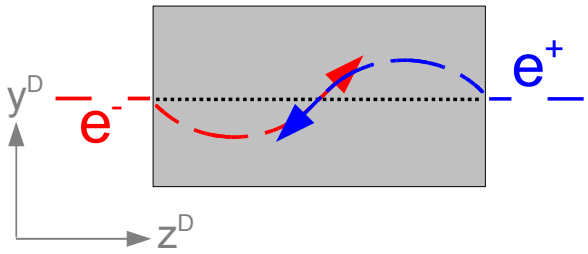

Figure 8.7: Sketch of the vertical motion in the detector solenoid under the horizontal crossing angle. The kink at the solenoid entrances is caused by the fringe field kick $\vartheta_{\text{fringe}}$. On the basis of fig. 1 from [50].

The solenoid field also induces a rotation of the bunch about its longitudinal axis. The expected tilt angle at the IP (in the center of the solenoid) is [51]:

$$|\alpha_{\text{sol}}| = \frac{B_{\text{sol}}\, L_{\text{sol}}}{4\,|B\rho|} \tag{8.8}$$

For flat bunches ($\sigma_x \gg \sigma_y$), the tilt hardly affects the horizontal beam size σ_x, whereas the vertical beam size σ_y increases to [51]

$$\sigma_y \approx \sigma_{y0} \sqrt{1 + \left(\frac{\sigma_{x0}}{\sigma_{y0}}\,\alpha_{\text{sol}}\right)^2}, \tag{8.9}$$

where σ_{x0} and σ_{y0} are the beam sizes at the IP without the solenoid field.

In the following, first the effects of the solenoid on the bunch parameters at the IP will be discussed on the basis of tables 8.4 and 8.5 and figure 8.8, afterwards the additional effects of the anti-DID, and thereafter the implications for the further transport to the downstream polarimeter.

Table 8.4 lists the values for the fringe field kick $\vartheta_{\text{fringe}}$, the tilt angle α_{sol} and the enlarged beam size σ_y calculated for the two detector concepts SiD and ILD assuming a 250 GeV electron beam ($B\rho = 833.9\,\text{Tm}$). σ_y is calculated for $\sigma_{x0} = 2.2\,\mu\text{m}$ and $\sigma_{y0} = 5.8\,\text{nm}$.

Table 8.5 lists selected electron bunch parameters from the simulation at the IP for the three samples listed in table 8.3. Due to the different number of macroparticles, the spreads are a factor $\sqrt{10}$ smaller for the sample "no magnets".

Figure 8.8 shows the simulated vertical bunch position along the BDS between IP and downstream polarimeter and in detail around the IP for the

detector	B_{sol} [T]	L_{sol} [m]	$B_{\mathrm{sol}} \cdot L_{\mathrm{sol}}$ [Tm]	$\lvert\vartheta_{\mathrm{fringe}}\rvert$ [μrad]	$\lvert\alpha_{\mathrm{sol}}\rvert$ [mrad]	σ_y [nm]
SiD	5	5.586	28.0	58.6	8.37	19.3
ILD	3.5	7.35	25.8	54.0	7.71	17.9

Table 8.4: Expected bunch parameters calculated from eqs. 8.6, 8.8 and 8.9 for the two detector concepts and $B\rho = 833.9\,\mathrm{Tm}$, $\sigma_{x0} = 2.2\,\mu\mathrm{m}$ and $\sigma_{y_0} = 5.8\,\mathrm{nm}$.

		no magnets	solenoid	all magnets
$\langle x \rangle$	[nm]	-22 ± 7	435 ± 22	$-1\,311 \pm 22$
$\langle x^{\mathrm{D}} \rangle$	[nm]	-22 ± 2	434 ± 6	$-1\,188 \pm 6$
$\langle y \rangle$	[nm]	-0.00 ± 0.02	3.6 ± 0.2	$25\,883 \pm 3$
σ_x	[nm]	$2\,196 \pm 5$	$2\,195 \pm 16$	$2\,196 \pm 16$
σ_x^{D}	[nm]	640 ± 1	639 ± 4	640 ± 5
σ_y	[nm]	5.75 ± 0.01	19.3 ± 0.1	319 ± 2
$\langle x' \rangle$	[μrad]	-0.3 ± 0.1	-0.3 ± 0.3	-1.1 ± 0.3
$\langle y' \rangle$	[μrad]	0.00 ± 0.05	58.6 ± 0.1	185.1 ± 0.1
θ_x	[μrad]	32.35 ± 0.07	32.4 ± 0.2	32.3 ± 0.2
θ_y	[μrad]	14.36 ± 0.03	14.4 ± 0.1	14.4 ± 0.1

Table 8.5: Selected beam parameters of the electron beam at the IP for the three samples listed in table 8.3.

different magnet configurations. At $s = 3411\,\mathrm{m}$ and $s = 3416.6\,\mathrm{m}$, the fringe-field kicks as described above appear. If only the solenoid is switched on, the beam follows the course described by the hard-edge model. The vertical incident angle $\langle y' \rangle$ at the IP (table 8.5) corresponds to the fringe field kick $|\vartheta_{\mathrm{fringe}}|$ (table 8.4) as expected.

The change in the horizontal bunch position $\langle x \rangle, \langle x^{\mathrm{D}} \rangle$ results from the vertical motion of the bunch within the solenoid field caused by the horizontal crossing angle ζ. Since $\vartheta_{\mathrm{fringe}} \ll \zeta$, it can be seen as "second-order effect". Compared to the maximum vertical displacement within the solenoid in front of the IP

$$|\langle y \rangle_{\mathrm{max}}| \approx 0.25\ |\vartheta_{\mathrm{fringe}}|\ L_{\mathrm{sol}} = 40.9\,\mu\mathrm{m}, \tag{8.10}$$

the horizontal displacement at the IP of $\langle x^{\mathrm{D}} \rangle = 434\,\mathrm{nm}$ is small. The change in the vertical bunch position $\langle y \rangle$ at the IP is small compared to $|\langle y \rangle_{\mathrm{max}}|$, but both $\langle x^{\mathrm{D}} \rangle$ and $\langle y \rangle$ are larger than foreseen with respect to the beam-beam collisions at the IP (see chapter 10). The angular divergences θ_x and θ_y, the horizontal bunch sizes σ_x and σ_x^{D} and the horizontal incident angle $\langle x' \rangle$

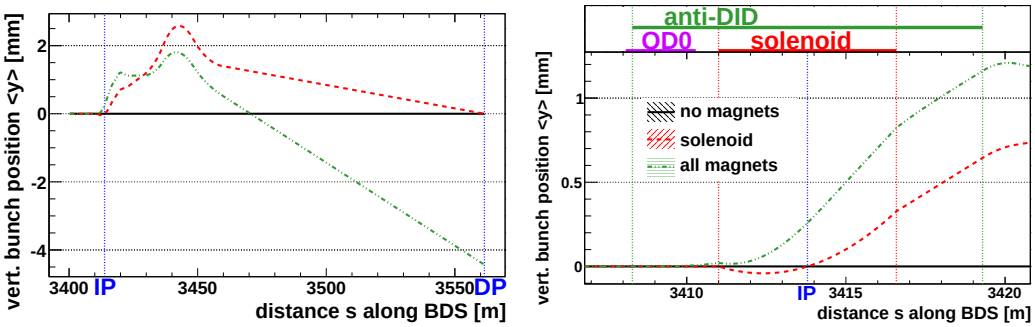

(a) (b)

Figure 8.8: Vertical bunch position $\langle y \rangle$ along the BDS between IP and downstream polarimeter (a) and in detail around the IP (b) for the three samples listed in table 8.3. The positions of the detector magnets and the final focus quadrupole QD0 are indicated in the upper part of (b).

remain unchanged by the solenoid field, whereas the vertical bunch size σ_y increases as expected due to the rotation of the bunches by α_{sol}.

In the operation of an accelerator, it is desirable to keep the horizontal and the vertical motion of the particles decoupled. The bunch rotation in the solenoid field induces precisely such "skew coupling". Possible countermeasures, which have not been taken in this thesis, are skew quadrupoles (quadrupoles tilted by 45°) or anti-solenoids (solenoids with a field pointing in the opposite direction), which are described in more detail in [50, 51].

For the ILD concept, the values of $\vartheta_{\text{fringe}}$, α_{sol} and σ_y differ only slightly from those for the SiD concept. Thus, the particle transport is affected qualitatively likewise by the ILD solenoid.

The anti-DID simply adds a dipole field, which bends the beams about the x-axis. This leads primarily to a displacement $\langle y \rangle$ at the IP (table 8.5) and an even larger incident angle $\langle y' \rangle$ than for the sample "solenoid". Due to the skew coupling (see above), $\langle x \rangle$ and $\langle x' \rangle$ are also affected, but to a smaller extent. Like for the sample "solenoid", θ_x, θ_y, σ_x and σ_x^{D} remain unchanged, whereas the vertical bunch size σ_y increases much further. Figure 8.9 shows the vertical particle position y versus the particle energy E. The correlation of y and E shows that the dispersion generated by the anti-DID in conjunction with the beam energy spread cause the drastic increase of the vertical beam size. The incident angle and the beam position can be corrected by additional dipole magnets outside the detector. A correction of the displacement of the beam removes also the dispersion.

As shown above, the detector magnets have a large impact on several bunch parameters at the IP, which has to be compensated in order to achieve

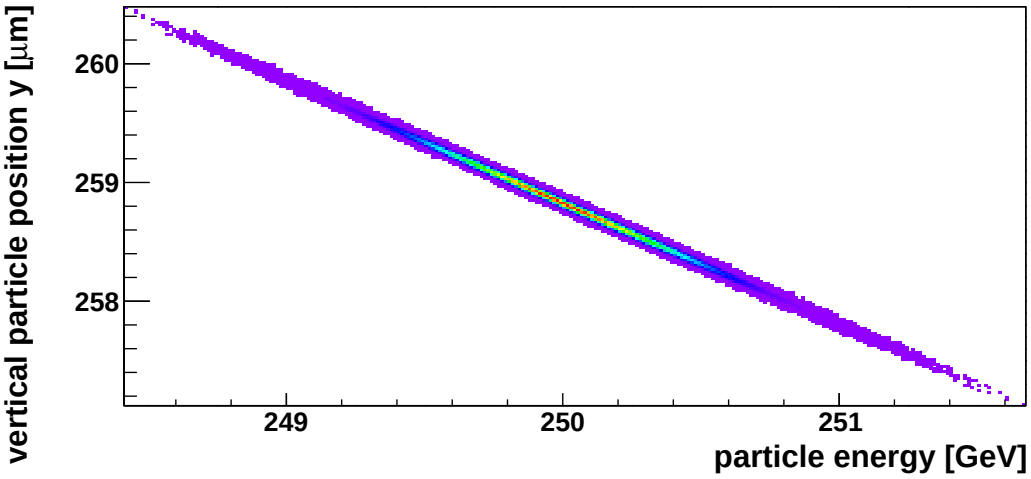

Figure 8.9: Vertical dispersion at the IP for the sample all magnets.

the desired luminosity in the e^+e^- collisions. The compensation will also affect the bunch parameters at the downstream polarimeter, which makes a detailed discussion of these parameters in view of the laser-bunch interaction pointless without the compensation magnets being implemented.

Nevertheless, the effects of the detector magnets and the compensation magnets on the polarization can already be discussed qualitatively without the compensation magnets being implemented, since the relevant bunch parameters are left unchanged (the angular divergences θ_x and θ_y) or their influence is well-understood and correctable (the incident angles $\langle x' \rangle$ and $\langle y' \rangle$), whereas the bunch positions and sizes do not directly affect the polarization.

Spin Transport

Table 8.6 lists the polarization and the related bunch parameters at the IP and the downstream polarimeter for the electron beam. Figure 8.10 shows the longitudinal and the entire polarization of the electron bunches between IP and downstream polarimeter.

For the sample "no magnets", the spin transport has been discussed in section 7.3. Since the polar angles ϑ_{pol} and $\vartheta_{\mathrm{bunch}}$ are almost zero, their quotient b is not meaningful for this sample.

When the detector magnets are added to the simulation, their fields lead to additional T-BMT precession, which leave the (entire) polarization and $f(\theta_r)$ (cf. section 7.3.2) practically unchanged (see also figure 8.10a). The longitudinal component $\mathcal{P}_z$ is strongly affected by the T-BMT precession, as figure 8.10b illustrates, which leads to a decrease with respect to the

position			no magnets	solenoid	all magnets
IP	$\mathcal{P}_z$		0.799 863 0 (5)	0.799 424 (3)	0.795 452 (7)
	$\lvert\vec{\mathcal{P}}\rvert$		0.799 863 0 (5)	0.799 863 (2)	0.799 858 (2)
	$f(\theta_r)$		0.799 838 1 (6)	0.799 838 (2)	0.799 838 (2)
	ϑ_{bunch}	[μrad]	0.3 ± 0.1	58.6 ± 0.1	185.1 ± 0.1
	ϑ_{pol}	[mrad]	0.07 ± 0.04	33.13 ± 0.08	105.01 ± 0.08
	ϕ_{bunch}	[°]	180 ± 9	90.3 ± 0.3	90.33 ± 0.10
	ϕ_{pol}	[°]	179 ± 65	90.6 ± 0.3	90.87 ± 0.09
	b		189 ± 145	565.33 ± 0.06	567.45 ± 0.02
	$\mathcal{P}_z^{\text{corr}}$		0.799 863 0 (5)	0.799 868 (2)	0.799 872 (2)
DP	$\mathcal{P}_z$		0.799 947 9 (2)	0.799 923 7 (7)	0.799 635 5 (7)
	$\lvert\vec{\mathcal{P}}\rvert$		0.799 947 9 (3)	0.799 947 8 (7)	0.799 951 1 (7)
	$f(\theta_r)$		0.799 965 8 (2)	0.799 965 8 (5)	0.799 965 8 (5)
	ϑ_{bunch}	[μrad]	0.20 ± 0.05	13.77 ± 0.02	48.78 ± 0.02
	ϑ_{pol}	[mrad]	0.24 ± 0.04	7.762 ± 0.010	28.090 ± 0.009
	ϕ_{bunch}	[°]	-0 ± 2	-87.3 ± 0.7	-88.1 ± 0.2
	ϕ_{pol}	[°]	-0.0 ± 0.7	-94.7 ± 0.8	-93.5 ± 0.2
	b		$1\,225 \pm 178$	563.8 ± 0.6	575.87 ± 0.09
	$\mathcal{P}_z^{\text{corr}}$		0.799 947 9 (2)	0.799 948 2 (7)	0.799 942 9 (7)

Table 8.6: Polarization of the electron beam at the IP and the downstream polarimeter (DP) for the three samples listed in table 8.3.

sample "no magnets" by 0.05 % (sample "solenoid") and 0.6 % (sample "all magnets") at the IP, but practically not (sample "solenoid") and only by 0.04 % (sample "all magnets") at the downstream polarimeter.

In presence of a magnetic field component parallel to the beam, eqs. 7.9 and 7.10 do not apply any longer in general, since there is no counterpart for the longitudinal T-BMT precession (eqs. 4.12-4.14). But the effect of the is longitudinal T-BMT precession is tiny, since the polarization vector is almost parallel to the precession axis. To obtain an estimate value for the effect of the longitudinal T-BMT precession, the relative deviation of $\mathcal{P}_z^{\text{corr}}$ from $|\vec{\mathcal{P}}|$ at the downstream polarimeter for the sample "all magnets" is taken, which accounts for the effect of the entire solenoid and a rather large transverse polarization component inside the solenoid. This approach excludes the effect of the incident angle, which has already been considered in section 7.4. The result is a deviation of $\approx 10^{-5}$, which is negligible compared to the precision goal of 0.1 % (section 5.2). If the orbit is corrected for the effects of the detector magnets, such that the polar angles ϑ_{bunch} and ϑ_{pol} are

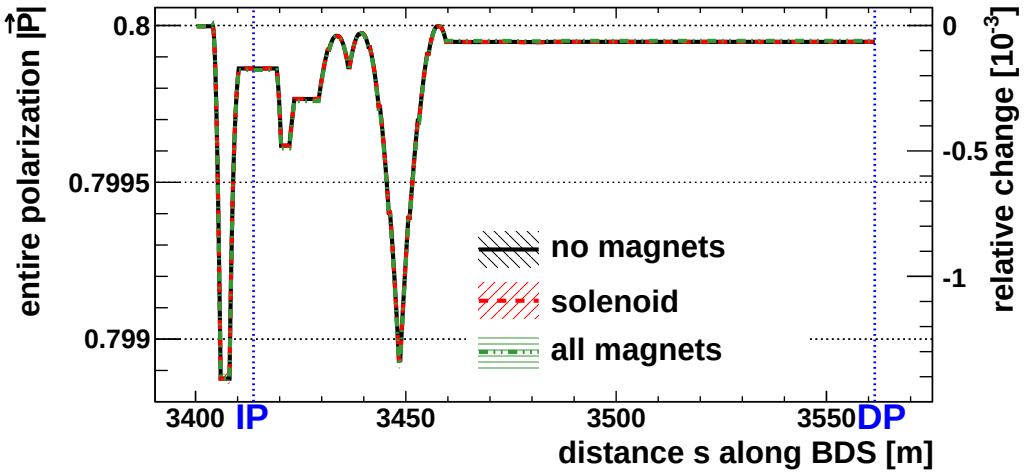

(a)

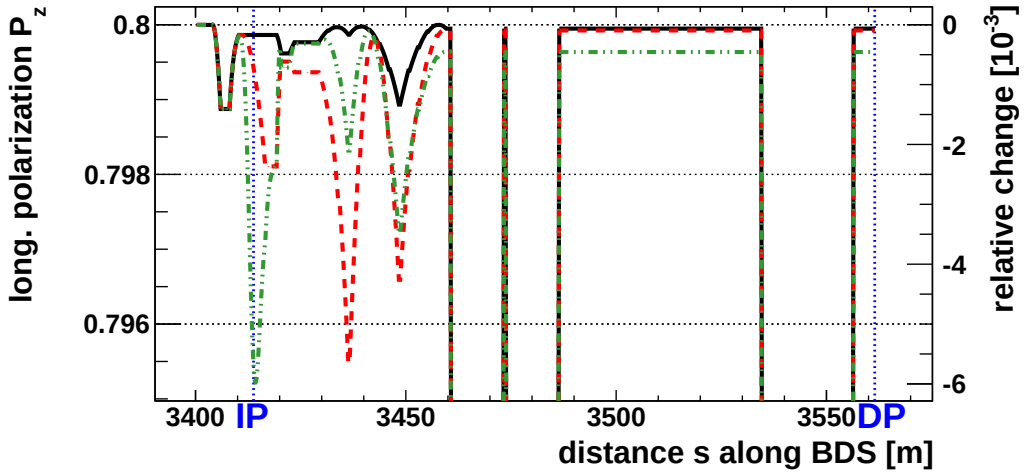

(b)

Figure 8.10: Entire polarization (a) and longitudinal polarization (b) along the BDS between IP and downstream polarimeter (DP) for the three samples listed in table 8.3.

smaller inside the solenoid, the effect of the longitudinal T-BMT precession shrinks correspondingly.

Since the solenoid affects the polarization only negligibly, the same can be expected for anti-solenoids to remove the skew coupling (see above). Moreover, anti-solenoids even undo a part of the longitudinal T-BMT precession. A correction of the tilt in the extraction line (accounting for the half solenoid behind the IP) is not required, unless possibly with respect to the laser-bunch interaction. The alternative - skew quadrupoles instead of anti-solenoids -

would affect the angular divergence θ_r and thus the polarization. The size of this effect would have to be determined.

A possible correction scheme for the incident angles at the polarimeters and the IP (cf. section 7.4) has been discussed already in [47] and in section 2.4 of [37], leaving open whether it would be necessary to adjust the incident angle at the IP or simply calculate a corrected value from eq. 7.13. As eq. 7.15 illustrates, the uncertainty on the polarization grows not only with the uncertainty on ϑ_{bunch} (which is obvious), but also with ϑ_{bunch} itself. While for $\vartheta_{\text{bunch}} \lesssim 50\,\mu\text{rad}$, no correction is necessary, the tolerance for $\vartheta_{\text{bunch}} = 185.1\,\mu\text{rad}$ (sample "all magnets", at the IP) is rather small. If $\vartheta_{\text{bunch}} = 200\,\mu\text{rad}$ had been measured instead, the correction longitudinal polarization would be $\mathcal{P}_z^{\text{corr}} = 0.801$. Thus, this error of $\approx 15\,\mu\text{rad}$ would already use up the entire error budget of 0.1 % for the polarization transport.

If ϑ_{bunch} had been zeroed using correction magnets, the same measurement error would have contributed only an error of $3.6 \cdot 10^{-5}$ (table 7.7). Therefore, a correction by aligning the orbits using magnets is to prefer from the viewpoint of polarimetry.

This study has been performed with an ideal solenoid with a constant field B_{sol}. A more realistic model would account for variations of the local field $\vec{B}(\vec{r})$. However, the relevant effects for the polarization depend on the integrated field strength $\int B(l)\,dl$. Therefore, this an ideal solenoid suffices here, as long as the variations are small enough such that all particles experience the same integrated field strength. Since $B_{\text{sol}} \cdot L_{\text{sol}}$ is about equal for ILD and SiD, the effects on the polarization are expected to be similar as well.

Chapter 9

Collision Effects and Synchrotron Radiation

In this chapter, the effects of beam-beam collisions at the IP and the emission of synchrotron radiation during the transport through the beam delivery system are investigated. The collision effects comprise T-BMT precession and emission of beamstrahlung (see section 4.2.4), the synchrotron radiation (section 4.2.3) consists only of radiative depolarization.

As shown in section 8.2, the detector magnets distort and deflect the beams severely. In order to obtain the design luminosity (the luminosity is introduced in section 4.1.2), these distortions would have to be corrected by additional magnets. This correction is rather difficult, since the luminosity depends strongly on the exact bunch shape (section 8.7.1.3 in [7]), as is also demonstrated in chapter 10. Therefore, the detector magnets will not be taken into account in the following studies involving the effects of the beam-beam collisions. The crab cavities however will be included, since the bunch rotation to compensate the beam-beam crossing angle is essential to reach the design luminosity.

From the RDR [15] to the TDR [6], several beam parameters changed. A selection is listed in table 9.1. The reduced beam size raises the intensity of the collision effects, but the luminosity decreases due to the lower bunch collision frequency. For a further increase of the luminosity, the application of a waist shift[1] is planned, which was not foreseen in the RDR. These changes can not be reproduced with the RDR lattice, but samples with a similar amount of beamstrahlung and with a waist shift have been generated. Other samples

[1]The focussing of the beams at the IP is altered such that the vertical waist of each beam moves slightly in front of the IP. Due to to mutual electromagnetic interaction (pinch effect), the beams are then focussed even stronger, which yields a higher luminosity than focussing the beams exactly at the IP.

investigate the case of collisions without bunch rotation (to compensate the crossing angle) and the effects of beamstrahlung and synchrotron radiation being switched off artificially. Samples with luminosities comparable to the application of a waist shift and to omitted bunch rotation are generated for comparison.

Parameter	symbol		RDR	TDR
Bunches per train			2 625	1 312
Train frequency		[Hz]	5	5
Horizontal bunch size	σ_x^{D}	[nm]	639	474
Vertical bunch size	σ_y	[nm]	5.7	5.9
Beam energy spread (e^-/e^+)	σ_E/E	[10^{-3}]	1.4/1.0	1.24/0.7
e^+e^- luminosity	$\mathcal{L}$	[$10^{38}\,\mathrm{m}^{-2}\,\mathrm{s}^{-1}$]	2	1.47
incl. waist shift				1.8
Beamstrahlung parameter	$\Upsilon_{\mathrm{global}}$		0.048	0.062

Table 9.1: Selected beam parameters at the IP for $E_{\mathrm{CM}} = 500\,\mathrm{GeV}$ according to RDR and TDR. Values taken from [7] and [16].

To generate samples with different luminosities and amounts of beamstrahlung, the bunch parameters have to be altered. In reality, one would alter the beam sizes by changing the focussing. For this study, the bunch charge is altered instead, in order to avoid having to make changes to the lattice of the beamline. The bunch charge corresponds to the number of particles per bunch N_e. The beamstrahlung parameter $\Upsilon_{\mathrm{global}}$ (see section 4.2.4) is approximately proportional to N_e; the luminosity $\mathcal{L}$ is approximately proportional to N_e^2.

Table 9.2 contains a complete list of the samples used in this section.

9.1 Synchrotron Radiation during Transport

Emission of synchrotron radiation affects the polarization in two different ways: Directly by possible spin-flips and indirectly by the recoil from the emission of the photon and the energy loss, which affects the polarization via a different trajectory and a different $(a\gamma + 1)$-factor. The direct effect is assessed in the following, using eq. 4.20. While the position of particle is not relevant traversing a dipole magnet, the magnetic fields and thus the synchrotron radiation rise with growing distance to the reference orbit. For the lattice as introduced in section 7.1.1, the accumulated spin-flip probability for an electron traversing the entire BDS lattice hypothetically at $x = 11\,\mathrm{mm}$

sample name	description
Ref.	The reference sample. All beam parameters as in table 7.1, $N_e^{\text{macro}} = 40\,000$, including bunch rotation by crab cavities, no waist shift, the emission of synchrotron radiation during the transport is simulated.
no SR	Sample without synchrotron radiation. In contrast to the reference sample, the emission of synchrotron radiation during the transport is not simulated, but beamstrahlung and the corresponding spin-flips (Sokolov-Ternov effects) are.
no BS,SR	Sample without beamstrahlung and synchrotron radiation. In contrast to the reference sample, neither the emission of synchrotron radiation during the transport nor beamstrahlung is simulated. Thus the energy of each particle is preserved.
no CC	Sample without bunch rotation. In contrast to the reference sample, the crab cavities are switched off. The crossing angle is left unchanged.
WS	Sample with waist shift. In contrast to the reference sample, a vertical waist shift of $250\,\mu$m is applied.
$\mathcal{L}_{\text{noCC}}$	Sample with a luminosity corresponding to the sample "no CC". The crab cavities are switched on. In contrast to the reference sample, it contains only $N_e = 1.071 \cdot 10^{10}$ particles per bunch instead of $2 \cdot 10^{10}$. The number of macroparticles N_e^{macro} remains unchanged.
$\mathcal{L}_{\text{WS}}$	Sample with a luminosity corresponding to the sample "WS". No waist shift is applied. In contrast to the reference sample, it contains $N_e = 2.085 \cdot 10^{10}$ particles per bunch.
Υ_{TDR}	Sample with a beamstrahlung parameter Υ_{global} corresponding to the TDR, calculated according to eq. 4.27 from the change in the beam sizes. In contrast to the reference sample, it contains $N = 2.69 \cdot 10^{10}$ particles per bunch.

Table 9.2: Simulated samples for the investigation of the beam-beam collision effects.

and $y = 2\,\text{mm}$ has been computed to $6.4 \cdot 10^{-6}$, along the relevant beamline section of the beamline between upstream polarimeter and downstream polarimeter it is only $7.3 \cdot 10^{-7}$. This is also the maximum change in po-

larization which could possibly result from the spin-flips. Furthermore, this estimation does not take into account that the beams are (especially in front of the IP) much smaller; $\sigma_x \approx 11\,\mathrm{mm}$ and $\sigma_y \approx 2\,\mathrm{mm}$ are the maximum values the beam sizes reach at two different positions in the extraction line after collisions under optimum conditions. Thus, the spin-flips during the transport can be neglected and do not have to be implemented in the spin transport simulation. The indirect effects from the recoil and the energy loss are investigated in the following.

Table 9.3 lists selected beam parameters for the samples "no SR" and "Ref.", which illustrate the effects of synchrotron radiation on the particle transport, which again may affect the polarization. Due to the additional undulator section and the following dogleg, the mean energy loss $\langle\delta\rangle$ is larger for the electrons than for the positrons. The beam energy spread σ_E/E is however only slightly increased. The design lattice did apparently not take the gradual losses in energy and magnetic rigidity (see section 6.1.2) into account; therefore, the magnets further downstream the beamline bend the beam stronger than they are supposed to. Since all chicanes and double curves in front of the IP are set up in the horizontal plane, only the horizontal bunch parameters are affected. Naïvely, one would expect from figure 2.2 a positive sign for $\langle x'\rangle$ due to the gradual energy loss in the double curves, but the sign of the angle is reversed by the final focus magnets. Furthermore, the loss in magnetic rigidity affects also the angular divergence θ_x, the mean bunch position $\left\langle x^{\mathrm{D}}\right\rangle$ and the bunch size σ_x^{D}, which is not investigated in detail here. A correction of the bunch parameters is simulated in chapter 10, showing that a correction of the incident angle θ_x is not necessary for the investigation of the collision effects later in this chapter.

Table 9.4 lists the polarization parameters for the samples "no SR" and "Ref." at the IP and the downstream polarimeter. Despite the change in the incident angles for the sample "Ref.", the longitudinal polarizations $\mathcal{P}_z$ and $\mathcal{P}_z^{\mathrm{D}}$ are mostly unchanged. However, the quotient b of the polar angles takes a value which is not compatible with $a\gamma + 1 \approx 568$. This does not come as surprise, since eq. 4.15 does not apply for radiative depolarization. To quantify the additional uncertainty on the spin transport, the relative deviation of $\mathcal{P}_z^{\mathrm{corr}}$ from $|\vec{\mathcal{P}}|$ at the downstream polarimeter is used (like for the longitudinal T-BMT precession in section 8.2.3), which amounts to $5{\cdot}10^{-6}$ and is thus negligible.

particle	parameter		no SR	Ref.
e^-	$\langle\delta\rangle$	$[10^{-3}]$	0.000 ± 0.006	-0.985 ± 0.006
	σ_E/E	$[10^{-3}]$	1.240 ± 0.005	1.250 ± 0.004
	$\langle x'\rangle$	[μrad]	-0.3 ± 0.2	-11.2 ± 0.2
	θ_x	[μrad]	32.4 ± 0.1	33.4 ± 0.1
	$\langle x^{\mathrm{D}}\rangle$	[nm]	-22 ± 3	-7 ± 3
	σ_x^{D}	[nm]	640 ± 2	627 ± 2
e^+	$\langle\delta\rangle$	$[10^{-3}]$	0.000 ± 0.004	-0.229 ± 0.003
	σ_E/E	$[10^{-3}]$	0.700 ± 0.002	0.703 ± 0.002
	$\langle x'\rangle$	[μrad]	0.3 ± 0.2	2.3 ± 0.2
	θ_x	[μrad]	30.9 ± 0.1	31.0 ± 0.1
	$\langle x^{\mathrm{D}}\rangle$	[nm]	19 ± 3	93 ± 3
	σ_x^{D}	[nm]	637 ± 2	639 ± 2

Table 9.3: Comparison of selected parameters of the simulated beams at the IP without (no SR) and with (Ref.) synchrotron radiation damping. No collisions are simulated.

9.2 Simulation of the Collision Effects

The collision effects are simulated with Guinea-Pig++ 1.2.1 [20], which is a descendant of Guinea-Pig [53] that includes spin tracking (see section 4.2.4). For that purpose, the particle bunches tracked to the IP by Bmad are fed into Guinea-Pig++. The spent beams given out by Guinea-Pig++ are then read again by Bmad and tracked to the downstream polarimeter. Guinea-Pig++ is also used to simulate the waist shift and to calculate the e^+e^- luminosity and the luminosity-weighted polarization, which is introduced in section 4.1.2.

When the colliding bunches approach each other, they distort each other by their electromagnetic fields continuously throughout the collision. In the simulation, the bunches are tracked by Bmad up to the IP without any bunch-bunch interaction, where they are handed over to Guinea-Pig++ in order to simulate the collision. Guinea-Pig++ tracks the bunches backwards to a point in front of the IP where the simulation of the interaction starts. Likewise, the simulation ends at a point behind the IP from which the particles are tracked back to the positions at the IP where they would have come from if there had been no bunch-bunch interaction. Then the distorted bunches are returned to Bmad to be tracked further to the downstream polarimeter.

When the collision effects are discussed in the following, the positions called "before collision"/"without collision" and "after collision" are the transfer points between Bmad and Guinea-Pig++ as explained above.

position	sample	no SR	Ref.
IP	$\mathcal{P}_x$	$-0.000\,04\,(7)$	$-0.007\,62\,(7)$
	$\mathcal{P}_y$	$0.000\,00\,(3)$	$-0.000\,00\,(3)$
	$\mathcal{P}_z$	$0.799\,863\,0\,(8)$	$0.799\,818\,(1)$
	$\mathcal{P}_z^{\mathrm{D}}$	$0.799\,843\,7\,(9)$	$0.799\,851\,5\,(9)$
	$\lvert\vec{\mathcal{P}}\rvert$	$0.799\,863\,0\,(8)$	$0.799\,854\,0\,(9)$
	$\vartheta_{\mathrm{bunch}}$ [μrad]	0.4 ± 0.2	11.2 ± 0.2
	ϑ_{pol} [mrad]	0.09 ± 0.05	9.53 ± 0.09
	ϕ_{bunch} [°]	180 ± 23	-180.0 ± 0.4
	ϕ_{pol} [°]	179 ± 82	-180.0 ± 0.2
	b	$340 \pm 1\,042$	849 ± 5
	$\mathcal{P}_z^{\mathrm{corr}}$	$0.799\,863\,0\,(8)$	$0.799\,834\,0\,(9)$
DP	$\mathcal{P}_x$	$0.000\,19\,(5)$	$0.000\,12\,(5)$
	$\mathcal{P}_y$	$-0.000\,000\,(3)$	$-0.000\,050\,(3)$
	$\mathcal{P}_z$	$0.799\,947\,9\,(4)$	$0.799\,945\,3\,(4)$
	$\lvert\vec{\mathcal{P}}\rvert$	$0.799\,947\,9\,(4)$	$0.799\,945\,3\,(4)$
	$\vartheta_{\mathrm{bunch}}$ [μrad]	0.20 ± 0.08	5.67 ± 0.08
	ϑ_{pol} [mrad]	0.24 ± 0.06	0.16 ± 0.05
	ϕ_{bunch} [°]	-0 ± 11	1.11 ± 0.09
	ϕ_{pol} [°]	-0 ± 1	-26 ± 12
	b	$1\,354 \pm 981$	29 ± 9
	$\mathcal{P}_z^{\mathrm{corr}}$	$0.799\,947\,9\,(4)$	$0.799\,949\,4\,(4)$

Table 9.4: Polarization and the related parameters of the electron beam at the IP and the downstream polarimeter (DP) as introduced in section 3.2.5. Compared are the parameters for the transport without (no SR) and with (Ref.) synchrotron radiation damping. No collisions are simulated.

9.3 Luminosity and Beamstrahlung

Table 9.5 lists the e^+e^- luminosities $\mathcal{L}$ and the maximum occurring beamstrahlung parameters Υ_{max} calculated by Guinea-Pig++ for the different samples and confronts them with the design values. The design values do not account for energy losses due to synchrotron radiation.

For the samples "Ref.", "no SR" and "no BS,SR" the simulated luminosity agrees with the design value to a level of 1 %, which is well within the precision range of the design value. If synchrotron radiation during the transport is simulated, the luminosity increases slightly, most likely due to smaller horizontal beam size (cf. table 9.3). Therefore, a correction of the

sample	luminosity $[10^{38}\,\mathrm{m}^{-2}\,\mathrm{s}^{-1}]$		beamstrahlung parameter	
	design value	simulation output	design value $2.4 \cdot \Upsilon_{\mathrm{global}}$	simulation output Υ_{max}
Ref.	2	2.02 ± 0.02	0.12	0.134 ± 0.008
no SR	2	1.98 ± 0.02	0.12	0.13 ± 0.01
no BS,SR	2	1.97 ± 0.02		
Υ_{TDR}	4	3.84 ± 0.06	0.146	0.215 ± 0.008
WS		2.19 ± 0.02		0.136 ± 0.004
$\mathcal{L}_{\mathrm{WS}}$	2	2.21 ± 0.02		0.141 ± 0.007
no CC	0.6	0.504 ± 0.004		0.118 ± 0.003
$\mathcal{L}_{\mathrm{noCC}}$	0.6	0.509 ± 0.003		0.065 ± 0.005

Table 9.5: Design values and simulation results for the luminosities and the beamstrahlung parameters of the different samples, respectively. The design values do not account for energy losses due to synchrotron radiation. All luminosities are given in $10^{38}\,\mathrm{m}^{-2}\,\mathrm{s}^{-1} = 10^{34}\,\mathrm{cm}^{-2}\,\mathrm{s}^{-1}$, where 13 125 bunch collisions per second are assumed. The design value for "no CC" is calculated from eq. 9.1. The design values for "Υ_{TDR}", "$\mathcal{L}_{\mathrm{WS}}$" and "$\mathcal{L}_{\mathrm{noCC}}$" are calculated by scaling the RDR design value [16] with N_e^2. For a comparison to the Υ_{max} calculated by Guinea-Pig++, the design values $\Upsilon_{\mathrm{global}}$ are multiplied by 12/5 according to eq. 4.28.

bunch position and the incident angle has not been regarded necessary here. The simulated maximum beamstrahlung parameters Υ_{max} are $\approx 12\,\%$ larger than the design values, which have been calculated according to eq. 4.28. For the sample "Υ_{TDR}", the simulated luminosity agrees[2] with the RDR design value scaled with N_e^2, but the maximum occurring beamstrahlung parameter is 50 % larger than the design value calculated according to eq. 4.28. For comparison, $\Upsilon_{\mathrm{global}}$ is calculated from the sizes of the simulated bunches according to eq. 4.27. The results are listed in table 9.6 and agree with the design values to a level of 1 %. Therefore, the most likely explanation for the discrepancy in Υ_{max} is that the approximations eq. 4.28 and/or eq. 4.27 do not hold here.

Continuing the discussion of table 9.5, the application of a waist shift ("WS") increases the luminosity by $\approx 10\,\%$, whereas 22 % are foreseen for the TDR. This discrepancy is mostly likely caused by the different bunch

[2] Altering of the bunch charge affects the luminosity in different manner than a change of the beam sizes would have. Therefore, the simulated luminosity in table 9.5 does correspond to the design value from table 9.1. Furthermore, the reduced number of bunches per train for the TDR is not taken into account here.

sample	design value	Υ_{global} from sim. bunch parameters e^--beam	e^+-beam
Ref.	0.048	$0.046\,7 \pm 0.000\,2$	$0.045\,9 \pm 0.000\,2$
no SR	0.048	$0.045\,8 \pm 0.000\,2$	$0.046\,0 \pm 0.000\,2$
Υ_{TDR}	0.062	$0.062\,9 \pm 0.000\,3$	$0.061\,8 \pm 0.000\,3$

Table 9.6: Beamstrahlung parameter Υ_{global}: design values and values calculated according to eq. 4.27 from the simulation results for the bunch sizes for selected samples.

sizes leading to a less strong effect of the waist shift. For the sample "no CC", a coarse estimate for the luminosity without bunch crabbing can be calculated (section 4.1, eq. (8) in [34]), ignoring the pinch effect:

$$\frac{\mathcal{L}(\text{CC off})}{\mathcal{L}(\text{CC on})} \approx \frac{1}{\sqrt{1 + \left(\frac{\sigma_z}{\sigma_x} \tan\left(\frac{\zeta}{2}\right)\right)^2}} \tag{9.1}$$

This value agrees to a level of $\approx 16\,\%$ with the simulation, which is regarded as acceptable.

9.4 Particle Transport after Collision

Table 9.7 lists selected parameters of the electron beam at the IP before and after the collision as defined in section 9.2. The parameter $N_{\text{lost}}^{\text{macro}}$ denotes the number of lost macroparticles. Since misalignments have not been introduced yet, there are no losses occurring along the beamline. In the collision, a small number of macroparticles gets lost for computational reasons: the grid which is used internally for the simulation of the collision extends only up to $z^{\text{D}} = 1\,\text{mm} \approx 3.3\sigma_z$. This cutoff was chosen as compromise between the accuracy of the simulation and the required CPU time. The macroparticles outside the grid are not taken into account by Guinea-Pig++ are therefore lost. This affects less than $0.1\,\%$ of the macroparticles. As result, the bunch length σ_z is slightly reduced, which otherwise not affected by the collision. The effects of the z^{D}-cutoff on all other bunch parameter are expected to be negligible, since the other bunch parameters are not correlated[3] with z^{D}. The emission of beamstrahlung leads to a energy loss in the collision, which

[3] This is not true for x, which might lead to a slight decrease in σ_x. However, relevant for the collision is σ_x^{D}, which is not affected by the cutoff.

agrees well with the design value ($\Delta \langle\delta\rangle = 2.4\,\%$ according to [16], table 2.1-2), as well as to a rise of the beam energy spread. The resulting beam energy spectrum after the collision is drawn in figure 9.1, since the standard deviation does not provide an accurate description for such an asymmetric spectrum. Even though single particles lose up to 60 % of their energy, most particles lose only a small fraction of their energy. Back to table 9.7: as result of the bunch-bunch interaction, the angular divergences θ_x and θ_y and the vertical beam size σ_y are noticeably enlarged, whereas the much larger horizontal beam size σ_x^{D} is not affected by the collision. To cross-check the simulation, the angular divergences after the collision can be estimated using eqs. 4.21 and 4.22 in absence of beamstrahlung. Table 9.8 confronts the estimated values with the simulation results from the sample "no BS,SR"[4]. The calculated results agree with the simulation to a level of $\approx 10\,\%$, which is regarded as sufficient for these approximations.

parameter		simulation output	
		before collision	after collision
$N_{\mathrm{lost}}^{\mathrm{macro}}$		0 ± 0	34 ± 6
$\langle\delta\rangle$	$[10^{-3}]$	-0.985 ± 0.006	-25.1 ± 0.3
σ_E/E	$[10^{-3}]$	1.250 ± 0.004	43.7 ± 0.5
σ_x^{D}	[nm]	627 ± 2	627 ± 2
σ_y	[nm]	5.76 ± 0.02	8.6 ± 0.1
σ_z	[nm]	0.300 ± 0.001	0.298 ± 0.001
θ_x	[μrad]	33.4 ± 0.1	204 ± 1
θ_y	[μrad]	14.39 ± 0.05	29.0 ± 0.9

Table 9.7: Selected parameters of the electron beam at the IP before and after the collision (sample "Ref.").

parameter		estimated	simulation output
θ_x	[μrad]	≈ 184	203 ± 1
θ_y	[μrad]	≈ 31	29.0 ± 0.7

Table 9.8: Angular divergences at the IP after the collision. The estimated values are calculated from eqs. 4.21 and 4.22, the simulation output is taken from the sample "no BS,SR".

Table 9.9 lists the same parameters as table 9.7 now for the electron beam

[4]Since the photons are radiated off with an average angle of γ^{-1} which is here $\approx 2\,\mathrm{mrad}$ and the photon energies are typically $\ll E_0$, the angular divergences of the samples "Ref." and "no BS,SR" hardly differ.

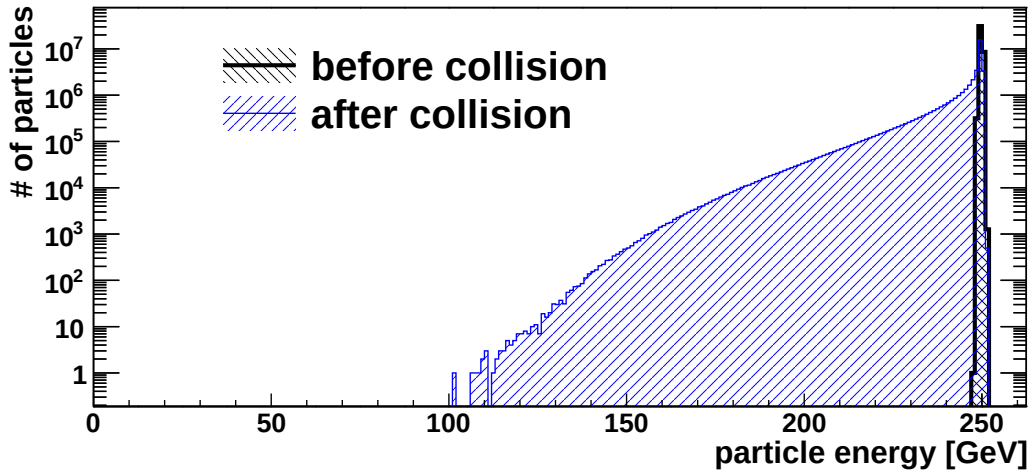

Figure 9.1: Energy distribution in the electron bunches at the IP before and after collision (sample "Ref."). The particles of 1000 simulated bunches are accumulated in this plot.

at the downstream polarimeter. Compared to table 9.7, the energy losses $\langle\delta\rangle$ have increased by 0.1 % due to emission of synchrotron radiation along the extraction line, while the energy spreads σ_E/E remain mainly unchanged. If no collisions occur, the considerations from section 7.2.2 regarding the laser-bunch interaction still apply, even though the number are slightly different due to the inclusion of synchrotron radiation emission. After a collision, the transverse beam sizes at the downstream polarimeter are about two orders of magnitude larger due to the disruption in the collision and the transport through the extraction line with the much larger energy spread. The latter affects also the incident angle at the downstream polarimeter, such that $\theta_x(\mathrm{DP}) = 0.58\,\theta_x(\mathrm{IP})$ instead of $0.5\,\theta_x(\mathrm{IP})$. Since θ_x is still negligible compared to the laser incident angle $\vartheta_0 = 10\,\mathrm{mrad}$, it does not have any impact on the laser-bunch interaction. In the following, the particle positions as a function of the particle are investigated more closely.

Figure 9.2 shows the horizontal particle position x against the particle energy at the downstream polarimeter. Without collision, the position is hardly correlated with energy. After a collision, the bulk of the particles, which has hardly lost any energy in the collision, is contained within a range of less than 0.5 mm around $x = 0$, whereas the low-energy electrons are spread out much further. To describe the transport of particles that have lost a a large amount of energy through the extraction line, eq. 5.10 is no longer sufficient; but the higher-order terms have to be taken into account as well. This also explains why $\langle x\rangle$ does not correspond to the position of the

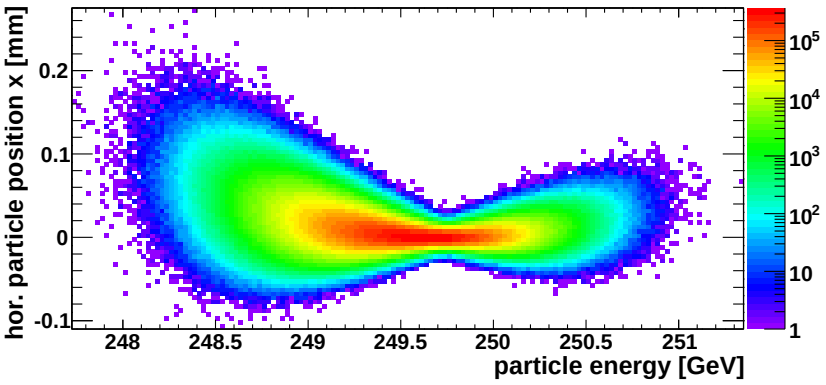

(a)

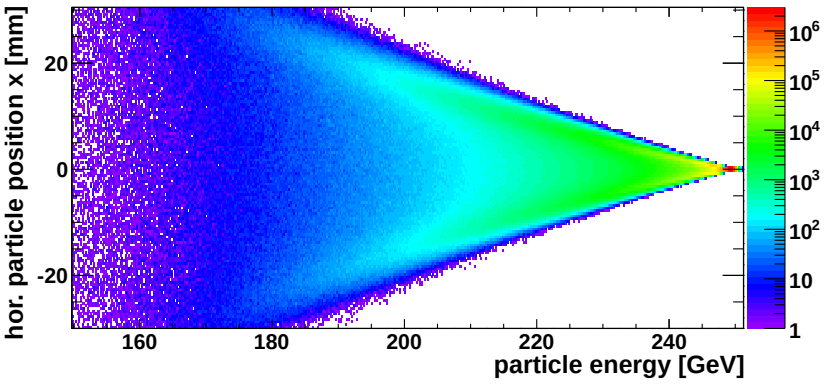

(b)

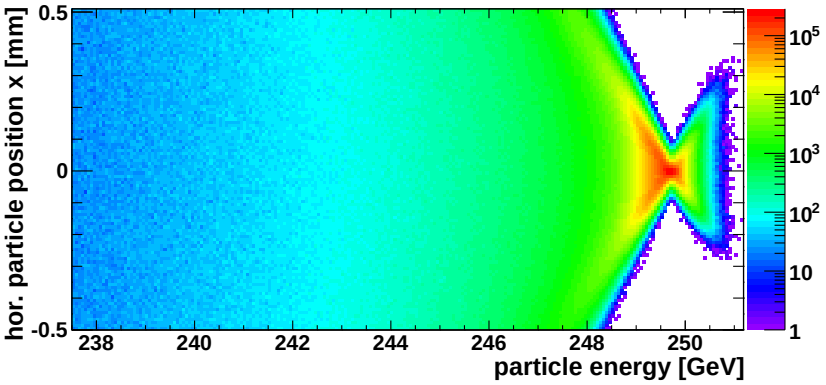

(c)

Figure 9.2: Horizontal particle positions vs. the energy at the downstream polarimeter for 1000 electron bunches before (a) and after (b,c) the collision (sample "Ref."). The pixel sizes are 0.025 GeV×0.005 mm (a), 0.25 GeV×0.5 mm (b) and 0.0625 GeV×0.01 mm (c), respectively.

parameter		simulation output	
		without collision	after collision
$N_{\text{lost}}^{\text{macro}}$		0 ± 0	34 ± 6
$\langle\delta\rangle$	$[10^{-3}]$	-2.083 ± 0.006	-26.2 ± 0.3
σ_E/E	$[10^{-3}]$	1.287 ± 0.004	43.6 ± 0.5
σ_x	$[\mu\text{m}]$	14.7 ± 0.1	$3\,010 \pm 53$
σ_y	$[\mu\text{m}]$	39.1 ± 0.1	$1\,229 \pm 39$
σ_z	[mm]	0.300 ± 0.001	0.299 ± 0.001
θ_x	$[\mu\text{rad}]$	16.78 ± 0.06	117.6 ± 0.8
θ_y	$[\mu\text{rad}]$	1.755 ± 0.006	7.3 ± 0.2
$\langle x\rangle$	$[\mu\text{m}]$	6.02 ± 0.07	242 ± 19
$\langle y\rangle$	$[\mu\text{m}]$	-24.6 ± 0.2	-569 ± 16

Table 9.9: Selected parameters of the electron beam at the downstream polarimeter (DP) with and without collision (sample "Ref.").

bulk of the particles, as figure 9.2c shows.

Figure 9.3 shows the vertical particle position y against the particle energy at the downstream polarimeter, which looks very similar apart from an additional correlation, which is explained in the following. The laser-bunch IP of the downstream polarimeter is located in a magnet chicane (see figure 5.4), which generates dispersion. From the properties of the chicane, one can calculate the expected offset for a hypothetical particle that differs from the reference particle only by the energy as follows: the bending angle (cf. eq. 6.2) in the chicane magnets is given as function of the electron energy E by

$$\alpha(E) = \frac{B\ L\ q}{|\vec{p}|} \approx \frac{B\ L\ q}{E_0} \cdot \frac{E_0}{E} = \alpha(E_0) \cdot \frac{E_0}{E}, \tag{9.2}$$

where B and L are the field strength and the length of the bending magnet, q and p the charge and the momentum of the electron, and $E_0 = 250\,\text{GeV}$ the design beam energy. For the magnets BVEX1P and BVEX2P (cf. figure 5.4), the nominal bending angle is $\alpha(E_0) = 1\,\text{mrad}$. The transverse shift $\tilde{y}(E)$ at the laser-bunch IP with respect to the reference orbit in front the chicane amounts to

$$\tilde{y}(E) = \Delta s \cdot \sin\big(\alpha(E)\big) = \Delta s \cdot \sin\left(\alpha(E_0) \cdot \frac{E_0}{E}\right), \tag{9.3}$$

where $\Delta s = 20\,\text{m}$ is the distance between the magnets BVEX1P and BVEX2P. Subtraction of the shift for the nominal energy yields the particle coordinate

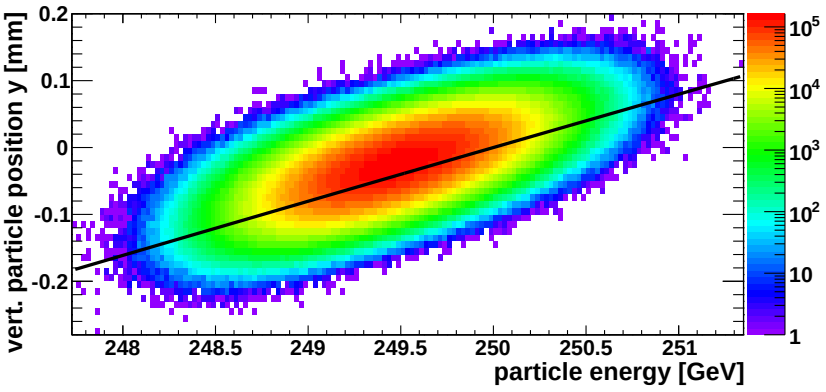

(a)

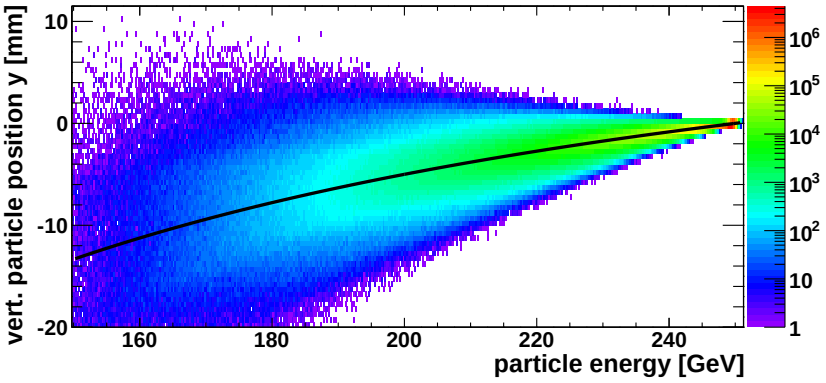

(b)

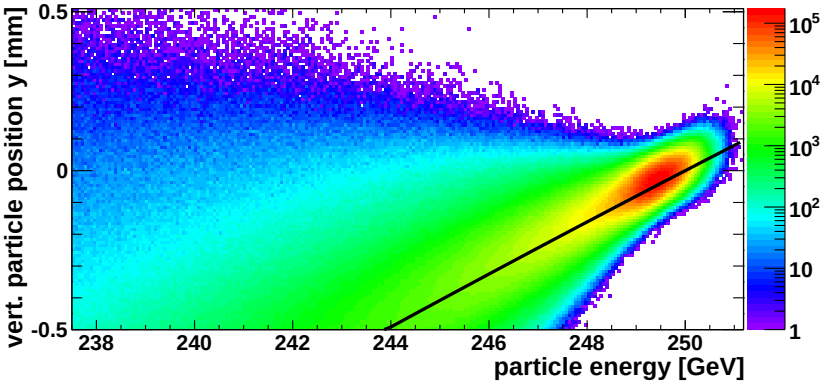

(c)

Figure 9.3: Vertical particle positions vs. the energy at the downstream polarimeter for 1000 electron bunches before (a) and after (b,c) the collision (sample "Ref."). The pixel sizes are 0.025 GeV×0.01 mm (a), 0.25 GeV×0.5 mm (b) and 0.0625 GeV×0.01 mm (c), respectively. The black solid curve is the expected y-coordinate according to eq. 9.5.

as function of the energy:

$$y(E) = \tilde{y}(E) - \tilde{y}(E_0) \tag{9.4}$$

$$= \Delta s \cdot \left(\sin\left(\alpha(E_0) \cdot \frac{E_0}{E} \right) - \sin\left(\alpha(E_0) \right) \right)$$

$$= 20\,\mathrm{m} \cdot \left(\sin\left(\frac{0.25\,\mathrm{GeV}}{E} \right) - 0.001 \right). \tag{9.5}$$

$y(E)$ is drawn in figure 9.3 as well and in good agreement with the simulation output. Hence, such a hypothetical particle with an energy $E = 248.75\,\mathrm{GeV}$ (i. e. $\delta = -5 \cdot 10^{-3} \approx 0.2\,\langle\delta\rangle$) is already expected to miss a $100\,\mu$m wide laser-spot. The bulk of the particles, which has hardly lost any energy in the collision, is contained within a range of less than 0.5 mm around $y = 0$. Due to the asymmetric distribution, $\langle y \rangle$ does not correspond to the position of the bulk of the particles.

In conclusion, the polarization measurement at the downstream polarimeter omits a remarkable fraction of the particles which lost energy due to beamstrahlung in the collision, if a laser-spot size of $50\,\mu$m as suggested in [38] is chosen. The consequences of this selection for the measurement are discussed in the following section.

For the other samples, the collision effects on the bunch parameters are similar and therefore not discussed here in detail.

9.5 Measurable Polarization at the Downstream Polarimeter

Figure 9.4 shows the longitudinal polarization $\mathcal{P}_z$ of the macroparticles versus the particle energy E and its vertical position y, respectively, at the downstream polarimeter for the electron beam of the sample "Ref.". There is a clear correlation between E and $\mathcal{P}_z$ due to a common cause: the more beamstrahlung a macroparticle emits in the collision, the more energy and the more polarization it loses. Since E is correlated with y due to dispersion (see figure 9.3), there is also a correlation between the longitudinal polarization and the vertical position $|y|$. In the horizontal plane, there is no dispersion. Nevertheless, the correlation between E and $\mathcal{P}_z$ in conjunction with the correlation between E and the horizontal particle position $|x|$ (see figure 9.2) leads also to a lower longitudinal polarization for increasing $|x|$. This means that the downstream polarimeter tends to measure a larger value than the average longitudinal polarization of the whole bunch, since the laser-spot of

the polarimeter covers only the center of the bunch where the average $\mathcal{P}_z$ is larger. The discrepancy is the larger, the smaller the laser spot is.

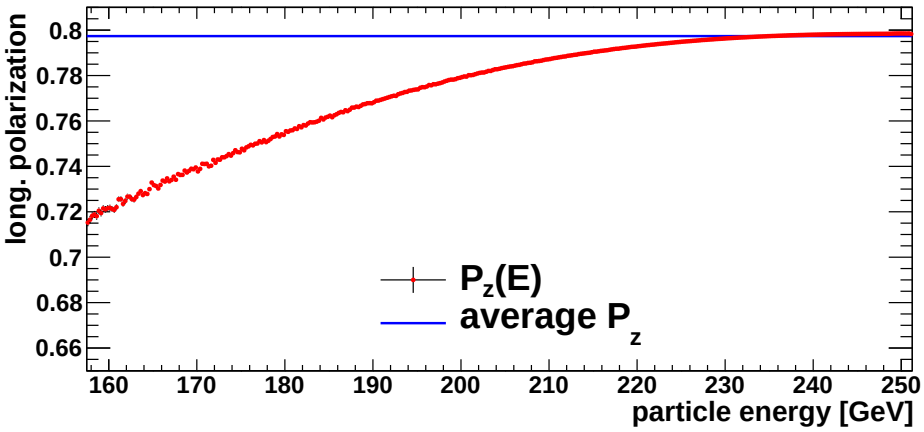

(a)

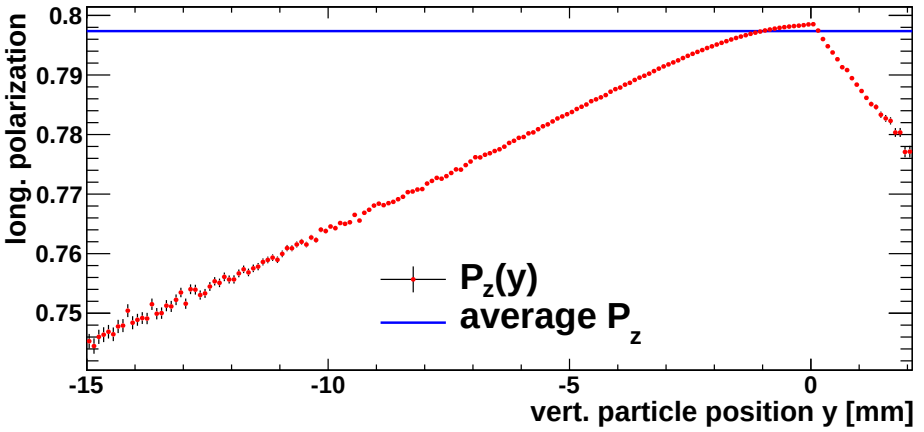

(b)

Figure 9.4: Longitudinal polarization $\mathcal{P}_z$ of the macroparticles versus the particle energy E (a) and the vertical particle position y (b) at the downstream polarimeter for the sample "Ref.".

In order to account for the transverse laser spot size without running a separate simulation of the laser-bunch interaction, a quantity named "measurable" polarization is defined here as follows: $\mathcal{P}_z^{mr}$ is the average longitudinal polarization of all macroparticles within a circle (i. e. the laser spot) of radius r in mm around the bunch center (as defined below) in the x-y plane. For example, $\mathcal{P}_z^{m0.1}$ corresponds to a radius of 0.1 mm. Assuming the laser pulse to be sufficiently long, there is no restriction in z. A light intensity

distribution within the laser spot is not taken into account.

In reality, the laser would be adjusted by searching for the maximum signal in the polarimeter. In this simulation, the adjustment is assumed to have already been performed successfully. As figures 9.2 and 9.3 show, most particles have lost only little energy and are concentrated in a spot at $x, y \approx 0$, which does not correspond to the mean positions $\langle x \rangle$ and $\langle y \rangle$. Therefore, the x-coordinate of the bunch center in the simulation is chosen to be the median value of the distribution of the x-coordinates of all particles with $\delta < 0.05$ ($E > 237.5\,\mathrm{GeV}$); the y-coordinate is obtained analogously. The bunch center is determined separately for each bunch, assuming that the adjustment has already been performed successfully and the bunch center position is stable over many bunch crossings. This will become relevant in chapter 10, where misalignments of the beamline elements lead to larger variations in the bunch positions.

The "measurable" polarization has been only calculated for the longitudinal component since the polarimeters are designed to measure only the longitudinal polarization. The results for different laser spot sizes are presented in the following section.

9.6 Spin Transport after Collision

Figure 9.5 shows the propagation of the polarization ($\mathcal{P}_z$ and $|\vec{\mathcal{P}}|$) along the BDS without and with collision effects for the electron beam of the sample "no BS,SR".

Also shown are $f(\theta_r)$ (see section 7.3) for the disrupted beam and the luminosity-weighted polarization in the collision ($\mathcal{P}_z^{\mathrm{lumi},1}$ and $|\vec{\mathcal{P}}|^{\mathrm{lumi},1}$) as introduced in section 4.1.2, which is the relevant quantity to be determined by the polarization measurement. The luminosity-weighted longitudinal polarization $\mathcal{P}_z^{\mathrm{lumi},1}$ is given in the detector coordinate system. Since the difference is negligible for a longitudinally polarized beam as shown in section 7.4.3, also the usual labeling of the symbol with the index D is omitted here.

In addition, table 9.10 lists the values of $\mathcal{P}_z$, $|\vec{\mathcal{P}}|$ and $f(\theta_r)$ at the IP and at the downstream polarimeter. The beam arrives at the IP with almost the initial longitudinal polarization. The mutual disruption of the bunches (spin fan-out due to T-BMT precession, see section 7.3.2) lowers the polarization by 0.6 %. The propagation of $|\vec{\mathcal{P}}|$ after the collision through the extraction line corresponds to the propagation of $f(\theta_r)$. The relative deviation of $|\vec{\mathcal{P}}|$ from $f(\theta_r)$ is 0.06 % at the IP and 0.03 % at the downstream polarimeter, while there are variations of $> 5\,\%$ on the way between. This means that

the changes in $|\vec{\mathcal{P}}|$ can still be fully explained by spin fan-out, even though the amplitudes of the fan-out are much larger in the extraction line after collision. Furthermore, it indicates that the used approximations in the spin transport still hold for the disrupted beams (cf. section 7.3.3).

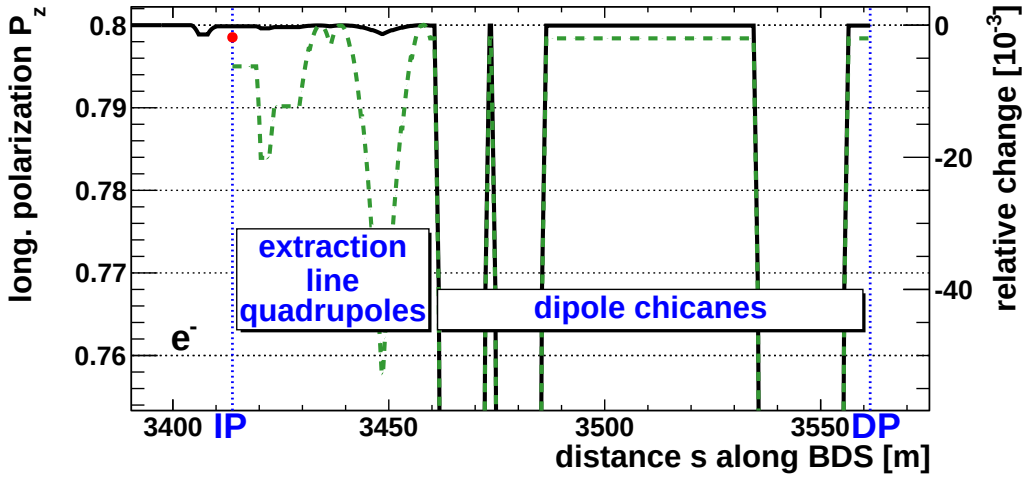

(a)

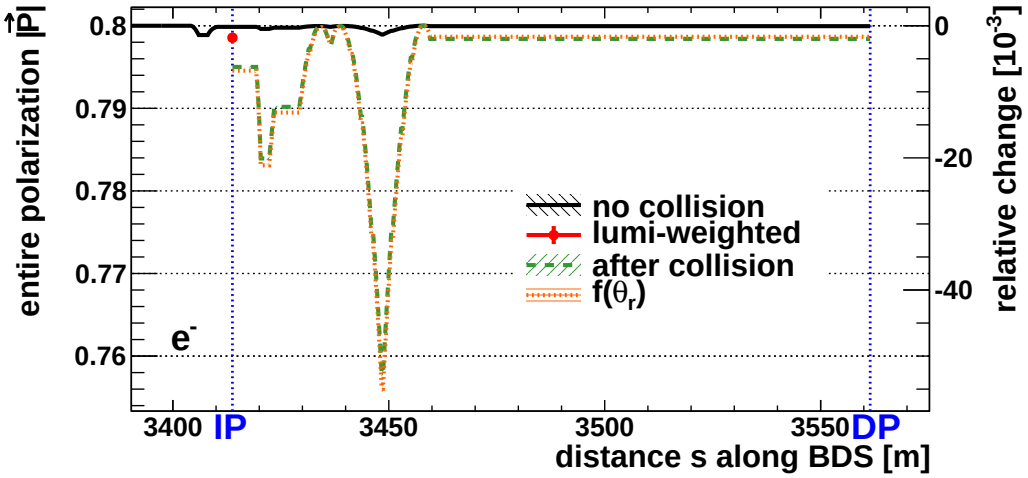

(b)

Figure 9.5: Longitudinal (a) and entire polarization (b) of the electron beam along the BDS for the sample "no BS,SR". Shown are the propagation in the case of no collisions, the different propagation after the collision and the luminosity-weighted polarization in the collision. In (b), also $f(\theta_r)$ after the collision is drawn (eq. 7.8).

To verify the simulation results, the quotient Q according to eq. 4.24 has been calculated from the three simulated polarization values at the IP:

position	$\mathcal{P}_z$	$\lvert\vec{\mathcal{P}}\rvert$	$f(\theta_r)$
IP, before collision	0.799 863 0 (8)	0.799 863 0 (8)	0.799 838 1 (9)
IP, luminosity-weighted	0.798 53 (2)	0.798 55 (2)	
IP, after collision	0.795 01 (5)	0.795 01 (5)	0.794 56 (6)
downstream polarimeter	0.798 40 (2)	0.798 40 (2)	0.798 67 (1)

Table 9.10: Longitudinal polarization $\mathcal{P}_z$, (entire) polarization $|\vec{\mathcal{P}}|$ and the function $f(\theta_r)$ as defined in eq. 7.8 of the electron beam at the IP and the downstream polarimeter for the sample "no BS,SR".

$Q = 0.271 \pm 0.005$. This is in good agreement with the literature value 0.273 (eq. 4.25). The luminosity-weighted depolarization[5] $(|\vec{\mathcal{P}}|^{\mathrm{bef}} - |\vec{\mathcal{P}}|^{\mathrm{lumi,1}})/|\vec{\mathcal{P}}|^{\mathrm{bef}}$ in the collision (eq. 4.26) has already been investigated earlier [13]. Table 9.11 confronts the results of the earlier studies with the corresponding simulation results for the samples "no BS,SR" and "no SR" and shows that they agree sufficiently well.

sample	simulation output	previous study
no BS,SR	0.164 %	0.17 %
no SR	0.221 %	0.22 %

Table 9.11: Luminosity-weighted depolarization $(|\vec{\mathcal{P}}|^{\mathrm{bef}} - |\vec{\mathcal{P}}|^{\mathrm{lumi,1}})/|\vec{\mathcal{P}}|^{\mathrm{bef}}$. The reference values are taken from [13].

Figure 9.6 shows the propagation of the polarization like figure 9.5b, but for the sample "Ref.", which includes beamstrahlung effects and synchrotron radiation damping in addition. The propagation of the polarization through the BDS still corresponds qualitatively to the propagation of $f(\theta_r)$ despite the much larger energy spread, but with an offset due to the additional depolarization by the emission of beamstrahlung. In contrast to figure 9.5b, an additional spin fan-out occurs in the ramps of the magnet chicanes. This is caused by the larger energy spread after the emission of beamstrahlung, such that the term $\delta/(1+\delta)$ in eq. 7.5 can no longer be neglected. Therefore, an energy-spread-driven spin fan-out becomes noticeable, which in principle also occurs in the sample "no BS,SR", but is too small to be visible in figure 9.5b.

For the following comprehensive discussion of all samples, it is convenient to focus on the polarization values at the IP and at the polarimeters. Fig-

[5] The major part of it is spin fan-out and not (irrecoverable radiative) depolarization, as pointed out in section 4.2.4.

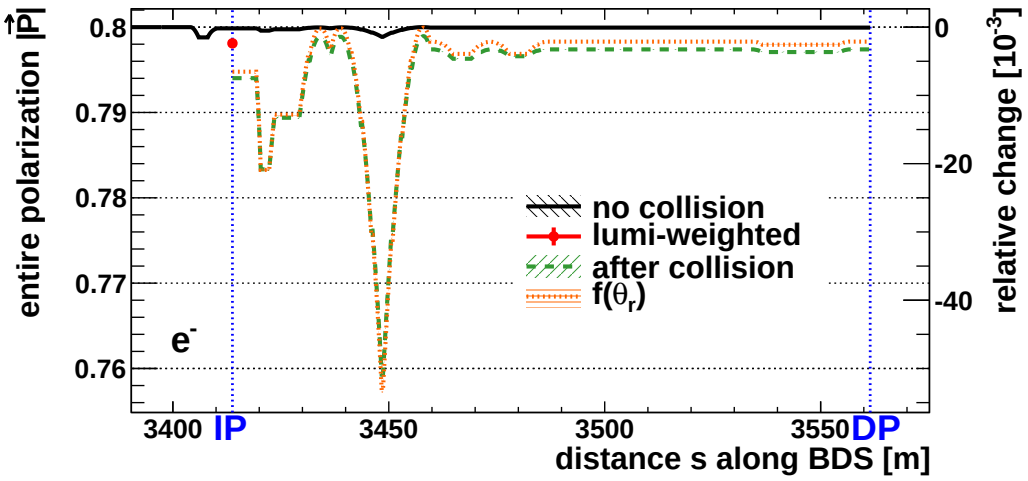

Figure 9.6: Polarization of the electron beam along the BDS. Like figure 9.5b, but for the sample "Ref.".

ure 9.7 shows the longitudinal and entire polarization $\mathcal{P}_z$ and $|\vec{\mathcal{P}}|$ at these positions for all samples introduced in table 9.2. The positions are denoted by the abbreviations IP, UP and DP for the beam-beam interaction point and the laser-bunch IPs of the up-/downstream polarimeters, respectively. At the IP, the longitudinal polarizations before and after the collision and the luminosity-weighted longitudinal polarization in the collision are shown. Analogously, the values of $|\vec{\mathcal{P}}|$ at different positions are shown. The measurable longitudinal polarization $\mathcal{P}_z^{mr}$ at the downstream polarimeter for different radii is drawn in figure 9.7 as well.

The propagation of the polarization through the extraction line for the sample "no BS,SR" has already been discussed above. As described in section 7.2.2, the lattice is designed to restore the value of $\mathcal{P}_z^{\text{lumi},1}$ at the downstream polarimeter. For this sample, the $\mathcal{P}_z^{mr}$ for all radii agree with $\mathcal{P}_z$ at the downstream polarimeter and $\mathcal{P}_z^{\text{lumi},1}$ to a level of $2 \cdot 10^{-4}$, which is sufficient with respect to the precision goal of 0.1 % (cf. section 5.2).

The sample "no SR" includes simulation of beamstrahlung which leads to additional depolarization, which affects likewise $|\vec{\mathcal{P}}|$ and $\mathcal{P}_z$. Furthermore, like for the sample Ref., $\theta_x(\text{DP}) > 0.5\,\theta_x(\text{IP})$ (cf. section 9.4), which lead to a larger spin fan-out. Therefore, $\mathcal{P}_z^{\text{lumi},1}$ is not fully restored at the downstream polarimeter. The measurable polarizations are larger than $\mathcal{P}_z^{\text{lumi},1}$ and decreases for larger laser spot radii. As described in section 9.5, the particles which have hardly emitted any beamstrahlung are concentrated in the bunch center, whereas the other particle are spread the further the more energy they have radiated off. Thus, a sufficiently small laser-spot selects only the par-

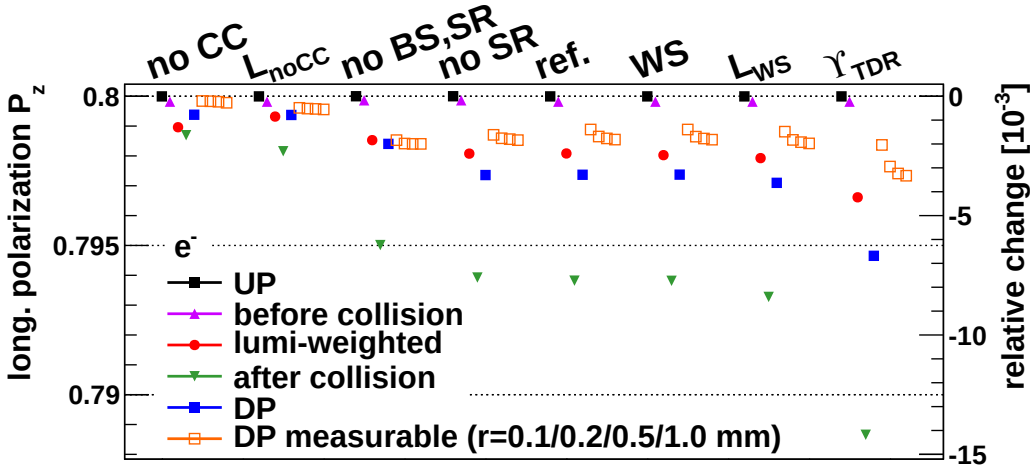

(a)

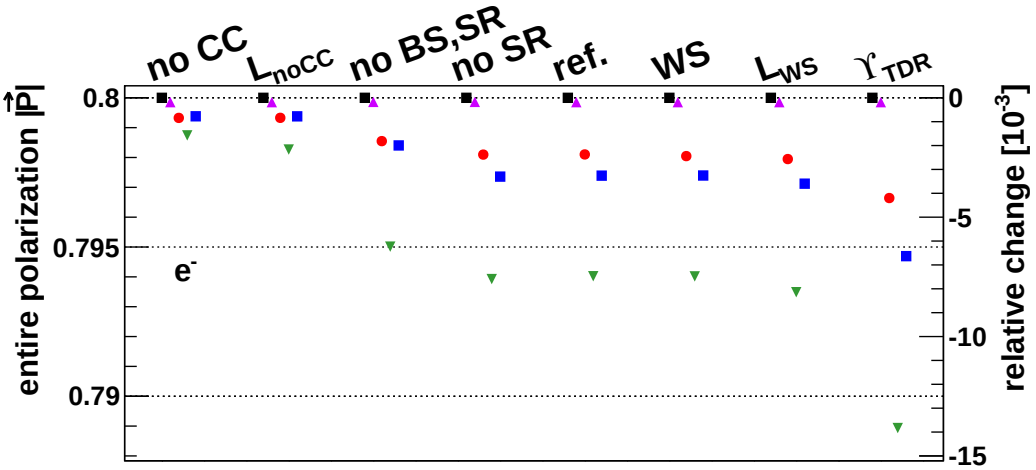

(b)

Figure 9.7: Electron beam polarization along the BDS at the IP and the polarimeters for the samples listed in table 9.2. Shown are the longitudinal (a) and entire (b) polarization of the electron beam at the upstream polarimeter (UP), at the IP before and after the collision as well as the luminosity-weighted polarization ($\mathcal{P}_z^{\mathrm{lumi},1}$, $|\vec{\mathcal{P}}|^{\mathrm{lumi},1}$) and at the downstream polarimeter. In (a), also the measurable longitudinal polarization $\mathcal{P}_z^{mr}$ (see section 9.5) for different radii is shown.

ticles which have hardly emitted any beamstrahlung. Since the emission of beamstrahlung is closely related to the deflection in the electromagnetic field of the oncoming bunch, it is most likely that the angular divergence θ_r of

only the particles in the bunch center is significantly smaller than the overall θ_r. This explains the larger value for the measurable polarizations.

The sample "Ref." differs from the sample "no SR" by the additional simulation of synchrotron radiation damping. The measurable polarizations are slightly increased and more dependent on the laser-spot size than for the sample "no SR". The reason for this still needs to be investigated. Since $\mathcal{P}_z^{\text{lumi,1}}$ and $\mathcal{P}_z(\text{DP})$ remain unchanged, the slightly increased luminosity with respect to the other samples (cf. table 9.5) cannot be the explanation. While $\mathcal{P}_z(\text{DP})$ is 0.1 % less than $\mathcal{P}_z^{\text{lumi,1}}$, $\mathcal{P}_z^{m0.1}$is 0.1 % larger than $\mathcal{P}_z^{\text{lumi,1}}$. This exhausts already the uncertainty budget for the spin tracking.

The sample "no CC" illustrates the effects of absent bunch rotation at the IP. Beamstrahlung is simulated, but even though the beamstrahlung parameter Υ_{max} is only moderately smaller (cf. table 9.5), $|\vec{\mathcal{P}}|^{\text{lumi,1}}$ and $|\vec{\mathcal{P}}|(\text{DP})$ agree. However, this is not the case for $\mathcal{P}_z^{\text{lumi,1}}$ and $\mathcal{P}_z(\text{DP})$, which implies a rotation of the polarization vector during the collision due to the asymmetry in x^{D}. The total change in polarization is significantly less than for the sample "Ref.", which has to be related to a remarkably weaker pinch-effect, since beamstrahlung is only moderately reduced. The relative deviation of $\mathcal{P}_z^{m0.1}$ from $\mathcal{P}_z^{\text{lumi,1}}$ is 0.11 %.

For comparison, the sample "$\mathcal{L}_{\text{noCC}}$" features collisions with bunch rotation, but with a luminosity similar to the previous sample and a remarkably smaller beamstrahlung parameter. Consequently, the results correspond qualitatively to the results for the sample "no BS,SR".

The sample "$\mathcal{L}_{\text{WS}}$" features likewise collisions with a luminosity similar to the sample "WS", which results in a slightly increased Υ_{max} and a larger angular divergence after the collision. The polarization behaves like in the sample "Ref.", but due to the larger θ_r and larger Υ_{max}, the gaps between $\mathcal{P}_z^{\text{lumi,1}}$, $\mathcal{P}_z(\text{DP})$ and $\mathcal{P}_z^{mr}$ are correspondingly larger.

For the sample "WS", θ_r is the same for the sample "Ref." and Υ_{max} is slightly increased, but not as much as for the sample "$\mathcal{L}_{\text{WS}}$". Even though the luminosity is 10 % larger than for the sample "Ref.", the effects on the polarization are still the same.

The sample "Υ_{TDR}" has been generated to feature the same amount of beamstrahlung as the TDR parameters (table 9.1). According to eqs. 4.21 and 3.10, is should feature a similar amount of T-BMT precession as well. The relative deviation of $\mathcal{P}_z(\text{DP})$ from $\mathcal{P}_z^{\text{lumi,1}}$ amounts to 0.25 %, and the relative deviation of $\mathcal{P}_z^{mr}$ from $\mathcal{P}_z^{\text{lumi,1}}$ amount to 0.22 % and 0.09 % for $r = 0.1\,\text{mm}$ and $r = 1.0\,\text{mm}$, respectively.

Figure 9.8 shows the longitudinal and entire polarization $\mathcal{P}_z$ and $|\vec{\mathcal{P}}|$ analogous to figure 9.7, but for the positron beam. While T-BMT precession has

the same relative effects on beam with different degrees of polarization (see section 7.3), this is a priori not the case for Sokolov-Ternov effects (radiative depolarization). However, in comparison to figure 9.7, the relative changes in polarization are quite similar. For the samples involving emission of synchrotron radiation along the beamline, the relative changes in the polarization are slightly larger for the positron beam. The laser spot size however affects the measurable longitudinal polarization remarkably less. The reason for these differences needs still to be investigated. Nevertheless, in terms of the uncertainty of the spin transport, the values for the electron beam can be regarded as upper limit.

9.7 Conclusion

In the previous sections, synchrotron radiation damping and the beam-beam collision effects have been added to the simulation. The collision effects have been studied for a number of different operation modes, which comprises different luminosities, application of a waist shift and collision without bunch rotation. The simulation results have shown to be in agreement with the predictions from theory and with earlier studies.

In absence of collisions, the direct influence of the emission of synchrotron radiation on the polarization is negligible. The gradual energy loss and the recoil of the photons slightly affect the particle trajectories. That can be compensated by correction magnets.

As it has been shown using the sample "no BS,SR", the effects of T-BMT precession are fully compensated by the lattice design, such that the downstream polarimeter could directly measure the luminosity-weighted longitudinal polarization $\mathcal{P}_z^{\mathrm{lumi},1}$, if no beamstrahlung and no synchrotron radiation were radiated off in the collision and in the extraction line, respectively.

The emission of beamstrahlung leads to additional depolarization which is not made up for by the lattice design, but the resulting loss in energy affects the particle trajectories, such that especially the low-energy particles miss the laser spot of the downstream polarimeter. This is however advantageous in view of the measurement: a large energy spread in the incoming particle beam would lead to a diffuse Compton spectrum without a sharp Compton edge and a sharp crossover point (see section 5.1.1). This would make the calibration of the polarimeter more difficult.

The energy loss by the emission of beamstrahlung affects the incident angles at the downstream polarimeter as well (see section 9.4), and thus the polarization via spin fan-out. With increasing beamstrahlung, also the dependence of the measurable polarization from the laser spot size at the

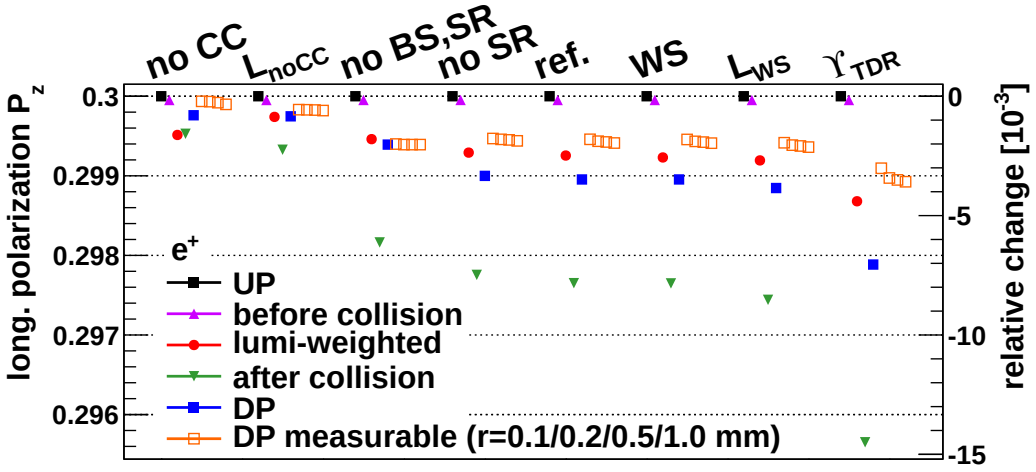

(a)

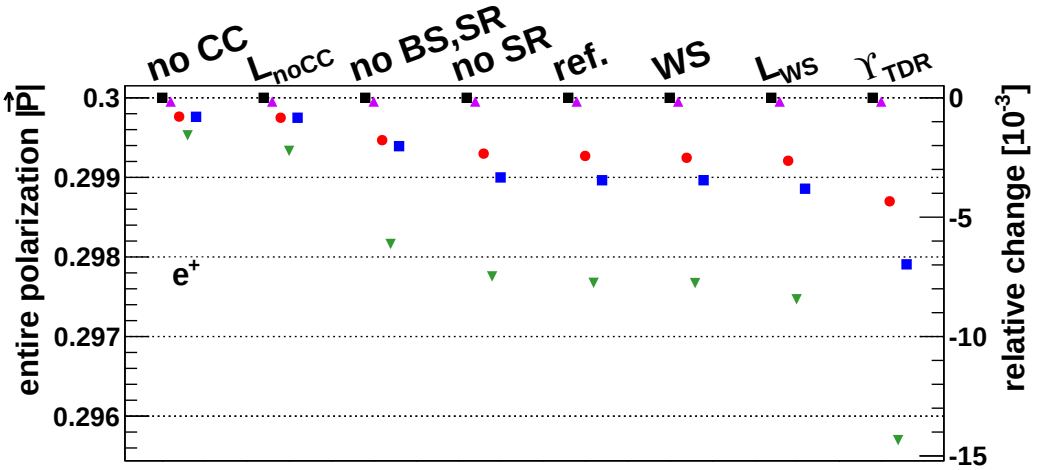

(b)

Figure 9.8: Positron beam polarization along the BDS at the IP and the polarimeters for the samples listed in table 9.2. Analogous to figure 9.7.

laser-bunch IP at the downstream polarimeter rises. For a beamstrahlung intensity comparable to the TDR beam parameters, the knowledge of the laser spot size becomes crucial for the interpretation of the measured longitudinal polarization.

Therefore, further studies are necessary regarding the effects of photon emission and the interaction between the laser and the electron bunch at the downstream polarimeter in order to derive the luminosity-weighted polarization from the measurement at the downstream polarimeter with the required precision. The former comprises a closer investigation of how the luminosity-

weighted longitudinal polarization $\mathcal{P}_z^{\mathrm{lumi},1}$ and longitudinal polarization $\mathcal{P}_z$ at the downstream polarimeter are related under the influence of beamstrahlung and synchrotron radiation; the latter a more detailed simulation including the light intensity distribution in the laser pulse and a measurable θ_r analogous to the measurable polarization. Based on a more detailed simulation, one could eventually determine the desired laser-spot size, which has to weigh the achievable measurement accuracy against the available laser power and the accuracy of the laser focus system.

The operation without bunch rotation at the IP has been shown to be problematic with respect to the polarization measurement and requires further studies as well, if it is regarded as possible operation mode, e. g. if the crab cavities are defect.

The application of a waist shift as a measure to increase the e^+e^- luminosity seems not to increase the spin fan-out and the depolarization at the IP, in contrast to other measures (e. g. increasing the bunch charge or reducing the beam sizes). Since the effect of the waist shift is expected to be remarkably stronger for the TDR parameters, this study should be repeated with the corresponding lattice and the corresponding beam parameters.

Chapter 10

Misalignments

Misalignments as introduced in section 6.4 are now included in the beamline simulation. Over time, misalignments increase due to ground motion. During operation periods with beam-beam collisions, these increases are be compensated for by the feedback orbit correction as introduced in section 6.5, until the misalignments have grown to a certain RMS magnitude (a few micrometers [48]). At this point (which is chosen in view of maximizing the time-integrated luminosity), a beam-based alignment is carried out, during which the misalignments and the required corrections are minimized and which requires the collisions to pause. After the beam-based alignment, the collisions are restarted, until a new beam-based alignment becomes necessary.

In this thesis, only static misalignments are simulated. The generated sets of misalignments represent time snapshot in the cycle described above, just before a realignment becomes necessary. Therefore, misalignments with a magnitude of few micrometers are studied in this chapter as "worst case".

Like in the preceding chapters, $N_{\mathrm{rep}} = 1\,000$ simulation runs with one electron bunch and one positron bunch each are generated for every data sample. For each run, the misalignments are generated randomly as Gaussian-distributed random numbers. The mean of the distribution is chosen to be zero, the standard deviation corresponds to the RMS magnitude. All beamline elements are treated in the same manner, without assuming a better alignment for critical elements like the final focus magnets. Unlike in more realistic models, the misalignments of neighboring elements are not correlated in this simulation. Initial beam jitter is not applied in this simulation.

Table 10.1 lists the samples which are used in this chapter. There are two orbit correction systems (slow and fast feedback) involved, which will be introduced in the following section. The sample "Ref." is the same as in chapter 9, does not contain any misalignments or orbit correction and serves as reference. The samples named "$x\,\mu$" feature misalignments and the orbit

sample name	description
Ref.	The reference sample as in table 10.1. No misalignments, no orbit correction.
$10\,\mu$	In contrast to the reference sample, misalignments with a RMS magnitude of $10\,\mu$ are applied ($10\,\mu$m for the x-, y- and s-offsets; $10\,\mu$rad for the pitches and tilts). Both slow and fast feedback orbit correction are applied.
$5\,\mu$	Like "$10\,\mu$", but with $5\,\mu$ RMS misalignment magnitude.
$2\,\mu$	Like "$10\,\mu$", but with $2\,\mu$ RMS misalignment magnitude.
FFB only	No misalignments, only fast feedback (FFB) orbit correction is applied.

Table 10.1: Simulated samples for the investigation of the effects of misalignments.

correction mechanisms as described above. x denote the RMS magnitude of the misalignments, given in μm for the three offsets and in μrad for the three rotations (cf. section 6.4). The sample "$10\,\mu$" exploits the maximum capability of the orbit correction implemented here. The sample "FFB only" serves to evaluate possible effects of the fast feedback (as implemented here) without misalignments.

10.1 Orbit Correction Feedback Systems

The ILC beam delivery system contains two feedback orbit correction systems which operate on different timescales (section 8.7 of [7]). One of them which is called here "slow feedback" operates along the entire beamline up to the e^+e^- IP at a repetition rate of 5 Hz, i. e. on the timescale of bunch trains. It serves to avoid a beam loss and maintain the beam quality as good as possible. The "fast feedback" at the e^+e^- IP performs corrections between the bunches of a single train and serves to maintain the luminosity in the collision. Both corrections systems are implemented here and are introduced in the following. Although this study investigates only single bunches, the terms slow and fast are used to distinguish these two systems.

10.1.1 Slow Feedback

In order to mitigate the effects of the misaligned magnets, a feedback orbit correction system as described in section 6.5 has been implemented. The beam position monitors (BPMs) and correction dipoles (implemented as kick-

ers, see section 6.1.1) as specified in the lattice (see section 7.1.1) are used. The correction algorithm is based on the measured response to a correction upstream, which implies that BPMs located in front of the first correction dipole cannot be taken into account, as well as correction dipoles behind the last BPM. The last correction dipoles are located few meters in front of the IP. In the case of collisions, the luminosity measurement provides information about the beam positions at the IP. Therefore, the IP is included in the orbit correction scheme in this simulation, as if a BPM had been installed at this position. Such a correction system is as well foreseen for the extraction line; however, it is not implemented in the used lattice (section 7.1.1) and thus also not in this simulation.

The resolution of the BPMs is assumed to be perfect for the following reason: the aim of this part of this study is to investigate the effects of misalignments on the spin transport. The possible magnitude of the misalignments that can be investigated is limited by the increasing number of beam losses at collimators and other beamline elements with limited aperture for larger RMS magnitudes of the misalignments. Therefore, it is advantageous to implement an orbit correction that might be performing better than it would in reality. For the same reason, the BPMs are assumed not to be subject of any misalignments, although many of them are directly attached to magnets.

To perform the orbit correction, the simulation is run with a single test particle with the initial coordinates $\boldsymbol{r}(s = 0) = \mathbf{0}$ - i. e. the properties of the reference particle - repeatedly through the lattice with the same set of misalignments that is also used afterwards for the bunch tracking. The particle positions at the BPMs are used as input to compute the correction dipole strengths for the next iteration. An exit condition based on the number of iteration steps and the improvement with respect to the last step is applied. Usually the iteration finishes within 10 steps or less. If the test particle does not reach the end of the beamline when the iteration is terminated, this set of misalignments is rejected and replaced by a new one. If the test particle has been propagated successfully through the lattice, the simulation is run with full bunch and the results are recorded. A successful propagation of the test particle does however not imply that all particles of a full bunch reach the end of the beamline, since the transverse extension of the bunch is not taken into account by the test particle.

10.1.2 Fast Feedback at the IP

To ensure collisions with the maximum luminosity at the IP, an additional correction is performed right there in the simulation. It is planned to control

the relative bunch positions (e^--bunch relative to e^+-bunch) and incident angles up to 0.1 standard deviations of the bunch size and angular divergence, respectively, using a fast feedback correction that operates on bunch-to-bunch timescales [45].

In reality, this correction is based on BPM signals and on the luminosity measurement as described in section 8.7.1 of [7]. In this simulation, it is implemented in a strongly simplified way. Before the particles are parsed to Guinea-Pig++ to simulate the collision effects, the transverse coordinates of each bunch are shifted (i. e. the transverse coordinates of all particles in a bunch are shifted by the same amount), such that the new mean bunch positions $\langle x \rangle$ and $\langle y \rangle$ are zero plus a random number representing the precision of the correction. The random numbers are Gaussian-distributed with mean zero and a standard deviation corresponding to the precision of the correction, which is $0.1\,\sigma_y/\sqrt{2} = 0.4\,\text{nm}$ for both the horizontal and the vertical correction. The additional factor $1/\sqrt{2}$ arises from the positions being corrected here relative to the reference orbit and not relative to the oncoming bunch. Analogously, the bunch incident angles are corrected to $0.1\,\theta_y/\sqrt{2} = 1\,\mu\text{rad}$. Since the correction would be performed by sufficiently fast kicker magnets (i. e. dipoles) in reality, the spins are rotated correspondingly by the $(1 + a\gamma)$-fold angle.

Misalignments can also cause skew correlations, additional dispersion and detune the focussing at the IP. Consequently, the bunch sizes at the IP can increase remarkably, as shown in section 8.2. In reality, the focussing magnets would be adjusted to compensate for these effects. In the simulation, the bunch sizes at the IP are corrected in a similar way as position and angle: the horizontal distance of all particles to the bunch center is scaled, such that the standard deviation of the distances equals the horizontal design bunch sizes at the IP. The vertical distances are treated accordingly. For the bunch size correction, no imprecision is simulated.

10.2 Results

A common feature of the following results are enlarged spreads in several bunch parameters as result of the misalignments and the imperfections of the orbit correction. These spreads represent the possible variation for different sets of misalignments for the respective sample. Thus, the corresponding variations in the bunch parameters would occur on timescales of days or longer, but they do not imply that adjustments (e. g. of the polarimeter lasers) for such variations on shorter timescales would be required.

10.2.1 Particle transport

Figure 10.1 shows the transverse positions of the electron bunches between upstream polarimeter and downstream polarimeter. Up to the IP, the orbit

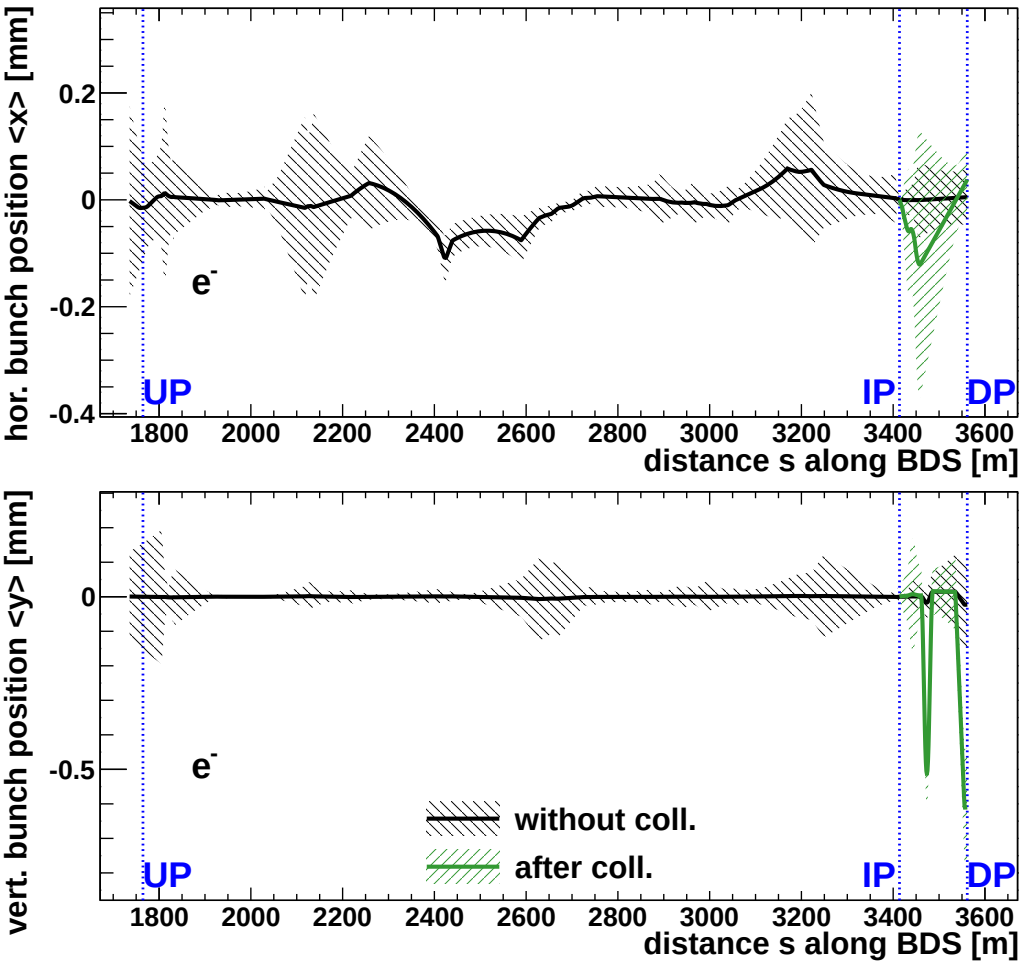

Figure 10.1: Horizontal (a) and vertical (b) electron bunch positions along the BDS for the sample "10 μ".

correction confines the bunches within 0.2 mm (RMS) distance to the design orbit. At the IP, the fast feedback adjusts the positions to 0 ± 0.4 nm. But the misalignments in the extraction line, where no orbit correction is implemented (see section 10.1.1), lead again to a rise in the position uncertainty. After a collision at the IP, the enlarged energy spread contributes via dispersion to the uncertainties and also causes the excursions in the vertical direction in the magnet chicanes in the extraction line. The reasons for the excursions in the horizontal direction, which are significantly smaller, have

not been examined further.

Table 10.2 lists the number of lost particles at different positions. Up to the sample "$5\,\mu$", no losses occur apart from the simulation-conditioned ones (cf. section 9.4). In the sample "$10\,\mu$", there are a few cases in which a larger number of particles gets lost between the upstream polarimeter and the IP, as the numbers suggest. Yet, the average loss is a fraction of $5 \cdot 10^{-5}$ and therefore negligible.

	Ref.	$5\,\mu$	$10\,\mu$
UP	0 ± 0	0 ± 0	0 ± 0
IP before collision	0 ± 0	0 ± 0	2 ± 55
IP after collision	34 ± 6	$[34 \pm 6]$	$[36 \pm 55]$
DP without collision	0 ± 0	0 ± 0	2 ± 55
DP after collision	34 ± 6	$]34 \pm 6]$	$[36 \pm 55]$

Table 10.2: Number of lost macroparticles $N_{\mathrm{lost}}^{\mathrm{macro}}$ for the samples "Ref.", "$5\,\mu$" and "$10\,\mu$" at different positions. For all samples, each bunch consists of 40 000 macroparticles. The results put in square brackets have been identified as unreliable (see section 10.2.3).

Table 10.3 lists the transverse positions of the electron bunches and other selected bunch parameters for the samples "Ref.", "FFB only" and "$10\,\mu$" at the polarimeters and the IP.

Without misalignments, the beam position at the IP is only influenced by the emission of synchrotron radiation along its path (cf. section 9.1), which affects only the horizontal dimension. However, the displacement in x^{D} is less than $0.1\,\sigma_x$ and does not affect the luminosity (cf. chapter 9).

For the sample "$10\,\mu$", the slow feedback alone is unable to ensure collisions. Especially the spread in $\langle y \rangle$ corresponds to several design bunch sizes σ_y. The transverse bunch sizes do not match the design values either, especially σ_y, which is most likely a result of dispersion (cf. section 8.2.3). After application of the fast feedback, all parameters are corrected as described in section 10.1.2. The spread of $\langle x^{\mathrm{D}} \rangle$ is larger, since only the x-coordinates are corrected, but not the z-coordinates. Nevertheless, the spread of $\langle x^{\mathrm{D}} \rangle$ is safely below $0.1\,\sigma_x^{\mathrm{D}}$.

At the downstream polarimeter, the incident angle $\langle x' \rangle$ is reduced significantly as result of the fast feedback orbit correction at the IP. Apart from that, the incident angles at both polarimeters remain below $10\,\mu$rad (including the enlarged spreads for the sample "$10\,\mu$"), i. e. $\vartheta_{\mathrm{bunch}}$ remains within the envisaged tolerance of $50\,\mu$rad (cf. section 7.4.2).

			Ref.	FFB only	$10\,\mu$
UP	$\langle x \rangle$	[μm]	-19.5 ± 0.2		-15 ± 97
	$\langle y \rangle$	[μm]	0.00 ± 0.02		0 ± 155
	$\langle x' \rangle$	[μrad]	0.083 ± 0.005	see Ref.	0 ± 3
	$\langle y' \rangle$	[μrad]	$-0.000\,0 \pm 0.000\,1$		-0 ± 1
	σ_x	[μm]	31.8 ± 0.1		32 ± 2
	σ_y	[μm]	3.16 ± 0.01		6 ± 3
IP	$\langle x^{\mathrm{D}} \rangle$	[nm]	-7 ± 3		-42 ± 271
before	$\langle y \rangle$	[nm]	0.00 ± 0.03		1 ± 42
feedback	$\langle x' \rangle$	[μrad]	-11.2 ± 0.2	see Ref.	-0 ± 5
	$\langle y' \rangle$	[μrad]	-0.00 ± 0.07		0 ± 6
	σ_x^{D}	[nm]	627 ± 2		$1\,919 \pm 659$
	σ_y	[nm]	5.76 ± 0.02		205 ± 94
IP	$\langle x^{\mathrm{D}} \rangle$	[nm]		1 ± 11	-0 ± 11
before	$\langle y \rangle$	[nm]		0.0 ± 0.4	0.0 ± 0.4
collision	$\langle x' \rangle$	[μrad]	see above	0 ± 1	-0.0 ± 1.0
	$\langle y' \rangle$	[μrad]		0.0 ± 1.0	0.0 ± 1.0
	σ_x^{D}	[nm]		639.00	639.00
	σ_y	[nm]		5.700 0	5.700 0
DP	$\langle x \rangle$	[μm]	6.02 ± 0.07	3.5 ± 0.2	5 ± 53
without	$\langle y \rangle$	[μm]	-24.6 ± 0.2	-24.6 ± 0.3	-23 ± 136
collision	$\langle x' \rangle$	[μrad]	5.67 ± 0.08	0.0 ± 0.5	0.1 ± 0.6
	$\langle y' \rangle$	[μrad]	0.110 ± 0.009	0.1 ± 0.1	0 ± 1
	σ_x	[μm]	14.7 ± 0.1	13.6 ± 0.1	14.4 ± 0.9
	σ_y	[μm]	39.1 ± 0.1	39.1 ± 0.3	42 ± 6
DP	$\langle x \rangle$	[μm]	242 ± 19	6 ± 34	$[38 \pm 71]$
after	$\langle y \rangle$	[μm]	-569 ± 16	-573 ± 83	$[-610 \pm 175]$
collision	$\langle x' \rangle$	[μrad]	19.7 ± 0.8	0 ± 2	$[2 \pm 3]$
	$\langle y' \rangle$	[μrad]	0.1 ± 0.3	0 ± 2	$[0 \pm 2]$
	σ_x	[μm]	$3\,010 \pm 53$	$3\,002 \pm 50$	$[2\,803 \pm 274]$
	σ_y	[μm]	$1\,229 \pm 39$	$1\,292 \pm 164$	$[1\,575 \pm 300]$

Table 10.3: Selected bunch parameters at different positions for the samples "Ref.", "FFB only" and "$10\,\mu$". The results put in square brackets have been identified as unreliable (see section 10.2.3).

Without collisions, the transverse positions of the bunches at the laser-bunch IPs of the polarimeters can wander due to the misalignments up to $\sim 150\,\mu$m (on long timescales, as mentioned at the beginning of this chapter).

Therefore, the positions of the polarimeter laser spots have to be adjustable on this scale. Most likely, this does not set additional requirements to the optical alignment systems of the polarimeter lasers, which are already needed to compensate the limited precision of the mechanical adjustment, not to mention the adjustment for different beam energies (cf. section 5.1.3).

In reality, the fast feedback orbit correction corrects the bunch position and angle at the IP only with respect to the oncoming bunch, whereas the implementation as described in section 10.1.2 corrects them also with respect to the reference orbit. Therefore, the bunch displacement along the extraction line might be underestimated by this simulation. Then again, such larger displacement might be correctable by the orbit correction system in the extraction line, which is not implemented here (cf. section 10.1.1).

The transverse bunch sizes at the polarimeters rise slightly due to the misalignments, as well as the spreads of the bunch sizes. If the laser spot size is chosen to be about the same size as the electron bunch or smaller, the laser-bunch luminosity decreases as consequence. For a much larger laser-spot, there is no effect (see section 4.6 in [38]).

The simulation of the collision effects and the bunch parameters after the collision will be discussed in section 10.2.3.

10.2.2 Spin transport

Table 10.4 lists the values of the incident angle ϑ_{bunch}, the angular divergence θ_r, the longitudinal polarization $\mathcal{P}_z$ and the (entire) polarization $|\vec{\mathcal{P}}|$ at the polarimeters and the IP for the samples defined in table 10.1. Furthermore, the values of $f(\theta_r)$ (see section 7.3) are given. Since $f(\theta_r)$ does not account for the depolarization by emission of beamstrahlung, the values after the collision are omitted. In the after-collision scenario, also the measurable longitudinal polarization at the downstream polarimeter as defined in section 9.5 is provided. Since θ_r is not affected by the fast feedback orbit correction and the polarization only by a negligible correction for ϑ_{bunch} (see table 7.7), the values before the application of the correction are not listed separately.

The differences between the samples "Ref." and "FFB only" are negligible with respect to the envisaged precision of 0.1 % (cf. section 5.2), which means that the fast feedback orbit correction without misalignments does not have a noticable effect on the polarization measurement. With increasing amplitude of the misalignments, the uncertainties on the polarization values rise at the polarimeters and the IP, while the values remain mostly unchanged within these uncertainties.

Without collisions, $|\vec{\mathcal{P}}|$ and $f(\theta_r)$ agree to a level $< 2{\cdot}10^{-4}$, for all samples

		Ref.	FFB only	$2\,\mu$	$5\,\mu$	$10\,\mu$
UP	$\vartheta_{\text{bunch}}\,[\mu\text{rad}]$	0.083 ± 0.005		0.6 ± 0.4	1.5 ± 0.9	3 ± 2
	$\theta_r\,[\mu\text{rad}]$	0.984 ± 0.003		0.985 ± 0.004	0.987 ± 0.005	1.00 ± 0.01
	$\mathcal{P}_z$	0.799 994 3 (0)	see Ref.	0.799 99 (1)	0.799 96 (4)	0.799 9 (1)
	$\lvert\vec{\mathcal{P}}\rvert$	0.799 999 3 (0)		0.799 999 3 (0)	0.799 999 2 (0)	0.799 999 2 (1)
	$f(\theta_r)$	0.799 999 9 (0)		0.799 999 9 (0)	0.799 999 9 (0)	0.799 999 9 (0)
IP	$\vartheta_{\text{bunch}}\,[\mu\text{rad}]$	11.2 ± 0.2	1.3 ± 0.7	1.3 ± 0.7	1.3 ± 0.7	1.2 ± 0.7
before	$\theta_r\,[\mu\text{rad}]$	36.4 ± 0.1	36.4 ± 0.1	36.9 ± 0.7	39 ± 4	45 ± 10
collision	$\mathcal{P}_z$	0.799 818 (1)	0.799 850 (2)	0.799 84 (1)	0.799 78 (6)	0.799 6 (2)
(after	$\lvert\vec{\mathcal{P}}\rvert$	0.799 854 0 (9)	0.799 854 0 (9)	0.799 850 (7)	0.799 82 (4)	0.799 7 (1)
correction)	$f(\theta_r)$	0.799 829 (1)	0.799 830 (1)	0.799 824 (7)	0.799 80 (4)	0.799 7 (1)
DP	$\vartheta_{\text{bunch}}\,[\mu\text{rad}]$	5.67 ± 0.08	0.5 ± 0.3	0.5 ± 0.3	0.7 ± 0.4	1.1 ± 0.6
without	$\theta_r\,[\mu\text{rad}]$	16.88 ± 0.06	16.86 ± 0.06	16.9 ± 0.2	17.0 ± 0.4	17.3 ± 0.9
collision	$\mathcal{P}_z$	0.799 945 3 (4)	0.799 941 3 (9)	0.799 93 (1)	0.799 90 (4)	0.799 8 (2)
	$\lvert\vec{\mathcal{P}}\rvert$	0.799 945 3 (4)	0.799 945 3 (4)	0.799 945 (1)	0.799 944 (3)	0.799 943 (5)
	$f(\theta_r)$	0.799 963 4 (3)	0.799 963 4 (3)	0.799 963 1 (7)	0.799 963 (2)	0.799 961 (4)
IP	$\theta_r\,[\mu\text{rad}]$	206 ± 1	208 ± 1	$[181 \pm 2]$	$[182 \pm 3]$	$[184 \pm 7]$
after	$\mathcal{P}_z$	0.793 82 (7)	0.793 89 (8)	[0.795 0 (2)]	[0.795 0 (2)]	[0.794 7 (5)]
collision	$\lvert\vec{\mathcal{P}}\rvert$	0.794 02 (7)	0.793 90 (7)	[0.795 1 (2)]	[0.795 0 (2)]	[0.794 9 (4)]
DP	$\theta_r\,[\mu\text{rad}]$	117.8 ± 0.8	118.6 ± 0.6	$[102 \pm 1]$	$[103 \pm 2]$	$[104 \pm 5]$
after	$\mathcal{P}_z$	0.797 37 (4)	0.797 35 (4)	[0.797 8 (1)]	[0.797 7 (2)]	[0.797 5 (3)]
collision	$\lvert\vec{\mathcal{P}}\rvert$	0.797 39 (4)	0.797 35 (4)	[0.797 8 (1)]	[0.797 8 (2)]	[0.797 7 (3)]

Table 10.4: Incident angle ϑ_{bunch}, angular divergence θ_r, longitudinal polarization $\mathcal{P}_z$, (entire) polarization $|\vec{\mathcal{P}}|$ and the function $f(\theta_r)$ as defined in eq. 7.8 of the electron beam at the IP and the polarimeters (UP/DP = up-/downstream polarimeter) for the samples listed in table 10.1. The results put in square brackets have been identified as unreliable (see section 10.2.3).

and locations. Thus, the increasing uncertainties in $|\vec{\mathcal{P}}|$ can be traced back to the uncertainties in the angular divergence θ_r.

For the samples featuring misalignments, the uncertainties on the longitudinal polarization $\mathcal{P}_z$ at the polarimeters are remarkably larger than the uncertainties on $|\vec{\mathcal{P}}|$. This discrepancy still lacks explanation. The incident angles ϑ_{bunch} and their larger spreads are ruled out as explanation, since angles $\vartheta_{\text{bunch}} \lesssim 5\,\mu\text{rad}$ lead only to a relative uncertainty of $4 \cdot 10^{-6}$ (cf. table 7.7), while the uncertainty on $\mathcal{P}_z$ at the downstream polarimeter for the sample "$10\,\mu$" amounts to $2.5 \cdot 10^{-4}$.

Taking into account that the actual sizes of the misalignments are unknown in reality, the uncertainties[1] amount to $1.1 \cdot 10^{-4}$ and $4.3 \cdot 10^{-4}$ at the downstream polarimeter for the samples "$5\,\mu$" and "$10\,\mu$", respectively.

The simulation of the collision effects and the parameters after the collision will be discussed in the following section.

10.2.3 Collisions in Presence of Misalignments

Table 10.5 shows the luminosities and beamstrahlung parameters for the samples listed in table 10.1. First, the simulation results for the samples "Ref." and "FFB only" are confronted with each other. The simulated luminosities for these two samples differ only slightly, reflecting the effect of the fast feedback orbit correction. The bunch parameters and the polarization (tables 10.3, 10.4 and 10.6) do not differ significantly either, apart from the horizontal displacement $\langle x \rangle$ at the downstream polarimeter, which is remarkably reduced for the sample "FFB only" thanks to the correction of the incident angle $\langle x' \rangle$ at the IP (cf. section 9.1).

sample	$\mathcal{L}$ $[10^{38}\,\text{m}^{-2}\,\text{s}^{-1}]$	Υ_{max}
Ref.	2.02 ± 0.02	0.134 ± 0.008
FFB only	1.97 ± 0.04	0.135 ± 0.004
$2\,\mu$	$[3.0 \pm 0.4]$	$[0.142 \pm 0.004]$
$5\,\mu$	$[2.4 \pm 0.4]$	$[0.141 \pm 0.005]$
$10\,\mu$	$[1.9 \pm 0.4]$	$[0.13 \pm 0.04]$

Table 10.5: Luminosities and maximum occurring beamstrahlung parameters for the samples listed in table 10.1. For the calculation of the luminosities, 13 125 bunch collisions per second are assumed. The results put in square brackets have been identified as unreliable (see text).

[1] These uncertainties are obtained by setting the lower boundary of the spread of the sample with misalignments in relation to the value of the sample without misalignment.

sample	Ref.	FFB only
$\mathcal{P}_z^{\text{lumi,1}}$	0.798 08 (3)	0.798 10 (3)
$\lvert\vec{\mathcal{P}}\rvert^{\text{lumi,1}}$	0.798 09 (3)	0.798 10 (3)

Table 10.6: Luminosity-weighted longitudinal and entire electron polarization for the samples "Ref." and "FFB only".

Under the influence of misalignments, one would naïvely expect a decrease of the luminosity at the IP with respect to the sample "FFB only" due to the disturbances caused by the misalignments. However, table 10.5 shows significant[2] increases in the simulated luminosities for the samples "2 μ" and "5 μ", which shall be addressed in this section.

Figure 10.2 shows the luminosity evolution versus the bunch position in the bunch train for various ground motion models [54] from a different study [55]. The rise in the luminosity indicates a stepwise improvement of the beam alignment by the fast feedback orbit correction after the time gap between two bunch trains during which no correction could be carried out for lack of input signals, i. e. bunch position measurements. Model A and B describe two rather quiet sites, for which the luminosity get close to the design value ($2 \cdot 10^{34}\,\text{cm}^{-2}\text{s}^{-1} = 2 \cdot 10^{38}\,\text{m}^{-2}\,\text{s}^{-1}$), while for model C with the strongest ground motion the luminosity only reaches $1.7 \cdot 10^{34}\,\text{cm}^{-2}\text{s}^{-1}$. Values larger than the design value are not obtained at all.

The luminosity depends strongly on the exact bunch shape (section 8.7.1.3 in [7]). Distortions of the bunch shape and additional dispersion due to the misalignments are not corrected in the simulation for this thesis, but only the RMS bunch sizes (see section 10.1.2), which provides a likely explanation for the unexpected behavior of the luminosity. While the exact bunch shape is not relevant for the simulation of the spin transport, it might have large influence on the simulation of the collisions beyond the calculation of the luminosity. In this context, it is remarkable that θ_r, $\mathcal{P}_z$ and $|\vec{\mathcal{P}}|$ at the IP after the collision (table 10.4) take quite similar values for the samples "2 μ", "5 μ" and "10 μ", which are however significantly different from the corresponding values for the sample "FFB only". The differences to the results for the sample "FFB only" indicate that the simulation of the spin fan-out and the depolarization in the collision is affected by the misalignments as well, but in a rather different manner than the luminosity. Therefore, it has been decided not to rely on these results. Presumably, an accurate simula-

[2] As explained in section 7.1.3, the results are given in the form "mean±spread". The uncertainty on the mean error is the spread divided by $\sqrt{1000}$ for the samples listed in table 10.1.

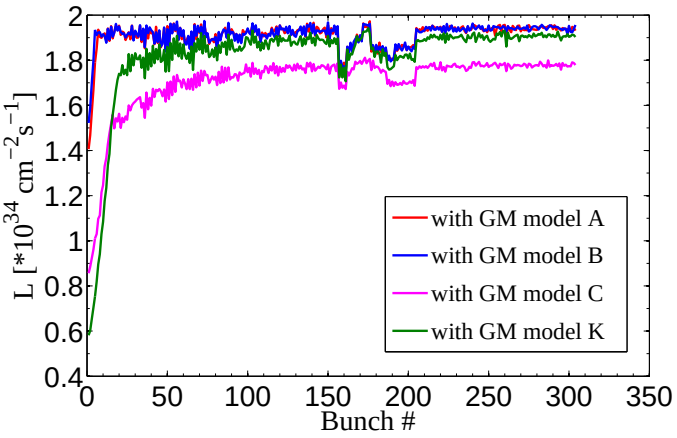

Figure 10.2: Luminosity vs. bunch number in a train for different ground motion (GM) models (example for one single random seed). Taken from figure 3 of [55].

tion of the collisions under the influence of misalignments would require a more realistic orbit correction including the bunch shapes and possibly also dispersion.

Nevertheless it is worth to notice that it is possible to increase the luminosity without increasing the spin fan-out/depolarization (as it has already been demonstrated for the waist shift, cf. section 9.6). Furthermore, these results imply that the measured luminosity and measurements of the amount of beamstrahlung cannot be used to estimate the spin fan-out/depolarization in the collision.

10.2.4 Conclusion

In this chapter, the effects of misalignments on the polarization measurement have been studied for static configurations of misalignments of different amplitudes to assess the resulting uncertainties to the polarization transport in the ILC beam delivery system. A realignment might be already required at smaller misalignment amplitudes for other reasons, e. g. in order to maximize the time-integrated luminosity.

In absence of collisions, misalignments cause a rise in the uncertainties of all bunch parameters including the polarization. While a readjustment of the polarimeter lasers can make up for the larger displacements of the beams, the rising uncertainties on the longitudinal polarization set limits for the acceptable misalignment amplitude.

The orbit correction by the fast feedback in absence of misalignments

with the envisaged precision (see section 10.1.2) does not impact the spin fan-out / depolarization in the collision or the spin transport through the extraction line.

To combine collisions and misalignments, possible future studies should comprise a more realistic implementation of the orbit correction, which includes a reduction of the dispersion at the IP and possibly an adjustment of the focussing magnets. In the next step, the investigation should be extended to bunch trains instead of single bunches, as pointed out in the following.

The gradual improvement of the beam alignment during a bunch train, which is displayed in figure 10.2, influences most likely also the collision effects on the polarization. Therefore, a study combining collisions and misalignments should include a realistic ground motion model [54], such that not only space and time correlations of the individual misalignments, but also the time structure of the beam are taken into account more accurately than in the implementation used in this thesis.

According to figure 10.2, one can expect a different values and uncertainties of longitudinal polarization at the IP and downstream for the first 10 to 100 bunches due to the gradual improvement of the beam alignment. Therefore, it seems to be advantageous for the determination of an average luminosity-weighted longitudinal polarization over many bunches to average separately over the single bunch positions in a train, or at least average separately over different blocks of bunches.

Chapter 11

Conclusions and Outlook

In the preceding chapters, the spin transport through the ILC beam delivery system has been scrutinized for the precision to which the polarization at the IP can be derived from the measurements at the polarimeters or vice versa. Table 11.1 summarizes the various contributions to the total uncertainty which have been determined in the corresponding chapters. The upper part of the table lists the effects in absence of collisions, which is especially relevant for the calibration of the polarimeters against each other.

contribution	section	uncertainty $[10^{-3}]$
Beam and polarization alignment at polarimeters and IP ($\Delta\vartheta_{\text{bunch}} = 50\,\mu\text{rad}$, $\Delta\vartheta_{\text{pol}} = 25\,\text{mrad}$)	7.4.2	0.72
Variation in beam parameters (10 % in the emittances)	7.3.4	0.03
Bunch rotation to compensate the beam crossing angle	8.1.2	< 0.01
Longitudinal precession in detector magnets	8.2.3	0.01
Emission of synchrotron radiation	9.1	0.005
Misalignments ($10\,\mu$) without collision effects	10.2.2	0.43
Total (quadratic sum)		0.85
Collision effects in absence of misalignments	9.6	< 2.2

Table 11.1: Contributions to the uncertainty of the spin transport in the ILC beam delivery system.

The main contribution comes from the alignment of the beam at the polarimeters (upstream vs. downstream) and the alignment of the polarization vector to the beam at the upstream polarimeter. Therefore, it is

crucial that the set goals regarding the alignment precision can be achieved ($\Delta\vartheta_{\text{bunch}} = 50\,\mu\text{rad}$ and $\Delta\vartheta_{\text{pol}} = 25\,\text{mrad}$, see section 7.4.2). In absence of collisions, the alignment at the IP is not relevant. This circumvents a possibly difficult angle measurement at the curved trajectory in the field of the detector magnets, such that the alignment precision might be higher in this case.

The effects of the bunch rotation at the IP and the detector magnets on the spin transport have been shown to be negligible. Therefore, it does not matter for the calibration of the polarimeters whether the crab cavities or the detector magnets are switched on or off, as long as the beam orbit at the downstream polarimeter is parallel to the beam orbit at the upstream polarimeter. Only a possible effect of skew quadrupoles to compensate x-y coupling from the detector solenoid (see section 8.2.3) on the angular divergence θ_r remains to be investigated. Furthermore, variations of the beam parameters at the percent level have only negligible influence on the polarization measurement in absence of collisions. Misalignments up to "$10\,\mu$" (cf. chapter 10) are another important source of uncertainty.

In absence of collisions, all these effects sum up to an RMS uncertainty of $0.85 \cdot 10^{-3}$, which matches the goal of 0.1 % formulated in section 5.2.

The lower part of table 11.1 table lists the additional contributions to the uncertainty, if beam-beam collisions occur. These collisions influence the polarization by the mutual disruption of the colliding bunches as well as by emission of beamstrahlung. The energy losses caused by the latter lead to large increases in the transverse bunch sizes at the downstream polarimeter.

The underlying idea in the design of the extraction line is to restore the luminosity-weighted polarization $\mathcal{P}_z^{\text{lumi},1}$ in the collision at the downstream polarimeter (see section 5.1.3). The overall longitudinal polarization at the downstream polarimeter is however smaller than $\mathcal{P}_z^{\text{lumi},1}$ due to the additional depolarization by beamstrahlung and due to a stronger spin fan-out caused by the energy loss. In contrast, the measurable longitudinal polarization $\mathcal{P}_z^{mr}$ is larger than $\mathcal{P}_z^{\text{lumi},1}$(for the considered laser spot sizes and samples), since $\mathcal{P}_z^{mr}$ comprises mostly particles which have lost rather little energy and have been deflected less than the average, such that their spins also have fanned out less.

The relative deviation of the measurable longitudinal polarization (assuming a laser spot size of $100\,\mu$m) from the luminosity-weighted longitudinal polarization for the sample with a collision intensity corresponding to the TDR parameters has been taken here as a preliminary value for the uncertainty, which amounts to $2.2 \cdot 10^{-3}$. The deviation depends on the intensity of the collision as well as the size and the position of the laser spot. To determine a reliable prediction of this deviation with a smaller uncertainty,

a more detailed simulation of the laser-bunch interaction is required, taking into account the intensity distribution within a laser pulse as well as a realistic laser model considering especially the uncertainties on the knowledge of the size of the laser-spot. To obtain a better understanding of the measurable polarization and its connection to spin fan-out, a measurable angular divergence θ_r^{mr} defined analogously to the measurable longitudinal polarization $\mathcal{P}_z^{mr}$ should be scrutinized. Possible improvements of the simulation of the collision effects comprise a beam transport simulation with the TDR lattice, such that the TDR parameters do not have to be mimicked by a larger bunch charge like in chapter 9, and an update of the simulation of the collision effects which includes the recent developments in that field for larger values of Υ [56].

Such an improved simulation will give valuable input for the decision on the laser spot size at the downstream polarimeter. The decision needs to be a trade-off between diverging demands: on the one hand, a small laser spot size is favored in view of the required laser power and the energy spread of the incoming electrons; on the other hand, the uncertainty of the size of the laser spot contributes the less to the uncertainty of the polarization measurement, the larger the laser spot is (cf. figure 9.5a). With an improved simulation as described above and a sufficiently large laser spot, it might be feasible[1] to describe the collision effects up to a precision of $< 0.1\,\%$.

As explained in chapter 10, a reliable statement for the uncertainty contribution from misalignments in combination with beam-beam collisions is not possible yet, but require more thorough studies. These comprise a more realistic model of the misalignments based on the existing ground motion models [54] and an improved orbit correction.

The simulation presented in this thesis starts at the end of the main linac, assuming ideal bunches at the starting point. To include also the imperfections from the other parts of the accelerator (e. g. the beam source and the damping rings), a simulation of the entire beamline ("cradle-to-grave") is planned [57].

[1] This estimate is motivated by the fact that the relative deviation of the measurable longitudinal polarization $\mathcal{P}_z^{m0.5}$ from $\mathcal{P}_z^{m1.0}$ for the sample "Υ_{TDR}" (cf. table 9.2) amounts to $9{\cdot}10^{-5}$, which gives only a negligible contribution to the total spin transport uncertainty (cf. table 11.1).

Acknowledgments

This PhD thesis would not have been accomplished without the support from many different sides. Therefore, I would like to thank

- Jenny List for the extensive supervision of this thesis including a 4-month research trip to SLAC; furthermore, for giving me the chance to get to know the multifarious world of high energy physics, also beyond the scope of my thesis.
- Kenneth Moffeit and Michael Woods for their dedicated supervision during my time at SLAC.
- David Sagan et al. for providing a well-documented simulation software [21, 22] and quick e-mail support and bug fixes.
- Deepa Angal-Kalinin for providing an updated BDS lattice [19].
- all the above and Desmond Barber, Karsten Büßer, Eckhard Elsen, Anthony Hartin, Benno List, Gudrid Moortgat-Pick, Yuri Nosochkov, Javier Resta-Lopez, Cecile Rimbault, Christoph Rosemann, Andre Sailer, Daniel Schulte, Andrei Seryi, Jeffrey Smith, Mathias Vogt, Nicholas Walker, Volker Ziemann and several more for helpful discussions, advice, information, bug fixes and support.

During my times at DESY and SLAC, I enjoyed sharing offices (including also helpful discussions, advice etc.) with Christoph Bartels, Christian Helebrant, Daniela Käfer, Jeremy McCormick, Hale Sert and especially with Mădălina Chera and Benedikt Vormwald.

Bibliography

[1] ATLAS collaboration (G. Aad *et al.*), "Observation of a new particle in the search for the Standard Model Higgs boson with the ATLAS detector at the LHC", Phys. Lett. **B716**, 1 (2012), doi:10.1016/j.physletb.2012.08.020, arXiv:1207.7214 [hep-ex].
CMS collaboration (S. Chatrchyan *et al.*), "Observation of a new boson at a mass of 125 GeV with the CMS experiment at the LHC", Phys. Lett. **B716**, 30 (2012), doi:10.1016/j.physletb.2012.08.021, arXiv:1207.7235 [hep-ex].

[2] ALEPH and CDF and D0 and DELPHI and L3 and OPAL and SLD and LEP Electroweak Working Group and Tevatron Electroweak Working Group and SLD Electroweak and Heavy Flavour Groups Collaborations, "Precision Electroweak Measurements and Constraints on the Standard Model", 2010, arXiv:1012.2367v2 [hep-ex].

[3] G. Moortgat-Pick *et al.*, "The role of polarized positrons and electrons in revealing fundamental interactions at the Linear Collider", 2005, doi:10.1016/j.physrep.2007.12.003.

[4] P.C. Rowson, D. Su, S. Willocq, "Highlights of the SLD physics program at the SLAC linear collider", Ann. Rev. Nucl. Part. Sci. **51**, 345 (2001), doi:10.1146/annurev.nucl.51.101701.132413.

[5] SLD collaboration (K. Abe *et al.*), "A High precision measurement of the left-right Z boson cross-section asymmetry", Phys. Rev. Lett. **84**, 5945 (2000), doi:10.1103/PhysRevLett.84.5945.

[6] ILC Technical Design Report, 2013,
`http://www.linearcollider.org/ILC/Publications/Technical-Design-Report`
Volume 1: "Executive Summary", arXiv:1306.6327v1 [physics.ins-det],
Volume 2: "Physics", arXiv:1306.6352v1 [physics.ins-det],
Volume 3.I: "Accelerator R&D", arXiv:1306.6353v1 [physics.acc-ph],

Volume 3.II: "Accelerator Baseline Design",
arXiv:1306.6328v1 [physics.acc-ph],
Volume 4: "Detectors", arXiv:1306.6329v1 [physics.ins-det].

[7] Volume 3.II of [6].

[8] Volume 4 of [6].

[9] M. Aicheler *et al.* "A Multi-TeV Linear Collider Based on CLIC Technology: CLIC Conceptual Design Report", 2012, doi:10.5170/CERN-2012-007.

[10] G. H. Hoffstätter, "High-Energy Polarized Proton Beams - A Modern View", Springer Science+Business Media, LLC, New York, 2006, Springer Tracts in Modern Physics, Vol. 218.

[11] M. Vogt, "Bounds on the maximum attainable equilibrium spin polarization of protons at high energy in HERA", Ph. D. Thesis, Hamburg University, 2000, DESY-THESIS-2000-054.

[12] J. C. Smith, "The Preservation of Emittance and Polarization in the International Linear Collider", Ph. D. Thesis, Cornell University, 2007.

[13] I. Bailey *et al.*, "Time evolution of ground motion-dependent depolarisation at linear colliders", Proceedings of 13$^{\text{th}}$ International Workshop on Polarized Sources and Targets & Polarimetry (PST 2009, Ferrara, Italy), 2011, arXiv:1108.6275v1 [physics.acc-ph].

[14] M. Beckmann and J. List, "Spin tracking studies for polarimetry at the ILC", Proceedings of 19$^{\text{th}}$ International Spin Physics Symposium (SPIN 2010, Jülich, Germany), J. Phys. Conf. Ser. **295** 012134 (2011), doi:10.1088/1742-6596/295/1/012134.

[15] ILC Reference Design Report, 2007,
`http://www.linearcollider.org/ILC/Publications/Reference-Design-Report`
Volume 1: "Executive Summary", arXiv:0712.1950v1 [physics.acc-ph],
Volume 2: "Physics at the ILC", arXiv:0709.1893v1 [hep-ph],
Volume 3: "Accelerator", arXiv:0712.2361v1 [physics.acc-ph],
Volume 4: "Detectors", arXiv:0712.2356v1 [physics.ins-det].

[16] Volume 3 of [15].

[17] M. Ross *et al.*, SB2009 Proposal Document, 2009, `http://lcdev.kek.jp/SB2009`.

[18] Website of the Linear Collider Collaboration, `www.linearcollider.org`, 2012.

[19] D. Angal-Kalinin *et al.*, ILC SB2009_Nov10 lattice, `http://projects.astec.ac.uk/ilcdecks`.

[20] P. Bambade *et al.*, "Results of the EUROTeV Beam-Beam Simulation (BBSIM) Task", EUROTeV 2008-065.

C. Rimbault *et al.*, "Implementation of depolarization due to beam-beam effects in the beam-beam interaction simulation tool GUINEA-PIG++", EUROTeV 2008-066.

G. Le Meur *et al.*, "Description of guineapig++, the C++ upgraded version of the GUINEA-PIG beam-beam simulation program", EUROTeV 2008-067.

Former project website: `https://trac.lal.in2p3.fr/GuineaPig`.

Current project website:
`https://savannah.cern.ch/projects/guinea-pig`.

[21] D. Sagan *et al.*, Bmad, `www.lepp.cornell.edu/~dcs/bmad`.

[22] D. Sagan, "The Bmad Reference Manual", Revision 16.7 (March 8, 2012), `www.lepp.cornell.edu/~dcs/bmad/manual.html`.

[23] A. Vogel, "The Coordinate System for LDC Detector Studies", 2005, LC-DET-2005-009, `http://www-flc.desy.de/lcnotes/`.

[24] D. Schulte, "Study of Electromagnetic and Hadronic Background in the interaction Region of the TESLA Collider", Ph. D. Thesis, Universität Hamburg, 1996, TESLA 1997-08.

[25] Daniel Schulte, CERN, private communication, 2012.

[26] Cecile Rimbault, LAL, France, private communication, 2012.

[27] J. D. Jackson, „Klassische Elektrodynamik", (original title: "Classical Electrodynamics"), translated by K. Müller, 2nd edition, Walter de Gruyter, Berlin, New York, 1983.

[28] C. Amsler *et al.* (Particle Data Group), Phys. Lett. **B667**, 1 (2008).

[29] M. Conte, W. W. MacKay, "An Introduction to the Physics of Particle Accelerators", 2nd edition, World Scientific, Singapore, 2008.

[30] B. W. Montague, "Polarized Beams in High-Energy Storage Rings", Phys. Rept. **113**, 1-96 (1984).

[31] K. Yokoya, P. Chen, "Depolarization due to Beam-Beam-Interaction in Electron-Positron Linear Colliders", AIP Conf. Proc. **187**, 938 (1989), SLAC-PUB-4692.

[32] A. Vogel, "Beam-Induced Backgrounds in Detectors at the ILC", Ph. D. Thesis, Hamburg University, 2008, DESY-THESIS-08-036.

[33] M. Woods, "Polarimetry at a Future Linear Collider - How precise?", Int. J. Mod. Phys. **A15**, 2529 (2000), SLAC-PUB-8397, doi:10.1142/S0217751X00002603.

[34] A. W. Chao, M. Tigner "Handbook of Accelerator Physics and Engineering", 2nd edition, World Scientific, Singapore, 1999.

[35] K. Yokoya, "User's Manual of CAIN", Version 2.35, April 2003, `http://lcdev.kek.jp/~yokoya/CAIN/cain235/CainMan235.pdf`.

[36] W. H. McMaster, "Matrix Representation of Polarization", Rev. Mod. Phys. **33**, 8 (1961).

[37] S. Boogert *et al.*, "Polarimeters and Energy Spectrometers for the ILC Beam Delivery System", JINST **4**, P10015 (2009), doi:10.1088/1748-0221/4/10/P10015.

[38] V. Gharibyan *et al.*, "The TESLA Compton Polarimeter", LC-DET-2001-047, 2001, `http://www-flc.desy.de/lcnotes/`.

[39] K. Moffeit *et al.*, "Proposal to Modify the Polarimeter Chicane in the ILC 14 mrad Extraction Line", 2007, SLAC-PUB-12425.

[40] I. Marchesini, "Triple Gauge Couplings and Polarization at the ILC and Leakage in a Highly Granular Calorimeter", Ph. D. Thesis, Hamburg University, 2011, DESY-THESIS-11-044.

[41] J. List, "Corrections to the Blondel Scheme for not exactly equal Polarisations", 2013, unpublished.

[42] W. H. Press *et al.*, "Numerical Recipes - The Art of Scientific Computing", Cambridge University Press, Cambridge, 1989.

[43] C. Weißbäcker, "Nichtlineare Effekte der Spindynamik in Protonenbeschleunigern", Diploma Thesis (in German), Technical University Darmstadt, 1998, DESY-THESIS-99-019.

C. Weißbäcker, G. H. Hoffstätter "Nonlinear Spin Transfer Maps", Proceedings of the workshop "Polarized protons at high energies - accelerator challenges and physics opportunities" (Hamburg, 1999), 1999.

[44] ROOT, versions 5.28 and 5.30, `http://root.cern.ch`.

[45] G. White, N. Walker, D. Schulte, "Design and Simulation of the ILC Intra-Train Orbit and Luminosity Feedback Systems", Proceedings of the 10^{th} European Particle Accelerator Conference (EPAC 06, Edinburgh, Scotland), 2006, EUROTEV-REPORT-2006-088.

[46] I. N. Bronstein *et al.*, "Taschenbuch der Mathematik" (Handbook of Mathematics) 5^{th} edition, Verlag Harry Deutsch, Thun and Frankfurt am Main, 2001.

[47] A. Seryi, T. Maruyama, B. Parker, "IR Optimization, DID and anti-DID", 2006, SLAC-PUB-11662.

[48] Nick Walker, DESY, private communication, 2011.

[49] G. Burt, P. Goudket, "Crab cavity system design", talk given at Snowmass workshop 2005, `http://www.slac.stanford.edu/econf/C0508141/proc/pres/ILCAW0532_TALK.PDF`.

[50] B. Parker, A. Seryi, "Compensation of the effects of a detector solenoid on the vertical beam orbit in a linear collider", Phys. Rev. STAB **8**, 041001 (2005), doi:10.1103/PhysRevSTAB.8.041001.

[51] Y. Nosochkov, A. Seryi, "Compensation of detector solenoid effects on the beam size in a linear collider", Phys. Rev. STAB **8**, 021001 (2005), doi:10.1103/PhysRevSTAB.8.021001.

[52] Takashi Maruyama, SLAC, USA, private communication, June 2010.

[53] D. Schulte, "Beam-beam simulations with GUINEA-PIG," CERN-CLIC-NOTE-387 (1999).

[54] International Linear Collider Technical Review Committee, Second report, 2003, SLAC-R-606.

A. Seryi, `http://www.slac.stanford.edu/~seryi/gm/model`.

[55] J. Resta-Lopez *et al.*, "Luminosity Performance Studies of Linear Colliders with Intra-train Feedback Systems", 2009, arXiv:0902.2915v1 [physics.acc-ph].

[56] A. Hartin *et al.*, "Strong field effects on physics processes at the Interaction Point of future linear colliders", Proceedings of the 36$^{\text{th}}$ International Conference on High Energy Physics (ICHEP2012, Melbourne, Australia), 2013, arXiv:1304.2632v1 [hep-ph].

A. Hartin, "Towards the exact calculation of strong field effects on polarized particles at future linear colliders", talk given at the European Linear Collider Workshop 2013 (ECFA LC2013, Hamburg, Germany).

[57] Gudrid Moortgat-Pick, University of Hamburg, private communication, 2013.

List of Used Symbols

The following table contains a quick reference to the symbols used in this thesis, their meaning and the chapters where they are introduced. Scalar quantities are printed italic (E), 3-vectors are marked with an arrow ($\vec{\mathcal{P}}$), whereas all other vectors are printed bold and italic ($\boldsymbol{r}$), and matrices bold and non-italic ($\mathbf{R}$).

Symbol	Meaning	Chapter
a	Gyro-magnetic moment anomaly $a \equiv \frac{g-2}{2}$. For electrons and positrons: $a \approx 0.001\,16$.	-
A	Asymmetry.	5.1.1
B, $\vec{B}$	Magnetic field.	-
$B\rho$	Magnetic rigidity of a particle/beam.	6.1.2
b	$b \equiv \vartheta_{\mathrm{pol}}/\vartheta_{\mathrm{bunch}}$.	3.2.5
c	Vacuum speed of light $c \approx 3 \cdot 10^8 \mathrm{m/s}$.	-
E	Particle energy.	-
E_0	Nominal beam energy.	-
E_{CM}	Center-of-mass energy.	-
$\mathcal{L}$	Luminosity in the beam-beam-collision.	-
L	Length of a beamline element.	-
m_e	Electron mass $m_e \approx 0.511\,\mathrm{MeV}/c^2$.	-
N_e	Number of particles per bunch.	3.2
N_e^{macro}	Number of macroparticles per bunch.	3.2
$N_{\mathrm{lost}}^{\mathrm{macro}}$	Number of lost macroparticles per bunch.	9.4
N_{rep}	Number of simulation runs.	7.1.2
$\vec{\mathcal{P}}$	Polarization vector.	3.2.5, 4.1
$\vec{\mathcal{P}}^{\mathrm{lumi,1}}$, $\vec{\mathcal{P}}^{\mathrm{lumi}}$	Polarization vector (luminosity-weighted).	4.1.2
$\mathcal{P}_z^{mr}$	Measurable longitudinal polarization for different radii r.	9.5
$\mathcal{P}_z^{\mathrm{corr}}$	Corrected longitudinal polarization.	7.4
$\mathcal{P}_3^{\gamma}$	Circular photon polarization.	5.1.1
$\vec{p}$	(Unnormalized) particle momentum.	3.1.1

$\hat{p}_x$, $\hat{p}_y$	Normalized transverse momenta.	3.1.1
p_0	Nominal beam momentum $p_0^2 = E_0^2 - m_e^2 \approx E_0^2$.	
q	Particle charge.	-
Q	The quotient defined in eq. 4.24.	4.2.4
$\boldsymbol{r}$	6-dimensional particle coordinates	3.1.1
r_e	Classical electron radius $r_e \approx 2.818 \cdot 10^{-15}\,\mathrm{m}$.	-
$\mathbf{R}$	Beam transfer matrix.	7.2.2
s	Longitudinal coordinate along the reference orbit.	3.1.1
$\vec{S}$	Classical spin vector.	4.1
x, y	Transverse coordinates.	3.1.1
x^{D}	Co-moving horizontal coordinate in the detector coordinate system.	3.2.1
x', y'	Horizontal/vertical angle of a particle trajectory towards the reference orbit.	3.1.1
$\langle x' \rangle$, $\langle y' \rangle$	Horizontal/vertical angle of the bunch trajectory towards the reference orbit.	3.1.1
z, $\hat{z}$	Longitudinal coordinates.	3.1.1
$\alpha_x, \alpha_y, \beta_x, \beta_y$	Twiss parameters.	6.3
β, γ	Relativistic Lorentz factors.	-
γ_0	Relativistic Lorentz factor for the nominal beam energy E_0.	-
δ	Normalized momentum.	3.1.1
ε_x, ε_y	Bunch emittances.	3.2.3
ζ	Crossing angle between the e^--beamline and the e^+-beamline. $\zeta = 14\,\mathrm{mrad}$.	3.1.2
ϑ_0	Crossing angle between the e^-/e^+beam and the laser of the polarimeters. $\vartheta_0 = 10\,\mathrm{mrad}$.	5.1
$\vartheta_{\mathrm{bunch}}$	Polar angle of the bunch direction of motion.	3.2.2
$\vartheta_{\mathrm{crab}}$	Rotation angle of the bunch at the IP due to the crab cavities.	8.1
ϑ_{pol}	Polar angle of the polarization vector $\vec{\mathcal{P}}$.	3.1.1
θ_r, θ_x, θ_y	Angular divergences. $\theta_r \equiv \sqrt{{\theta_x}^2 + {\theta_y}^2}$.	3.2.2
$\lambda\!\!\!^{-}_e$	Reduced electron Compton wavelength $\lambda\!\!\!^{-}_e \approx 3.862 \cdot 10^{-13}\,\mathrm{m}$.	-
ξ_{orbit}	Deflection angle of the particle orbit.	4.2.1
ξ_{spin}	Spin precession angle.	4.2.1
Π	Analyzing power.	5.1.2
ρ	Bending radius of a trajectory in a magnetic field.	6.1.2

σ_x, σ_y, σ_z	Bunch sizes.	3.2.1
σ_x^{D}	Horizontal bunch size with respect to the center-of-mass system of the collision.	3.2.1
σ_E/E	Bunch energy spread.	3.2.2
σ	cross section	-
τ_1, τ_2, τ_3	Pauli matrices.	6.6

Table 2: List of symbols used in this thesis. The symbols are sorted alphabetically, first the Latin characters, then the Greek ones. Unless stated otherwise, the system of reference is the beamline coordinate system (section 3.1.1). The right column points to the chapter where the respective variable is introduced.